

The Pennsylvania State University

The Graduate School

College of Engineering

**EXPERIMENTAL INVESTIGATION OF INTERNAL SHORT CIRCUITS  
IN LITHIUM-ION BATTERIES**

A Dissertation in

Mechanical Engineering

by

Poowanart Poramapojana

© 2015 Poowanart Poramapojana

Submitted in Partial Fulfillment  
of the Requirements  
for the Degree of

Doctor of Philosophy

December 2015

The dissertation of Poowanart Poramapojana was reviewed and approved\* by the following:

Chao-Yang Wang  
William E. Diefender Chair of Mechanical Engineering  
Dissertation Advisor  
Chair of Committee

Stefan T. Thynell  
Professor of Mechanical Engineering

Christopher D. Rahn  
Professor of Mechanical Engineering

Tony Jun Huang  
Professor of Engineering Science and Mechanics

Karen A. Thole  
Professor of Mechanical Engineering  
Head of the Department of Mechanical and Nuclear Engineering

\*Signatures are on file in the Graduate School

## ABSTRACT

With outstanding performance of Lithium-ion batteries, they have been widely used in many applications. For hybrid electric vehicles and electric vehicles, customer concerns of battery safety have been raised as a number of car accidents were reported. To evaluate safety performance of these batteries, a nail penetration test is used to simulate and induce internal short circuits instantaneously. Efforts to explain failure mechanisms of the penetration using electrochemical-thermal coupled models have been proposed. However, there is no experimental validation because researchers lack of a diagnostic tool to acquire important cell characteristics at a shorting location, such as shorting current and temperature.

In this present work, diagnostic nails have been developed to acquire nail center temperatures and shorting current flow through the nails during nail penetration tests. Two types of cylindrical wall structures are used to construct the nails: a double-layered stainless steel wall and a composite cylindrical wall. An inner hollow cylinder functions as a sensor holder where two wires and one thermocouple are installed. To study experimental reproducibility and repeatability of experimental results, two nail penetration tests are conducted using two diagnostic nails with the double-layered wall. Experimental data shows that the shorting resistance at the initial stage is a critical parameter to obtain repeatable results. The average shorting current for both tests is approximately 40 C-rate. The fluctuation of the shorting current is due to random sparks and fire caused loose contacts between the nail and the cell components. Moreover, comparative experimental results between the two wall structures reveal that the wall structure does not affect the cell characteristics and Ohmic heat generation of the nail. The wall structure effects to current measurements inside the nail. With the composite wall, the actual current redistribution into the inner wall is found to be a sinusoidal waveform.

## TABLE OF CONTENTS

List of Figures .....	vi
List of Tables .....	ix
List of Abbreviations .....	x
List of Symbols .....	xi
Acknowledgements.....	xiii
Chapter 1 Introduction .....	1
1.1. Battery Internal Short Circuits .....	3
1.1.1 Experimental Studies on Nail Penetration Tests .....	6
1.1.2 Modeling and Simulation Studies for Nail Penetrations .....	8
1.2. Motivations .....	12
1.3. Dissertation Outline.....	13
Chapter 2 In situ Measurements of Internal Short Circuits during Nail Penetration .....	14
2.1. A Diagnostic Nail Design .....	14
2.1.1 Nail Resistance Dependence on Temperature.....	16
2.1.2 Nail Resistance Measurements.....	17
2.2. Experimental .....	24
2.3. Results and Discussion.....	26
2.3.1 Nail Penetration Test #1: Proof of Concept .....	26
2.3.2 Nail Penetration Test #2: Repeatability and Reproducibility .....	34
2.4. Summary .....	48
Chapter 3 Effects of Nail Composite Wall on Cell Characteristics during a Nail Penetration Test.....	49
3.1. A Diagnostic Nail with Ceramic Sensor Holder .....	49
3.2. Experimental .....	59
3.3. Results and Discussions .....	60
3.3.1 Cell Characteristics during the Nail Penetration Test #3 .....	60
3.3.2 Energy Balance of the Diagnostic Nails at the Shorting Area .....	73
3.4. Summary .....	80
Chapter 4 Conclusions and Future Work.....	81
4.1. Conclusions .....	81
4.2. Future Work .....	82
4.2.1 Parametric Study of Nail Structure Design .....	82
4.2.2 Effects of Nail Thermal Conductivity on Cell Characteristics during a Nail Penetration Test .....	82

4.2.3 Experimental Investigation on Electrical and Thermal Contact Resistance in Nail Penetrations .....	83
References.....	85

## LIST OF FIGURES

Figure 1-1 U.S. Hybrid Electric Vehicles (HEV) and plug-in HEV sales between 1999 – 2013.....	1
Figure 1-2 Tesla S caught on fire after an accident in Tennessee [4] .....	3
Figure 2-1 A diagram of a prototype (left) and a diagnostic nail (right) .....	15
Figure 2-2 A cross section diagram at the location of measurements (left) and a sensor holder (right) .....	16
Figure 2-3 A circuit diagram for a nail resistance measurement .....	18
Figure 2-4 Experimental set up for nail resistance measurements.....	19
Figure 2-5 Current flow through the nail for the nail resistance measurements .....	20
Figure 2-6 Voltage drop between the inner probes for the nail resistance measurements .....	20
Figure 2-7 Nail center temperatures during the nail resistance measurements.....	21
Figure 2-8 Nail surface temperatures during the nail resistance measurements .....	21
Figure 2-9 Ambient temperatures during the nail resistance measurements .....	22
Figure 2-10 Nail resistance between the inner probes as a function of nail center temperatures .....	22
Figure 2-11 Average nail resistance as a function of nail center temperatures.....	23
Figure 2-12 Locations of voltage and temperature measurements outside the nail .....	25
Figure 2-13 Experimental setup in the operation chamber of the nail penetration tester .....	26
Figure 2-14 Penetration depth of the nail before the penetration completed.....	28
Figure 2-15 Schematic of current flow path and measurements at the shorting location .....	29
Figure 2-16 Current flow path in a cross section area (left) and charge at the interface between the internal wall of the hollow nail and the external wall of the stainless steel sensor holder (right).....	29
Figure 2-17 Nail temperatures, cell surface temperatures and ambient temperatures .....	30
Figure 2-18 Nail resistance between the inner probes during the nail penetration test #1 .....	30
Figure 2-19 Cell voltage and average shorting current for the nail penetration test #1 .....	31

Figure 2-20 Errors of the shorting current estimation for the nail penetration test #1 .....	31
Figure 2-21 Cell characteristics of the nail penetration #1 during 0 s to 0.3 s.....	32
Figure 2-22 Cell characteristics of the nail penetration #1 during 0.1 s to 4.4 s.....	33
Figure 2-23 Dimension components of Nail #1 and Nail #2 .....	36
Figure 2-24 Average nail resistance comparison between Nail #1 and Nail #2 .....	37
Figure 2-25 Experimental setup for the repeatability test.....	38
Figure 2-26 Penetration depth of Nail #2 before the penetration completed.....	38
Figure 2-27 Cell characteristics of the nail penetration #2 during 0 s to 3.6 s.....	39
Figure 2-28 Nail center temperatures comparison between Test#1 and Test#2 .....	40
Figure 2-29 Nail surface temperatures comparison between Test#1 and Test#2 .....	41
Figure 2-30 Comparisons of cell surface temperatures between Test#1 and Test#2.....	42
Figure 2-31 Comparisons of average nail resistance during the penetration of Test #1 and Test #2.....	43
Figure 2-32 Cell voltage comparison between Test #1 and Test #2.....	44
Figure 2-33 Average shorting current comparison between Test #1 and Test #2.....	45
Figure 2-34 Cumulative discharge capacity comparison between Test #1 and Test #2 .....	46
Figure 2-35 Cumulative discharge capacity as a function of cell voltages for Test #1 and Test #2.....	47
Figure 3-1 A diagram of a new design nail (left) and a new diagnostic nail (right) .....	51
Figure 3-2 A cross section diagram at the location of measurements for a new nail design (left) and a ceramic sensor holder (right) .....	52
Figure 3-3 Current flow through the nail for the nail resistance measurements .....	53
Figure 3-4 Voltage drop between the inner probes for the nail resistance measurements .....	54
Figure 3-5 Nail center temperatures during the nail resistance measurements.....	55
Figure 3-6 Nail surface temperatures during the nail resistance measurements .....	56
Figure 3-7 Ambient temperatures during the nail resistance measurements .....	57

Figure 3-8 Nail resistance between the inner probes as a function of nail center temperatures .....	58
Figure 3-9 Experimental setup for the nail penetration test #3 .....	59
Figure 3-10 Penetration depth of Test #3 before the penetration completed .....	62
Figure 3-11 Diagram of current flow path and measurements at the shorting location for Nail #3.....	62
Figure 3-12 Cell characteristics of the nail penetration #3 .....	63
Figure 3-13 Nail center temperatures comparison between Test#1 and Test#3 .....	64
Figure 3-14 Nail surface temperatures comparison between Test#1 and Test#3 .....	65
Figure 3-15 Comparisons of cell surface temperatures between Test#1 and Test#3.....	66
Figure 3-16 Comparisons of average nail resistance during the penetration of Test #1 and Test #3.....	67
Figure 3-17 Cell voltage comparison between Test #1 and Test #3 .....	68
Figure 3-18 Voltage drops between the inner probes for Test #1 and Test #3 .....	69
Figure 3-19 Average shorting current comparison between Test #1 and Test #3.....	70
Figure 3-20 Discharge capacity as a function of time for Test #1 and Test #3 .....	71
Figure 3-21 Cell voltage as a function of discharge capacity for Test #1 and Test #3 .....	72
Figure 3-22 Control volumes of the diagnostic nails used in Test #1 (left) and Test #3 (right) .....	75
Figure 3-23 Accumulative heat comparison for Test #1 and Test #3 .....	76
Figure 3-24 Ohmic heat comparison for Test #1 and Test #3.....	77
Figure 3-25 Accumulative energy and thermal energy generation of the nail used in Test #1.....	78
Figure 3-26 Accumulative energy and thermal energy generation of the nail used in Test #3.....	79

**LIST OF TABLES**

Table 1-1 Summary of experimental studies for nail penetration tests.....	11
Table 2-1 Nail resistance at 20 °C and temperature coefficients of resistivity for Nail #1 using least square linear fit curves .....	23
Table 2-2 Specifications of a cell for nail penetration tests .....	24
Table 2-3 Nail resistance at 20 °C and temperature coefficients of resistivity for Nail #2 using least square linear fit curves .....	37
Table 3-1 Nail resistance at 20 °C and temperature coefficients of resistivity for Nail #3 using least square linear fit curves .....	58
Table 3-2 Material properties of a nail.....	75
Table 4-1 Material properties of 304 stainless steel and 1018 mild steel [39].....	84

**LIST OF ABBREVIATIONS**

<i>HEV</i>	hybrid electric vehicles
<i>EV</i>	electric vehicles
<i>U.S.</i>	the united states
<i>NHTSA</i>	national highway traffic safety administration
<i>mm</i>	millimeter
<i>s</i>	second
<i>SOC</i>	battery state of charge
<i>FEM</i>	finite element model
<i>C – rate</i>	charge or discharge rate
<i>BAJ</i>	battery association of Japan
<i>Ah</i>	ampere – hour
<i>PP</i>	polypropylene
<i>PE</i>	polyethylene
<i>ECR</i>	electrical contact resistance
<i>TCR</i>	thermal contact resistance
<i>NCA</i>	nickel cobalt aluminum
<i>NMC</i>	nickel manganese cobalt
<i>CC – CV</i>	constant current – constant voltage

## LIST OF SYMBOLS

$T$	temperature
$Li_{4/3}Ti_{5/3}O_4$	lithium titanium oxide
$LiCoO_2$	lithium cobalt oxide
$LiMnO_2$	lithium manganese dioxide
$LiFePO_4$	lithium iron phosphate
$LiMn_4O_2$	lithium manganese oxide
$LiNiO_2$	lithium nickel oxide
$C_6$	graphite
$R$	resistance
$l$	distance between the copper wires
$A$	area
$V$	voltage
$I$	current
$m$	mass
$c_p$	specific heat at constant pressure
$t$	time
$D$	diameter
$\dot{E}$	rate of energy

### Greek Letters

$\alpha$	thermal diffusivity of the material
$\beta$	temperature coefficient of resistivity
$\rho$	density of the material

$\sigma$  electrical conductivity of the material

$\Delta$  differential value

### **Subscripts**

0 reference value

*c* cross section

*t* thermal

*ss* stainless steel

*Acc* accumulative heat

*In* entering

*Out* leaving

*Gen* generation

## ACKNOWLEDGEMENTS

First and foremost, I would like to sincerely thank to my advisor, Dr. Chao-Yang Wang, for his guidance and support. I also would like to thank my dissertation committee, Dr. Chris Rahn, Dr. Stefan Thynell and Dr. Tony Jun Huang for their invaluable comments and suggestions.

I am grateful to all members of the Electrochemical Engine Center (ECEC) at The Pennsylvania State University especially Man Su Park, Dan Marple, Dr. Lei Cao, Kamiar Salehi, Tanvia Tanim, Yubai Li, Dawn Fisher, Dr. Guangsheng Zhang, Dr. Yongjun Leng and Dr. Yancheng Zhang for sharing of their time and knowledge. I also would like to thank Bill Genet of the Learning Factory for help on lathe machining.

I gratefully acknowledge financial support throughout my graduate studies from The Royal Thai Government. I would like to express my gratitude to my brother Poodis, my sisters Suwana, Apinya, Patima and Ratchada, Kejkaew Thanasuan, Aunt Povongtip and Uncle Preecha for their eternal love, caring advice and encouragement. Finally, I would like to dedicate this work to my parent.

“But still try, for who knows what is possible.”

- *Michael Faraday*

## Chapter 1

### Introduction

With the increasingly stringent emission regulations, car manufacturers have electrified their vehicles to reduce fuel consumption and to improve energy efficiency. The penetration of Hybrid Electric Vehicles (HEV) and Electric Vehicles (EV) into the U.S. market has been increasing significantly [1]. Figure 1-1 shows HEV and plug-in HEVs sold in the United States between 1999 and 2013. Lithium-ion batteries have been widely implemented into these applications because the batteries can provide high power and high energy. However, there are still a few remaining challenges for use of the batteries in vehicles. One of the most important challenges is safety performance of the batteries.

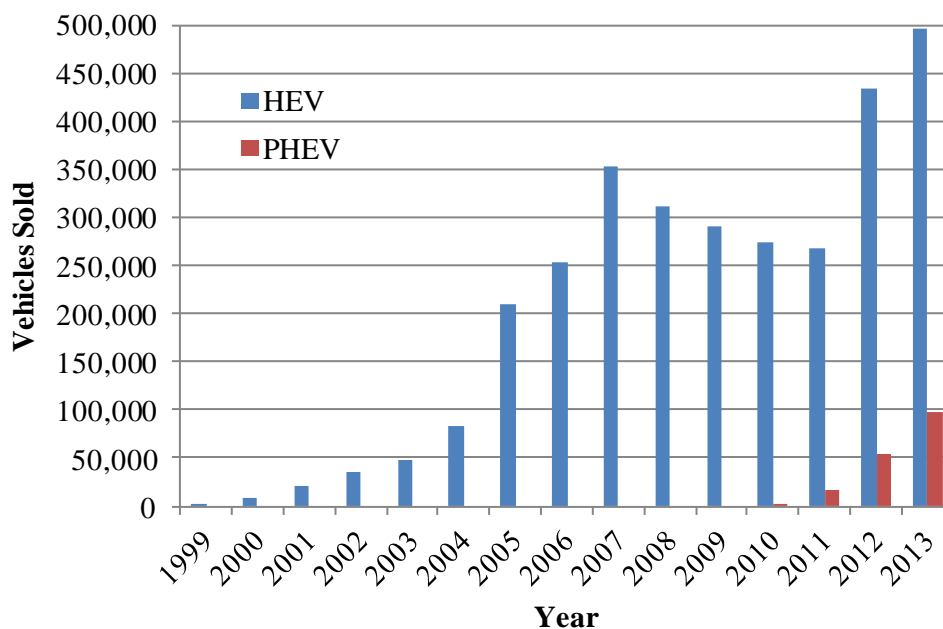


Figure 1-1 U.S. Hybrid Electric Vehicles (HEV) and plug-in HEV sales between 1999 – 2013

Battery safety is a major barrier to introduction of electrified vehicles powered by Lithium-ion batteries into markets. For new vehicles, the National Highway Traffic Safety Administration (NHTSA) evaluates safety performance of the vehicles beyond Federal Motor Vehicle Safety Standards (FMVSS). Based on real world crash scenarios, the NHTSA created the 5-Star safety ratings program to quantify crashworthiness of the vehicles for consumers.

In 2011, the NHTSA performed a side collision test for a plug-in hybrid electric Chevy Volt [2]. After the test was completed, Lithium-ion battery packs caught fire. To investigate the failure, the NHTSA attempted to replicate the damage in full scale vehicle and battery pack testing. Ultimately, the NHTSA was not able to reproduce the battery fire.

Moreover, car accidents of Tesla's Model S also show the irreproducible battery fire. The Model S was certified five-stars for crash tests from the NHTSA. However, three cars still caught on fires after collisions [3]–[5]. Two cases of fires resulted from collisions with road debris causing underbodies damaged. Another case resulted from high speed car impact which caused damages to the bottom of the car. Figure 1-2 shows a Tesla S sedan on fire after an accident in Tennessee. Tesla avoided future problems by increasing the ground clearance of the Model S, as well as installing a triple underbody shield to protect the battery pack of the car [6]. The investigations of NHTSA indicate that the reproducibility of the battery fire is very poor. To improve battery safety performance, failure mechanisms implicated in battery fires need elucidation.



Figure 1-2 Tesla S caught on fire after an accident in Tennessee [4]

### 1.1. Battery Internal Short Circuits

A common root cause of fire in the batteries is an internal short circuit. The battery internal short circuit is an electrical circuit that allows a flow of electricity through a conductor along an unintended path inside a battery. The conductor is often a low-resistance conductor. With a connection between two nodes, the battery tries to balance the voltage between the nodes to reach the same voltage. The low-resistance conductor allows a large current flowing through the conductor within a very short time. Based on Joule heating, therefore high heat energy is generated rapidly. If the heat generation cannot dissipate quickly, the battery may catch fire and explode.

For Lithium-ion batteries, internal short circuits may be caused by internal defects from battery manufacturing processes or cell damage. A latent flaw could be a small conductive particle wound in a jelly roll, a wrinkle in the separator, or the poor alignment of a winding [7]. The cell damage may be caused by crash, impact, drop, indentation or penetration. Many researchers have studied failure mechanisms of internal short circuits in Lithium-ion batteries. To create a

reproducible failure, researchers have proposed a few methods to trigger an internal short circuit inside Lithium-ion batteries.

For latent defects, Darcy [8] presents destructive physical examinations of a failure in a Lithium-ion polymer pouch cell battery designed for a spacesuit. The author simulated the failure of native material contaminations coupled with an insulation defect in cell fabrication processes. In manufacturing processes, the inclusions cannot be detected during screening tests because the inclusions are high-impedance conductors. After cycling tests, the impedance of the inclusions is decreased until the internal short circuit can be triggered. With trial and error experiments, the failure can be replicated successfully by using a 0.15 mm diameter needle punctures on the edge of a pouch cell.

Takami et al simulated a defect on a separator by cutting a separator with an 18 mm × 18 mm hole for fabricating a single-layered cell [9]. The cell contained a single-layered Lithium Titanium Oxide ( $\text{Li}_{4/3}\text{Ti}_{5/3}\text{O}_4$ ) anode, a single-layered Lithium Cobalt Oxide ( $\text{LiCoO}_2$ ) cathode and the separator. The internal short circuits were performed by pressing the cell with constant force. Comparative experimental studies show that the fully discharge time of a short circuit between the cathode and the anode current collector was two order of magnitude faster than a short circuit between the cathode and the anode, and a short circuit between the cathode current collector and the anode. However, there is no report on failure reproducibility.

Ramadass et al. also simulated a defect on a separator using a separator with a hole of 2 mm diameter for manufacturing 1Ah prismatic cells [10]. The cathode material is  $\text{LiCoO}_2$  and the anode material is graphite ( $\text{C}_6$ ). Comparative experimental results show that the cell surface temperatures in a short circuit test between the cathode current collector and the anode are higher than other cases. In addition, the maximum temperature can be reached with a shorter time when the battery State of Charge (SOC) is increased.

Cai et al. [11] introduced a pinch test to simulate internal short circuits near cell surface. Three types of Lithium-ion batteries were tested with different open circuit voltages. Experimental results showed that the risk of thermal runaway increases significantly as the open circuit voltages of the cells increase. However, the thermal runaway is not reproducible at 4.1 V open circuit voltage. Later, Ren et al. introduced a pinch-torsion test to increase failure reproducibility [12]. Their experimental results still show non-uniform of the thermal runaway.

To understand mechanical behaviors of Lithium-ion cells that lead to cell damage caused an internal short circuit, Sahraei et al. [13]–[15] proposed Finite Element Models (FEM) for commercially available cylindrical and pouch cells under compression tests. The cathode material of the cells is  $\text{LiCoO}_2$ . The FEM models consider only mechanical behaviors with no regard to electrochemical reaction. Simulation results reveal that internal short circuits occur when both cell voltage and compressive force suddenly dropped. For indentation tests, a conical punch required the lowest compressive force to penetrate into pouch cells comparing with a flat cylindrical punch and hemispherical punches. Wierzbicki and Sahraei [16] proposed a failure criteria of the cells using the maximum tensile stress of materials. The simulation results show a good agreement with experimental results for both cases of crushing and indentation.

Greve and Fehrenbach [17] also introduced a FEM for predicting deformation, fracture and short circuit initiation of a large format cylindrical cell. The cathode material is Lithium Nickel Cobalt Aluminum (NCA) Oxide. The classical stress-based fracture criterion of Coulomb and Mohr is used to identify the short circuit initiation. Simulation and experimental results show that the model can predict a fracture location accurately in the case of crushing but not in the cases of bending and indentation.

### 1.1.1 Experimental Studies on Nail Penetration Tests

A nail penetration test is a type of mechanical abuse test used to evaluate safety performance of Lithium-ion batteries. The penetration aims to create cell damage and to induce internal short circuits instantaneously. For a general test, a metal nail is indented through a battery cell or a battery pack at a specified speed then the cell/pack are observed. To pass the test, the cell or the pack must have no fire, gas generation or explosion during the penetration.

At the early stage of commercializing Lithium-ion batteries, researchers reported experimental studies on nail penetration tests along with material developments for the batteries. Most of the studies documented the observations of fire, gas generation and explosion during nail penetration tests only. A summary of essential parameters for experimental studies on nail penetration tests is listed in Table 1-1.

For comparative studies between cycled cells and fresh cells, Ozawa of Sony Corporation reported experimental studies of  $\text{LiCoO}_2$  cylindrical cell on nail penetration tests [18]. His experimental results show that cycled cells were safer than fresh cells. Tobishima et al. also reported safety characteristics of prototype AA-size Lithium-ion cells [7]. The cathode materials are  $\text{V}_2\text{O}_5\text{-P}_2\text{O}_5$  and the anode material is a Lithium metal sheet. A fresh cell and four different cycled cells were used to evaluate safety performance. Experimental results of the tests show that both cells passed the tests.

To improve safety characteristics of the batteries, Wu et al. introduced a shutdown separator [19]. The shutdown separator consists of a layer of Polyethylene (PE) and two layers of Polypropylene (PP).  $\text{LiCoO}_2$  prismatic cells were fabricated with three different separators including PP separator, PE separator and the shutdown separator. For safety characteristics comparison between 10 cycled and 200 cycled cells, experimental results of 10 cycled cells show that there were no fires, gas generation and explosions during the tests. However, the cells

fabricated with PE and the shutdown separators swelled after the tests were done. For 200 cycled cells, only cells made with PP separator caught on fire and exploded.

Battery state of charge is a sensitive parameter to cell characteristics during the penetration. Tobishima and Yamaki reported that a fully-charged cell is safer than an overcharged cell [20]. To avoid overcharging, the authors suggested that manufacturers should control the ratio of anode and cathode materials. Ramadass et al. reported effects of SOC and nail penetration speed to cell characteristics during the penetration [10]. For the SOC above 85%, all cells failed the tests. For the SOC below 85%, the penetration speed is a critical parameter to pass the tests. With slow penetration speed, the cells tentatively fail the tests.

For a battery pack level, Kito and Nemoto [21] performed safety evaluation tests using large-format Lithium-ion cells manufactured for EVs and HEVs. For a nail penetration test, experimental data show the surface cell temperatures reached the maximum temperature of 380 °C within 1 minute. However, there were no ignition and explosion because electrolyte vapor was released through the vents of the cell which were activated immediately after the stainless steel nail was penetrated into the cells. Nguyen and Taylor performed abuse tests for LiCoO<sub>2</sub> and Lithium Iron Phosphate (LiFePO<sub>4</sub>) battery packs [22]. Each pack consists of three cylindrical cells in parallel. For nail penetration tests, only a middle cell in each pack was penetrated. The initial battery pack voltage of LiCoO<sub>2</sub> and LiFePO<sub>4</sub> were 4.2 V and 3.4 V. Experimental results show that the LiFePO<sub>4</sub> battery pack is safer than the LiCoO<sub>2</sub> battery pack.

Lamb and Orendoff conducted penetration tests for commercially available 18650 cells using a blunt nail and a spike nail [23]. Experimental results show that temperature rate of change of the cell surface in the spike nail penetration is higher than the cell surface in the blunt nail penetration. In addition, the maximum cell temperature in the spike nail penetration is much higher than in the blunt nail penetrations.

Recently Hatchard et al. [24] attempted to obtain nail temperatures during nail penetration tests by inserting a thermocouple inside the tip of a nail. The body of the nail was made of stainless steel tube with 3.18 mm in diameter and the tip of a nail was made of copper. Two nail penetration tests for 18650 Lithium-ion cells were performed including slow ( $<2$  mm/s) and fast ( $>2$  mm/s) penetration speeds. With experimental results, the authors demonstrated that nail temperatures in the case of fast penetration speed were lower than seen at slow penetration speed because heat transfer for the slow speed was much better than for the fast speed.

### **1.1.2 Modeling and Simulation Studies for Nail Penetrations**

Electrochemical-thermal models have been proposed to elucidate fundamental mechanisms that govern cell behaviors during internal short circuits. Modeling and simulations reveal that heat generation and heat dissipation rate of a cell and the nail during the short circuits plays an important role for the safety performance. Unfortunately, those models have not been validated with experimental results because the lack of a diagnostic tool to acquire important cell characteristics at a shorting location, such as shorting current and heating mode.

In a general case, total heat generation during internal short circuits is a combination of three heat sources including Joule heating, electrochemical reaction and chain chemical reaction. The Joule heating is heat generation due to current passing through the shorting location. The electrochemical heat generation is obtained from the reversible and irreversible heat generation. The heat generation from chain chemical reaction can be obtained from combustion reactions. The chain chemical reaction can be neglected for normal operation.

Yamauchi et al. [25] proposed an electrochemical model to analyze characteristics of a cylindrical  $\text{LiNiO}_2$  cell during penetration. The critical cell temperature for thermal runaway was defined at  $180^\circ\text{C}$ . The shorting resistance was estimated by 0.6 ohm including the nail resistance

and the contact resistance. With simulation results, the authors found that the short-circuit current can be high as 10 C-rate at the beginning of the short, then the current decreases below 3 C-rate. To improve battery safety, the author suggested that Lithium-ion batteries need to be designed to handle high discharge rate.

In 2009, Maleki and Howard [26] introduced a thermal model to estimate heat generation and heat dissipation during nail penetration. The authors found that thermal runaway in nail penetration occurs when localized heat generation is higher than heat dissipation to the cell can. The risk of thermal runaway is high when the cell capacity is high and the local temperature exceeds the melting point of separators.

Santhanagopalan et al. [27] proposed a electrochemical-thermal model for better understanding the phenomena of Lithium-ion batteries during internal short circuits. In their model, the shorting resistance was determined from the maximum resistivity between two components undergoing a short circuit. With simulation and experimental results, the authors concluded that the short circuit between the anode material and the cathode current collector generated the maximum heat with the shortest time.

Zavalis et al. [28] introduced a 2D electrochemical-thermal model for investigating internal short circuit scenarios in a single-layer  $\text{LiNi}_{0.8}\text{Co}_{0.15}\text{Al}_{0.05}\text{O}_2$  prismatic cell. Three short circuit scenarios were studied including an external short circuit, a nail penetration and an impurity-induced short circuit. The shorting resistivity of the nail and the impurity are assumed to be the same as the aluminum current collector. Simulation results reveal that the rising rate of cell temperatures depends on the mass transport limitations of Lithium-ions in the electrolyte.

Fang et al. [29] proposed a 3D electrochemical-thermal model for studying internal short circuits in a 1Ah  $\text{LiCoO}_2$  prismatic cell. Comparative studies of shorting resistance are presented. A short between the anode and the cathode current collector simulates a low shorting resistance, whereas a short between the anode and the cathode simulates a higher shorting resistance.

Simulation and experimental results show a significant different temperature profiles during the short circuit. With the lower shorting resistance, cell temperatures are increased rapidly due to the Joule heat generation at the shorting spot. Then, the cell temperature was decreased because the Lithium-ion transport limitations in the solid and electrolyte phased. For the higher shorting resistance, cell temperatures increase continuously with much slower heat generation rate.

Zhao [30] proposed a 3D electrochemical-thermal coupled model of a 5Ah  $\text{LiNi}_{0.8}\text{Co}_{0.15}\text{Al}_{0.05}\text{O}_2$  prismatic cell to investigate physics of nail penetrations. Due to imperfect contacts between the nail and the cell components, a shorting resistance was defined as a combination of a nail resistance and a contact resistance. The author found that the shorting resistance of the nail penetration strongly effects to the cell discharge behavior. If a shorting resistance was smaller than the cell resistance, the Joule and the electrochemical heat generations of the cell are dominated. If a shorting resistance was larger than the cell resistance, the cell heat generation is dominated by the Joule heating inside the nail.

Table 1-1 Summary of experimental studies for nail penetration tests

Author	Cathode/Anode	Cell Type	Capacity (Ah)	Ø Nail (mm)	Nail Material	Max. Temp (°C)	Fire/Explosion
Ozawa [18]	LiCoO <sub>2</sub> /C <sub>6</sub>	20500	~1	4	Metal	105	No/No
Dan [31]	LiMnO <sub>2</sub> /Li	AA	0.85	n/a	n/a	n/a	No/No
Tobishima [7]	V <sub>2</sub> O <sub>5</sub> -P <sub>2</sub> O <sub>5</sub> /Li	AA	0.9	n/a	n/a	n/a	No/-
Tobishima [20]	n/a	Prismatic	0.835	2.5	Metal	40* 165**	No/No Smoke/No
Kitoh[21]	LiMn <sub>2</sub> O <sub>4</sub> /MCMB <sup>‡</sup>	Cylindrical	25	SBA <sup>†</sup>	Stainless Steel	380	No/No
Tobishima [32]	LiCoO <sub>2</sub> /C <sub>6</sub> LiMn <sub>2</sub> O <sub>4</sub> /C <sub>6</sub>	Prismatic	0.5-0.6	2.5	Metal	~50 ~90	No/No No/No
Wu [19]	LiCoO <sub>2</sub> /MCMB <sup>‡</sup>	Prismatic	0.75 <sup>1,2,3</sup> <0.65 <sup>1,2,3</sup>	3	Stainless Steel	n/a <sup>1,2,3</sup> 350 <sup>1</sup> ,105 <sup>2</sup> ,n/a <sup>3</sup>	No/No <sup>1,2,3</sup> No/No <sup>1,3</sup> ,Yes/Yes <sup>2</sup>
Nguyen [22]	LiCoO <sub>2</sub> /C <sub>6</sub> LiFePO <sub>4</sub> /C <sub>6</sub>	18650	n/a	3	Metal	600 125	Yes/Yes No/No
Takami [9]	LiCoO <sub>2</sub> / Li <sub>4/3</sub> Ti <sub>5/3</sub> O <sub>4</sub>	Prismatic	3.2	5	Metal	105	No/No
Lamb [23]	n/a	18650	2.2	3	Steel	662, 420	n/a , n/a
Ramadass [10]	LiCoO <sub>2</sub> /C <sub>6</sub>	Prismatic	1	2	Metal	113 – 135	n/a , n/a
Hatchard [24]	n/a	18650	n/a	3.18	Stainless Steel	600, 110	n/a , n/a

Note: \* fully-charge

\*\* overcharged

† Guideline for Safety Evaluation on Secondary Lithium Cells (1997), BAJ

‡ Mesocarbon microbeads

<sup>1</sup> Polypropylene (PP) Separators<sup>2</sup> Polyethylene (PE) Separators<sup>3</sup> PP/PE/PP Separators

## 1.2. Motivations

To improve battery safety, comprehension of electrochemical and thermal transport processes, as well as failure mechanisms during internal short circuits by a nail penetration need to be elucidated. Experimental investigations are very crucial to elucidate the fundamentals and failure mechanisms from proposed internal short circuit modeling and simulation. With better understanding, battery safety can be improved significantly.

The challenges of conducting experiments are not only reproducibility of failures but also acquisition of cell characteristics at the shorting location. The reproducibility of experiments is unacceptable at this time because shorting resistance cannot be controlled during nail penetrations [33], [34]. In addition, there are no fundamental studies on electrical and thermal contact resistance during nail penetration tests [30]. Moreover, Researchers lack of a diagnostic tool to investigate the cell characteristics at a shorting location.

The purpose of this dissertation is to:

- i. Invent a diagnostic nail to obtain nail temperatures and electrical current flow through the nail during a nail penetration. With acquired data, the fundamentals of electrochemical and thermal behaviors of Lithium-ion batteries during internal short circuits can be elucidated.
- ii. Develop a systematic study to investigate the reproducibility limit of nail penetration tests.
- iii. Study effects of nail composite wall on cell characteristics during nail penetration tests. With an implementation of a composite wall structure for the newly developed diagnostic nail, the electrical and the thermal resistance of the nail are

modified. The rate of heat conduction and heat generation along the nail are needed to study for improving a robust diagnostic nail.

### **1.3. Dissertation Outline**

This dissertation is organized as follows: Chapter 2 presents in situ measurements of internal short circuits during nail penetration using diagnostic nails. A structure of the nail and nail resistance measurements are introduced. Experimental results present cell surface temperatures, nail temperatures and current flow through the nail. Chapter 3 introduces a new structure of a diagnostic nail. The new nail is installed with a ceramic sensor holder to improve operating temperatures of the sensors. A nail penetration test is conducted using the new nail design. Experimental results are compared with the prototype to demonstrate effects of nail composite wall on cell characteristics during the nail penetration test. Chapter 4 provides conclusions and future work.

## Chapter 2

### **In situ Measurements of Internal Short Circuits during Nail Penetration**

A prototype of a diagnostic nail has been developed to investigate cell characteristics during internal short circuits by a nail penetration test. The nail enables to obtain nail temperatures and electrical current flow through the nail during the penetration. This chapter introduces a structure of the nail and nail resistance measurements. Based on the resistivity of nail material, the objective of resistance measurements is to establish a linear relationship between nail resistance and the nail temperatures. In situ measurements of internal short circuits during nail penetration using the diagnostic nail are presented. Experimental results show cell surface temperatures, nail temperatures and current flow through the diagnostic nail.

#### **2.1. A Diagnostic Nail Design**

A diagnostic nail was made of a 304 stainless steel rod with 3.18 mm in diameter to avoid chemical reactions between the nail and chemicals inside a cell during the penetration. The size of the nail diameter is selected based on SAE J2464 abuse and safety testing standard [35]. Figure 2-1 shows a diagram of a prototype and a diagnostic nail. The nail consists of three components including a top section, a bottom section and a sensor holder. The top section is used to hold the nail with a chuck of a nail penetration tester. The bottom section is used for penetration into the cell. A sensor holder is designed to accurate positioning of a Type J thermocouple and two copper wires. The holder is made of a miniature 304 stainless steel tube with two holes at one end. The wires and the thermocouple are bonded to the holder using PYRO-PUTTY® 2400 high temperature

metal sealer. The outer diameter of the thermocouple is 254  $\mu\text{m}$  and the diameter of wires is 127  $\mu\text{m}$ . To assemble the nail, the sensor holder is inserted into the bottom section using a press fit. Then, the top section is installed on the top section by a press fitting. The wires are used to measure voltage drop between the wires. The distance between the wires is designed to measure voltage between a pair layer of a copper foil and an aluminum foil. A diagram of measurements at a shorting location and a sensor holder are shown in Figure 2-2.

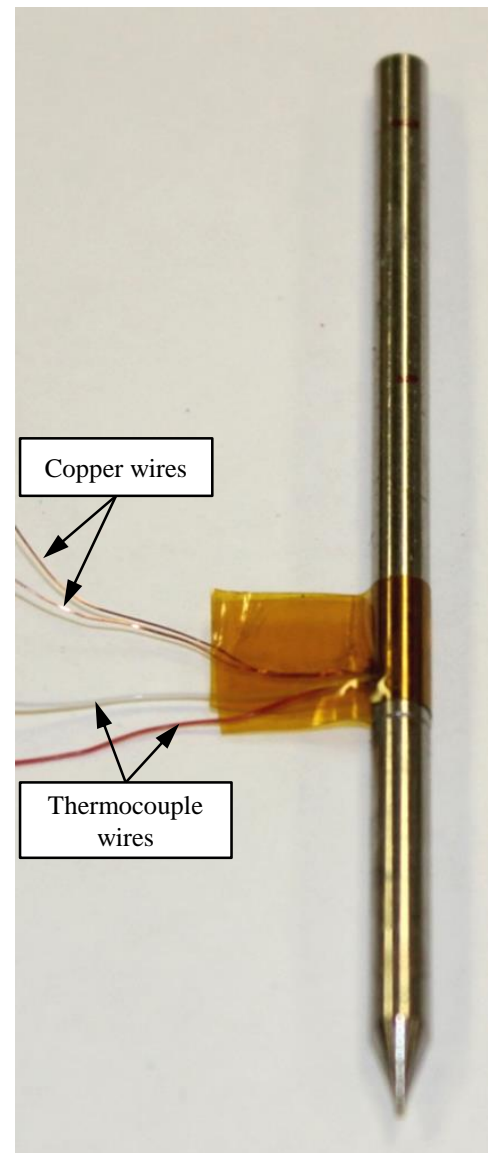
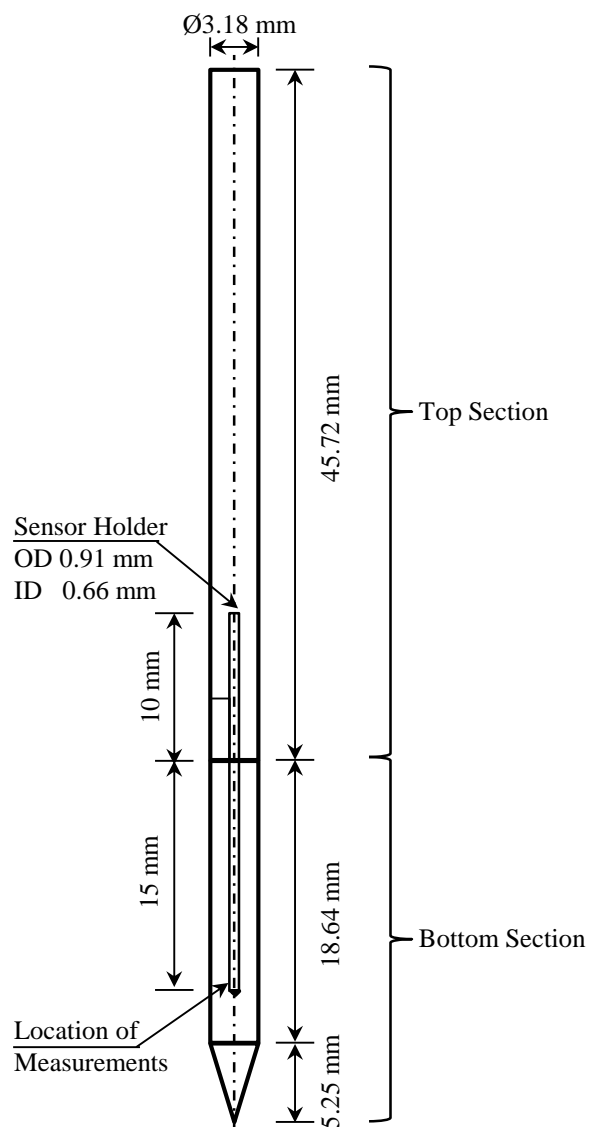


Figure 2-1 A diagram of a prototype (left) and a diagnostic nail (right)

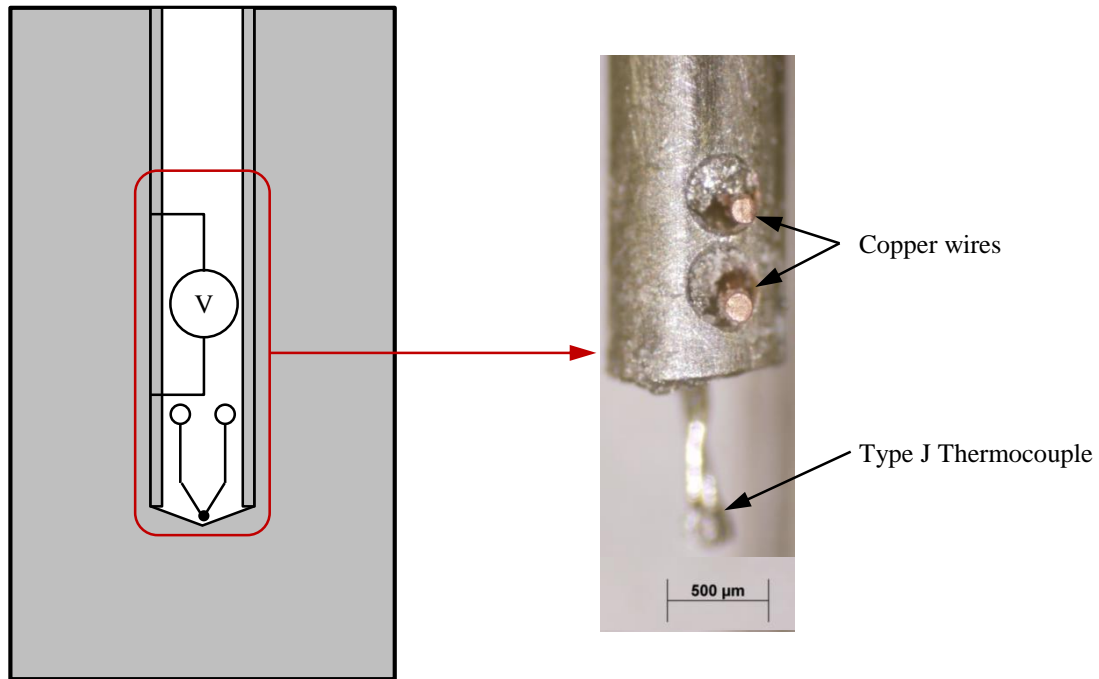


Figure 2-2 A cross section diagram at the location of measurements (left) and a sensor holder (right)

### 2.1.1 Nail Resistance Dependence on Temperature

Based on Ohm's law, electric current flow through the nail during the penetration can be determined from the ratio of the voltage drop and the nail resistance between the wires. The resistance of materials is an extrinsic property of an object which can be estimated using Equation (2-1) where  $\sigma$  is the electrical conductivity of the material,  $l$  is the distance between the copper wires and  $A_c$  is the cross-sectional area of the nail.

$$R = \frac{1}{\sigma} \left( \frac{l}{A_c} \right) \quad (2-1)$$

The electrical resistivity is the reciprocal of the electrical conductivity. Based on Matthiessen's rule [36], the temperature dependence of resistivity for metals can be expressed as shown in Equation (2-2) where  $T$  is the metal temperature,  $\beta$  is the temperature coefficient of resistivity.  $\sigma_0$  and  $T_0$  are the electrical conductivity and the temperature of the metal at 20 °C. The resistance of the nail as a function of temperatures can be expressed as shown in Equation (2-3).

$$\frac{1}{\sigma} = \frac{1}{\sigma_0} [1 + \beta(T - T_0)] \quad (2-2)$$

$$R = R_0 [1 + \beta(T - T_0)] \quad (2-3)$$

### 2.1.2 Nail Resistance Measurements

Nail resistance between the wires can be measured using four-point probe resistance measurements. Figure 2-3 shows a circuit diagram for a nail resistance measurement. The two outer probes are connected to a DC power supply. The inner probes are connected to a voltage meter. A shunt resistor is used to measure the current flow through the nail. Nail center temperature, nail surface temperature and ambient temperature are measured during a test.

The nail resistance measurement is performed by supplying constant DC current  $I$  to the outer probes at room temperature. The voltage drop  $\Delta V$  across the inner probes is measured. Based on Ohm's law, the nail resistance between two wires can be determined using Equation (2-4) as shown below.

$$R_{Nail} = \frac{\Delta V}{I} \quad (2-4)$$

Figure 2-4 demonstrates an experimental setup for nail resistance measurements. Two alligator clips are used as the outer probes. Tenma 72-6153 laboratory DC power supply is used for supplying DC current. Agilent 34330A current shunt is used to measure the current flow through the diagnostic nail. Voltage and temperature measurements during a test are logged using Agilent 34970 data acquisition with 1 Hz sampling rate.

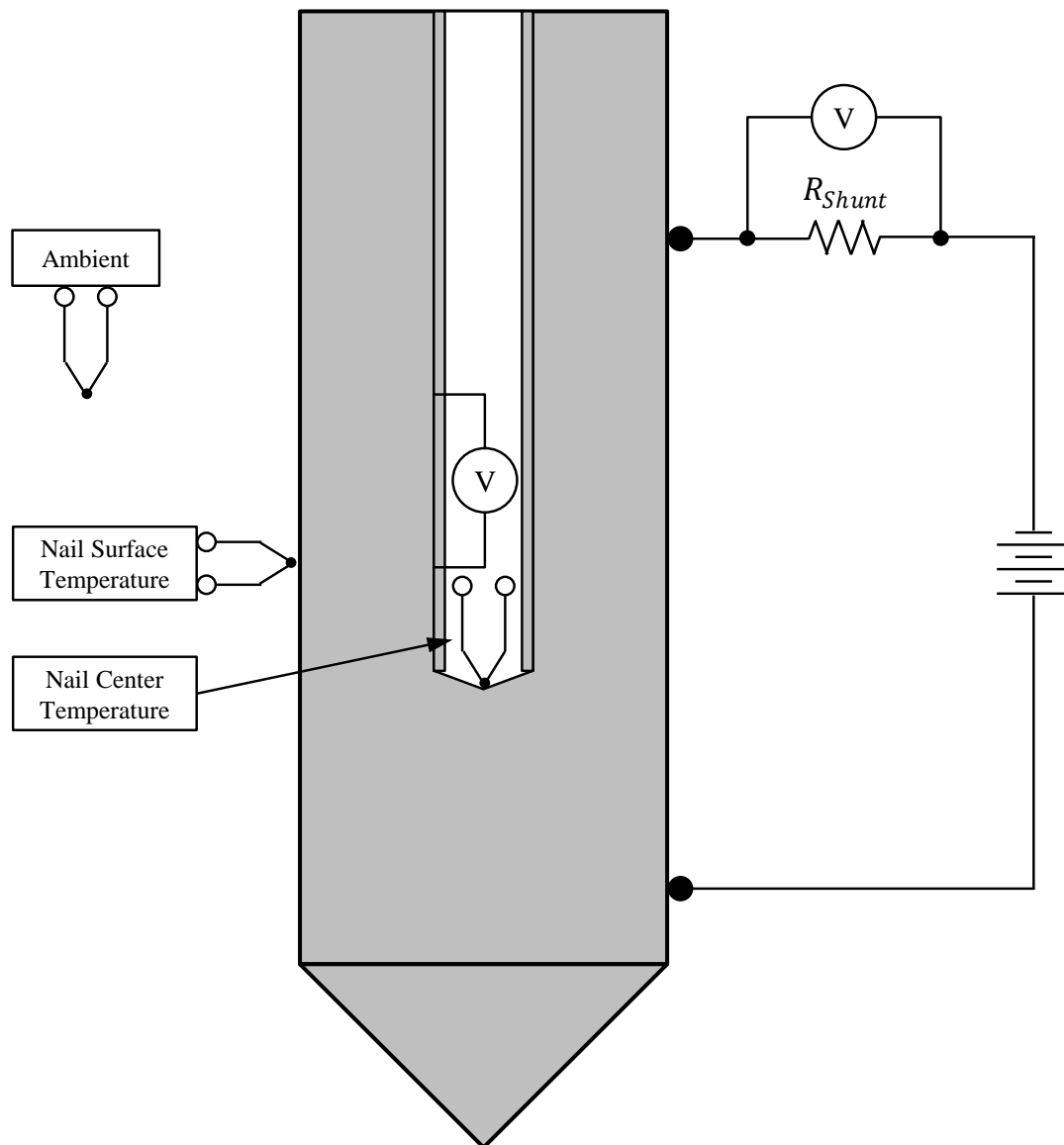


Figure 2-3 A circuit diagram for a nail resistance measurement

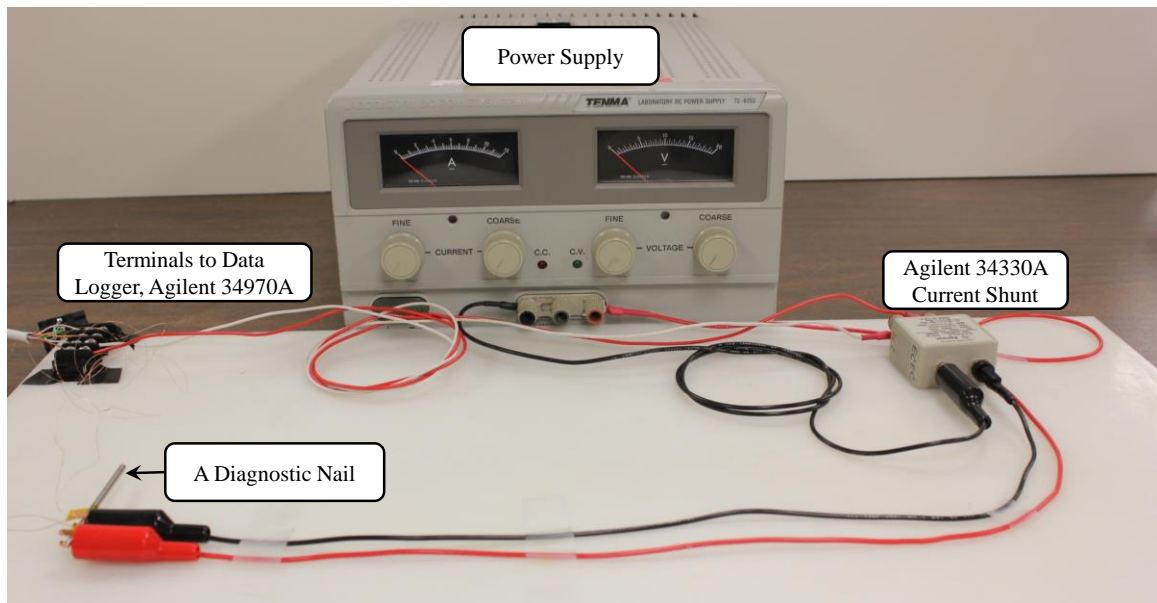


Figure 2-4 Experimental set up for nail resistance measurements

For three repeated nail resistance measurements, Figure 2-5 and Figure 2-6 show current flow through the nail and voltage drops between the inner probes. During the measurements, the nail is heated by Joule heating. Nail center temperatures, nail surface temperatures and ambient temperatures are shown in Figure 2-7, Figure 2-8 and Figure 2-9, respectively. By using Equation (2-4), the nail resistance between the inner probes as a function of nail center temperatures can be demonstrated as shown in Figure 2-10. The nail resistance measurements show good agreement with Matthiessen's rule. Table 2-1 lists nail resistance at 20 °C and temperature coefficients of resistivity for Nail #1 using least square linear fit curves. The average values are estimated from combined three measurements. With insufficient bonding strength between the inner probes and the sensor holder,  $R_0$  is increased when a distance between the inner probes is increased. The distance is increased due to stresses generated by thermal expansion of the materials. Figure 2-11 illustrates average nail resistance as a function of nail center temperatures. The error bars denote the maximum and the minimum values of least square linear fit curves for the measurements. The maximum error is 3.2%.

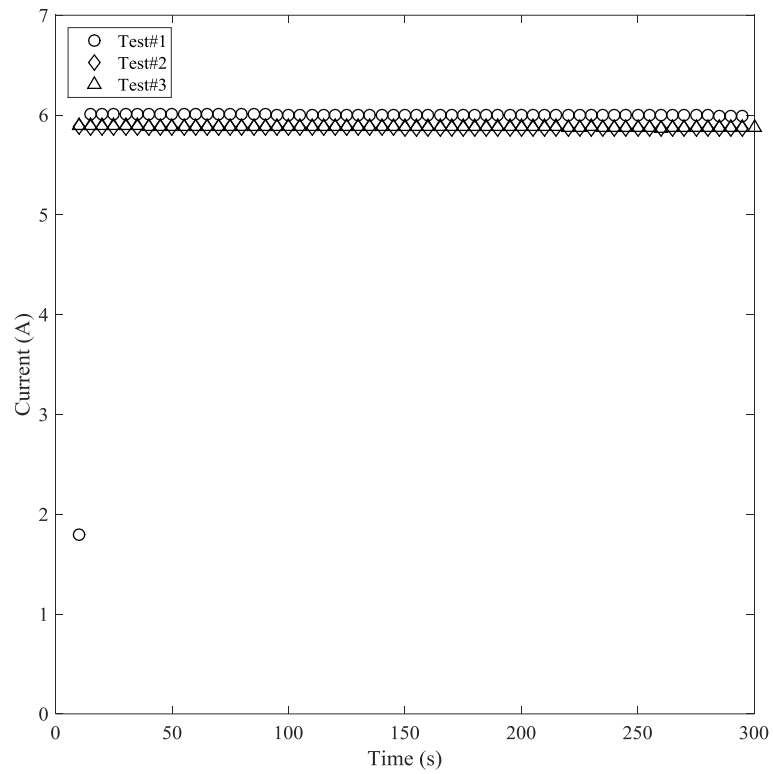


Figure 2-5 Current flow through the nail for the nail resistance measurements

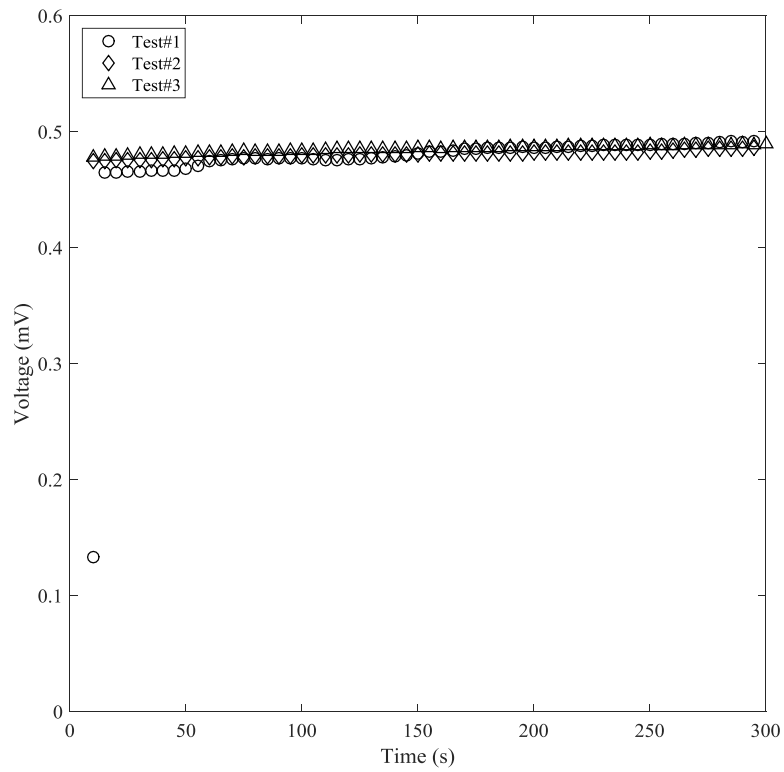


Figure 2-6 Voltage drop between the inner probes for the nail resistance measurements

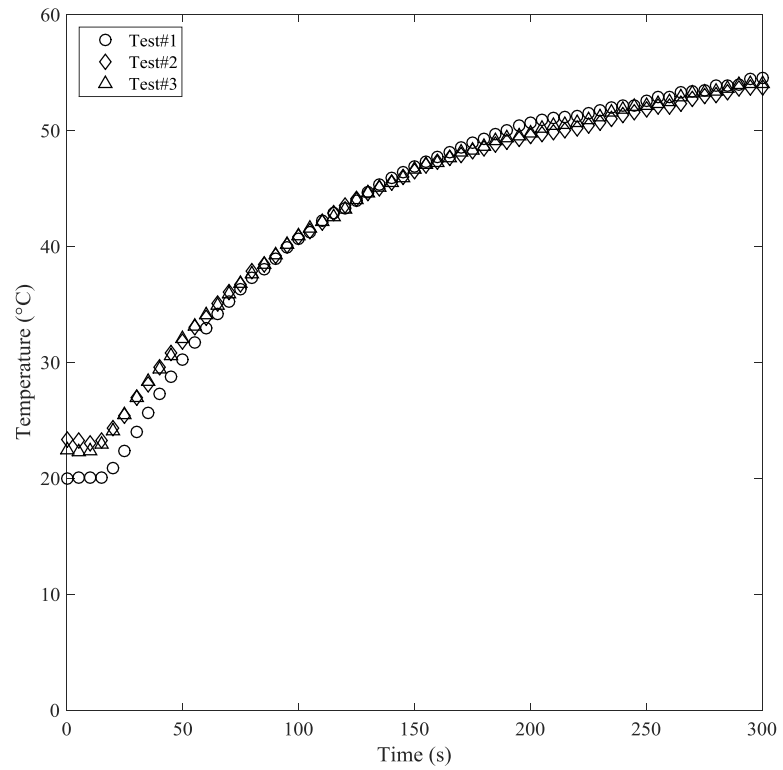


Figure 2-7 Nail center temperatures during the nail resistance measurements

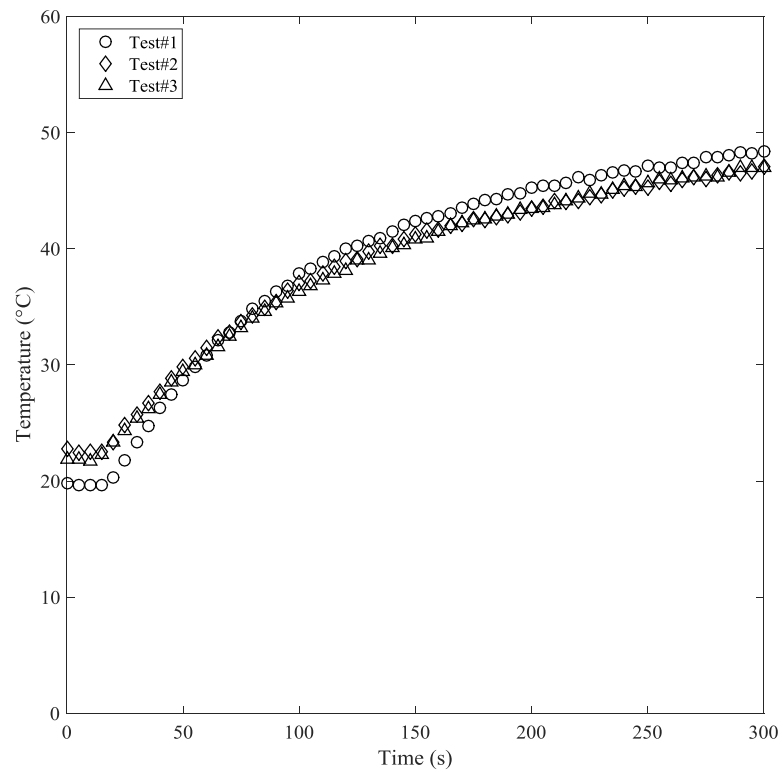


Figure 2-8 Nail surface temperatures during the nail resistance measurements

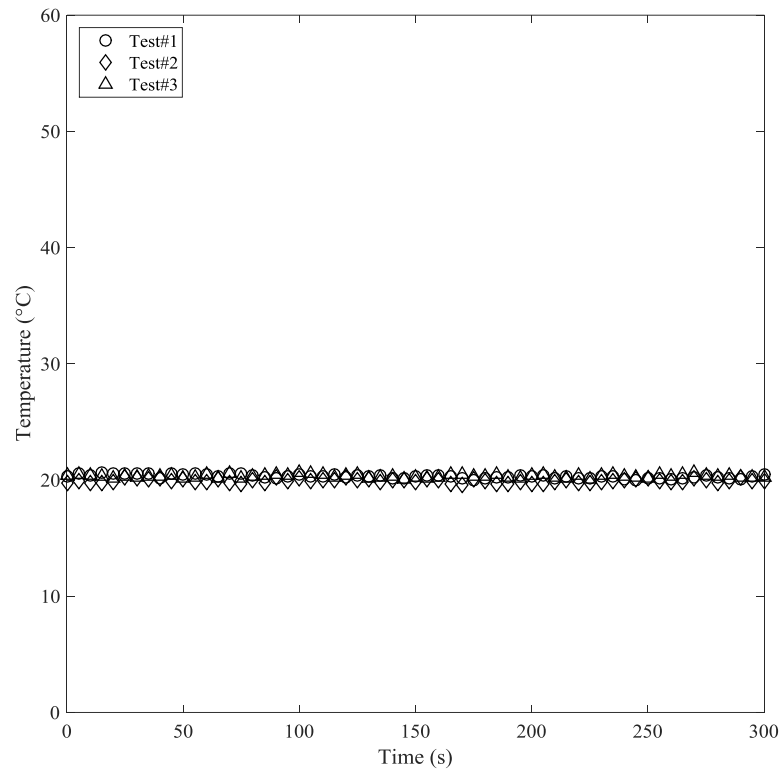


Figure 2-9 Ambient temperatures during the nail resistance measurements

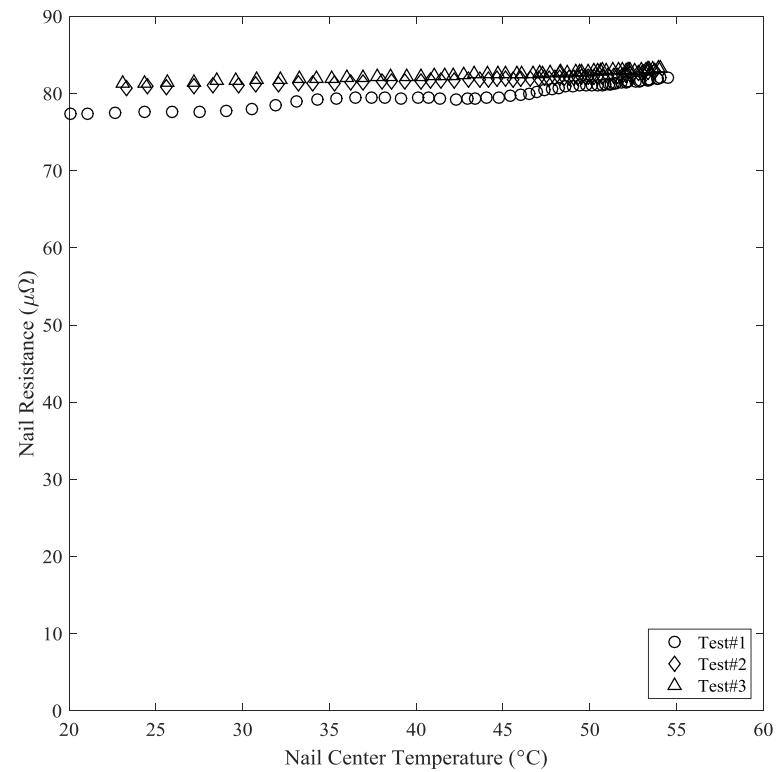


Figure 2-10 Nail resistance between the inner probes as a function of nail center temperatures

Table 2-1 Nail resistance at 20 °C and temperature coefficients of resistivity for Nail #1 using least square linear fit curves

Test #	$R_0(\mu\Omega)$	$\beta(^{\circ}\text{C}^{-1})$
1	76.74	$1.86 \times 10^{-3}$
2	80.46	$0.74 \times 10^{-3}$
3	81.06	$0.75 \times 10^{-3}$
Average	79.30	$1.17 \times 10^{-3}$

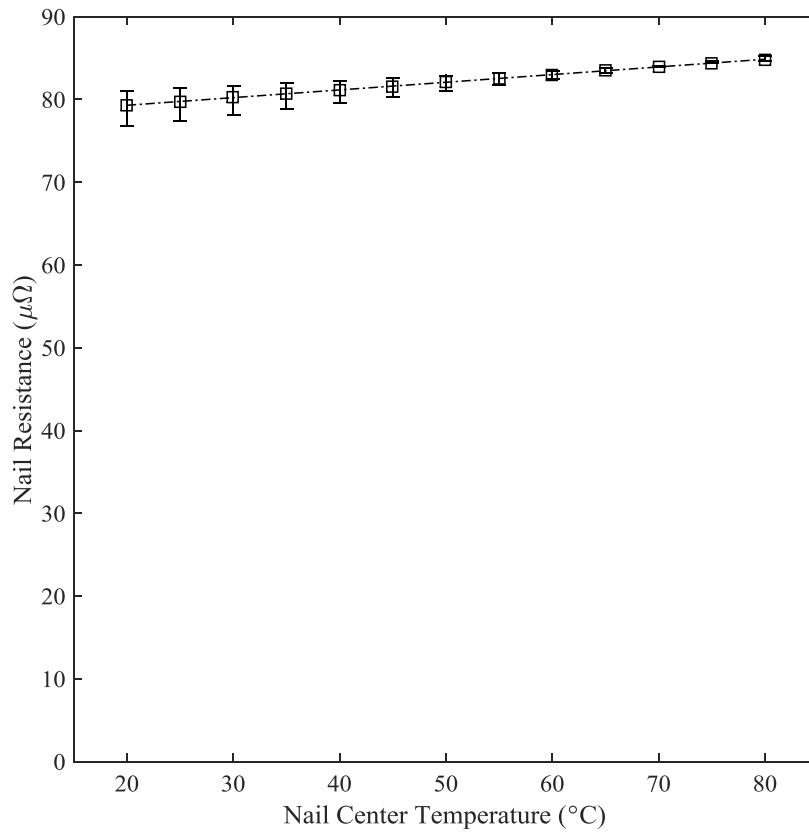


Figure 2-11 Average nail resistance as a function of nail center temperatures  
The error bars denote the maximum and the minimum values of least square linear fit curves for measurements

## 2.2. Experimental

In this present work, pouch cells are used for experimental investigation. The cathode material is Lithium Nickel Manganese Cobalt Oxide ( $\text{LiNi}_{1/3}\text{Mn}_{1/3}\text{Co}_{1/3}\text{O}_2$ ) and the anode material is graphite. Specifications of the cells are listed in Table 2-2. Before performing a nail penetration test, a cell is charged with a Constant Current – Constant Voltage (CC-CV) protocol at room temperature and rested for 2 hour. For the constant current period, a cell is charged with 3.2A current until the cell voltage reach 4.2 V. then the cell is charged with the constant voltage until the current drops to 0.16 A.

Table 2-2 Specifications of a cell for nail penetration tests

Parameter	Unit	Value
Weight	g	84
Specific energy	Wh/kg	141
Energy density	Wh/L	269
Nominal capacity	Ah	3.2
Nominal cell voltage	V	3.7
Cell dimensions	mm	8.0× 43×128

For data acquisition systems, Agilent 34970A is used for recording cell surface temperatures, nail temperatures and ambient temperature with 5 Hz sampling rate. The cell voltage and the voltage drops between the inner probes are recorded by using Measurement Computing USB-2408 DAQ Module with 10 Hz sampling rate. Figure 2-12 demonstrates locations of voltage and temperature measurements outside the nail. Thermocouples on the cell surface are used to observe temperature distribution of the cell during the penetration. The thermocouple on the nail

surface is used to investigate heat dissipation of the nail. GoPro Hero2 HD Video Camera is used to capture physical cell behaviors during the penetration. A frame rate of the video camera is 120 frame/s.

MSK-TE9002 nail penetration tester manufactured by MTI Corporation is used for conducting nail penetration tests. The tests are performed at room temperature. The penetration speed is estimated from still images recorded by the video camera. Figure 2-13 shows an experimental setup in the operation chamber of the nail penetration tester.

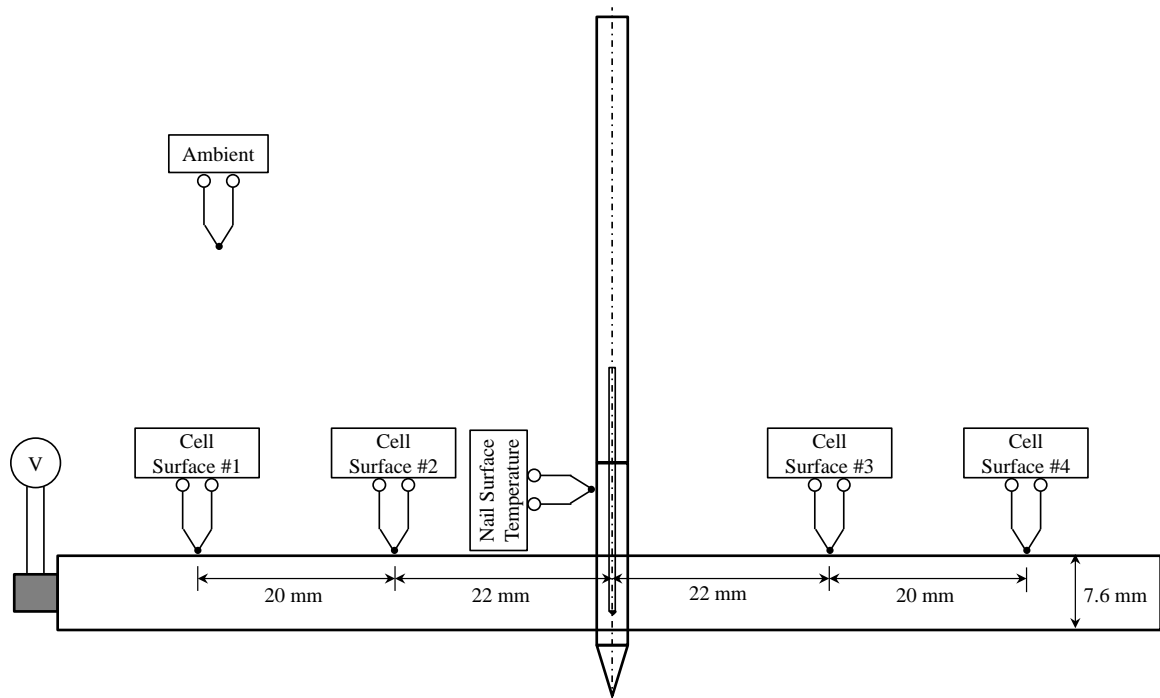


Figure 2-12 Locations of voltage and temperature measurements outside the nail

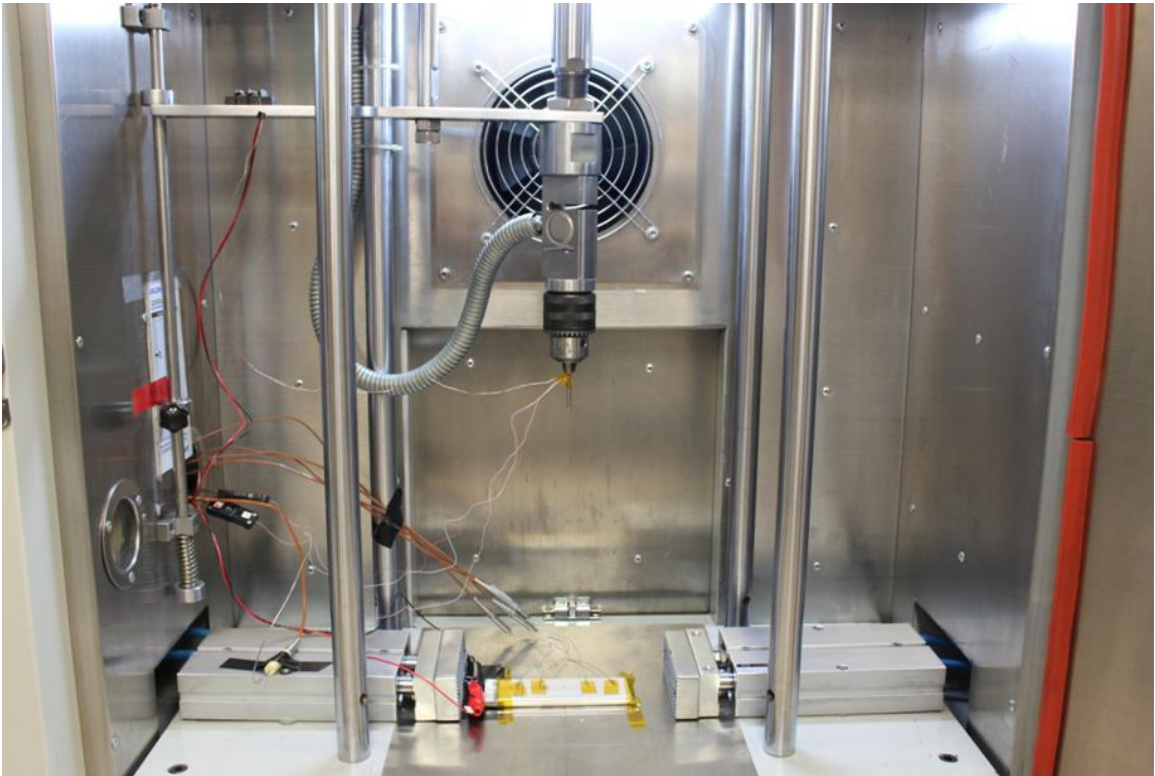


Figure 2-13 Experimental setup in the operation chamber of the nail penetration tester

### 2.3. Results and Discussion

Two nail penetration tests were conducted with different diagnostic nails. The first test is for proof of concept design. The second test is to show experimental reproducibility and to investigate repeatability of a nail penetration test.

#### 2.3.1 Nail Penetration Test #1: Proof of Concept

The purpose of the nail penetration test #1 is to demonstrate feasibility of the diagnostic nail obtaining nail temperatures and electrical current flow through the nail during the penetration. A pouch cell with its capacity of 2.724 Ah was used in this test. The actual average penetration

speed was 51.6 mm/s. The penetration depth for each time step is estimated from images captured by the video camera. Figure 2-14 illustrates penetration depth of the nail before the penetration completed at 0.3 s. After the penetration completed, a schematic of current flow path and measurements at the shorting location can be illustrated as shown in Figure 2-15. Figure 2-16 shows the current flow path in a cross section area and charge at the interface between the internal wall of the hollow nail and the external wall of the stainless steel sensor holder. Due to the current flows into the nail from the nail surface to the center of the nail, the voltage at the inner surface of the hollow nail is higher than the outer surface of the sensor holder. A layer of positive charge is formulated at the interface. Therefore, the voltage measurements at this interface is positive most of the time.

Cell surface temperatures, nail temperatures and ambient temperatures during the penetration are shown in Figure 2-17. All cell surface temperatures show normal temperature operation range, below 65 °C. With high local heat generations at the shorting location, the cell surface temperatures #2 and #3 are slightly higher than the cell surface temperatures #1 and #4. The nail center temperatures increase quickly after the penetration completed. However, thermocouples on the nail surface away from the penetration spot and the cell surface cannot detect the temperature changes from the short circuits indicating that Joule heating in the nail and exothermic reactions at the interface between the nail and the electrodes are highly localized. Random spark, gas generation and fire occur as the local temperature rapidly rises at the shorting area. The nail center temperatures drop suddenly at 2 s and 3.6 s due to noises from the temperature measurements. Due to the cell is swelling at 1.2 s and the fire at 1.242 s, the nail surface temperatures rise rapidly because the thermocouple at the nail surface is covered by the cell packaging. Later, the nail surface temperatures decrease as heat is released underneath the cell. Figure 2-21 and Figure 2-22 show cell characteristics of the nail penetration #1 from 0 s until 4.4 s.

Based on the nail center temperatures, nail resistance between the inner probes during the nail penetration test #1 can be estimated as shown in Figure 2-18. The sampling rate of nail center temperatures is increased to 10 Hz using a linear interpolation. The nail resistance is estimated using Equation (2-4) and parameters listed in Table 2-1. The error bars denote the maximum and the minimum values of least square linear fit curves from the nail resistance measurements.

The cell voltage and average shorting current for the nail penetration test #1 are shown in Figure 2-19. The positive current means the current flows upward through the nail and vice versa. At the beginning of the penetration, the cell voltage drops instantaneously because high inrush current is generated. After full penetration is completed, the cell voltage recovers because the kinetic/transport properties of the cell increase due to rapid local temperature rises. Later, the shorting current, in C-rate, is decreased due to depleting discharge of the cell. The cell voltage decreases gradually as the discharge process continues. The sudden drops of the shorting current at a few time instants are due to random sparks and fire which cause periodic loose contacts between the nail and cell components. To account for errors from nail resistance measurements, errors of the shorting current estimation for the nail penetration test #1 are shown in Figure 2-20. The errors of estimation are within  $\pm 15\%$  of the averaged shorting current.

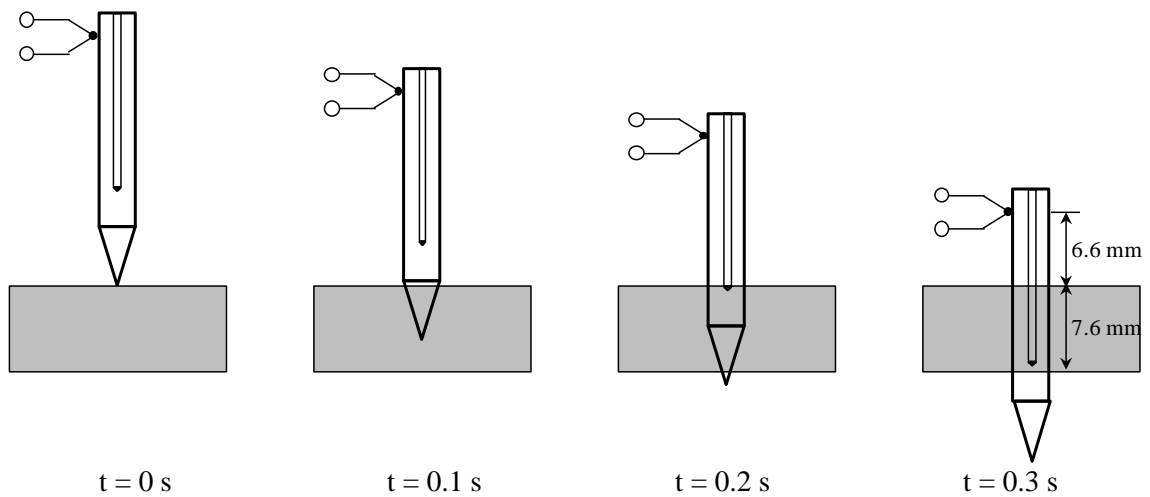


Figure 2-14 Penetration depth of the nail before the penetration completed

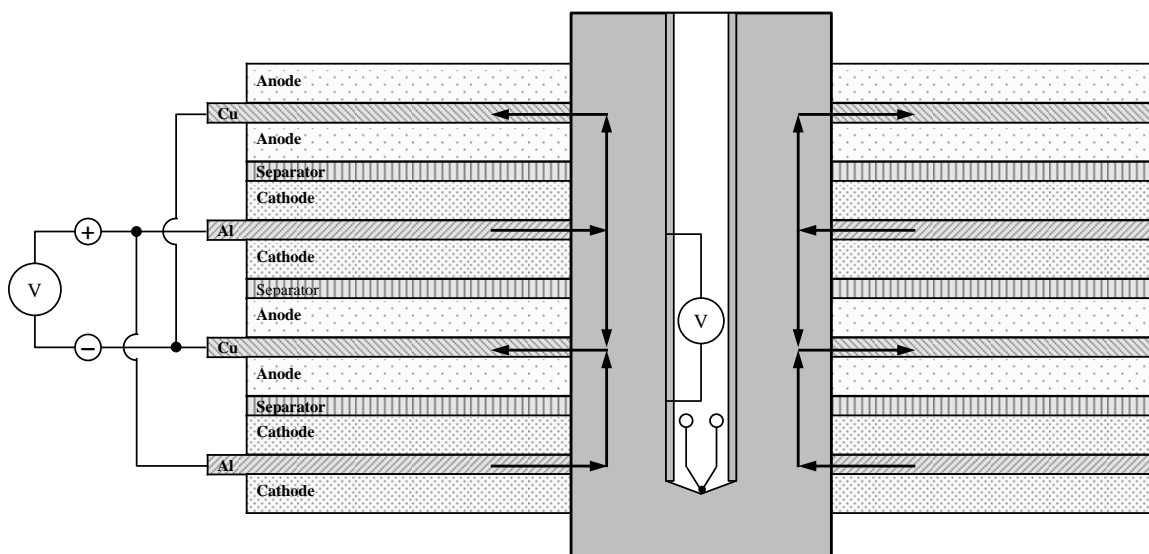


Figure 2-15 Schematic of current flow path and measurements at the shorting location

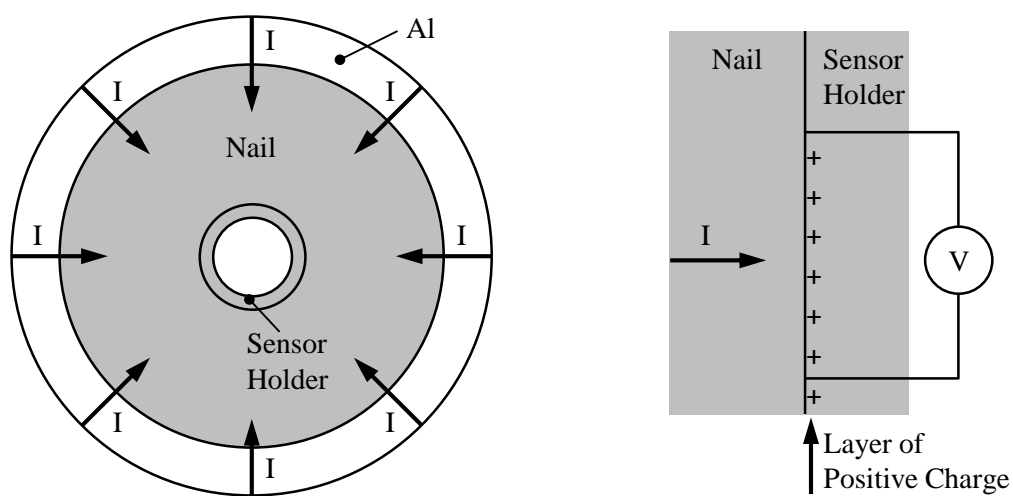


Figure 2-16 Current flow path in a cross section area (left) and charge at the interface between the internal wall of the hollow nail and the external wall of the stainless steel sensor holder (right)

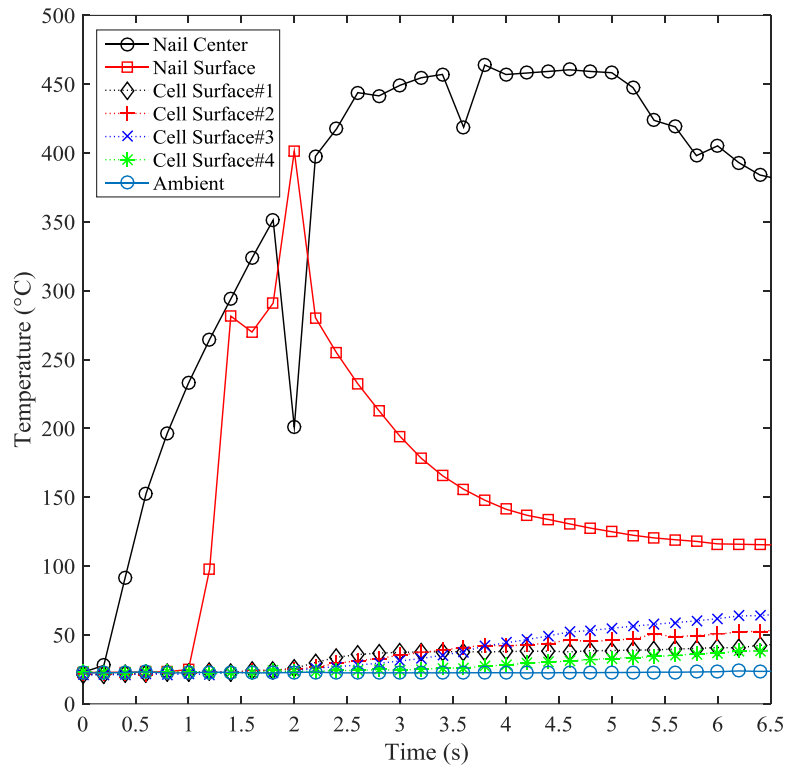


Figure 2-17 Nail temperatures, cell surface temperatures and ambient temperatures

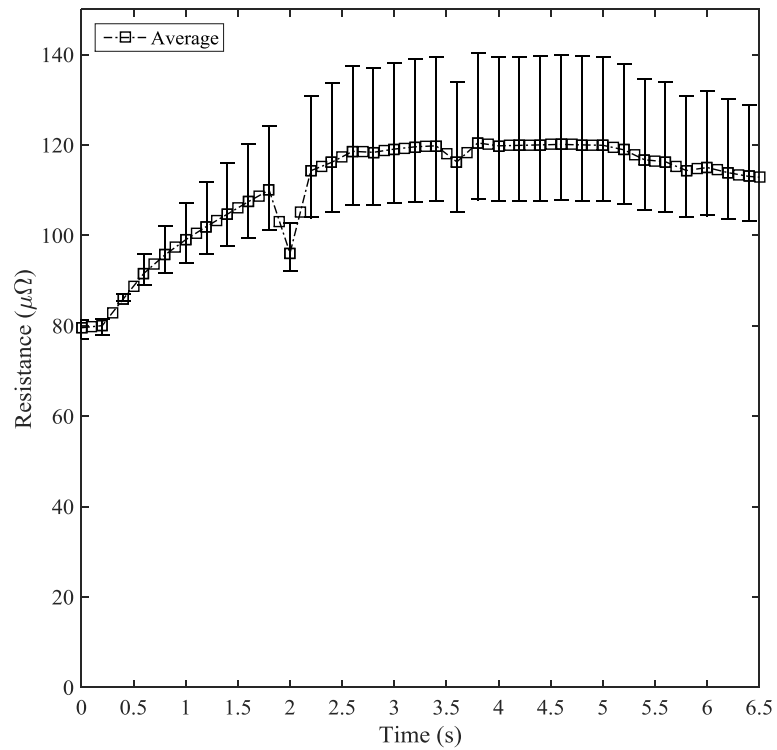


Figure 2-18 Nail resistance between the inner probes during the nail penetration test #1

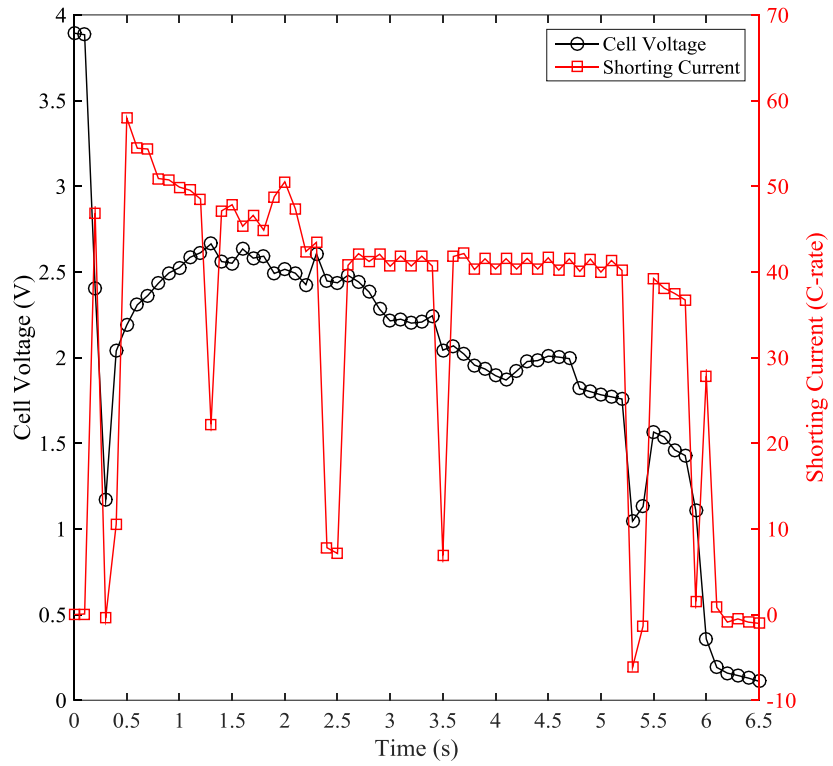


Figure 2-19 Cell voltage and average shorting current for the nail penetration test #1

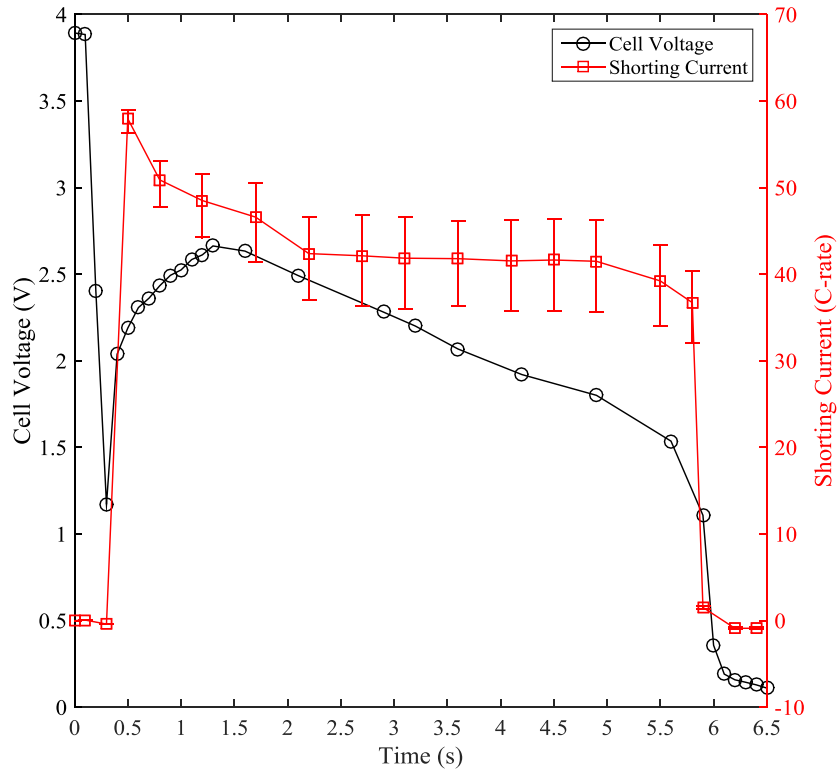
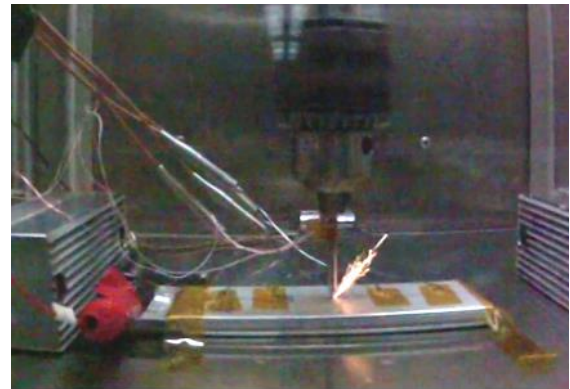


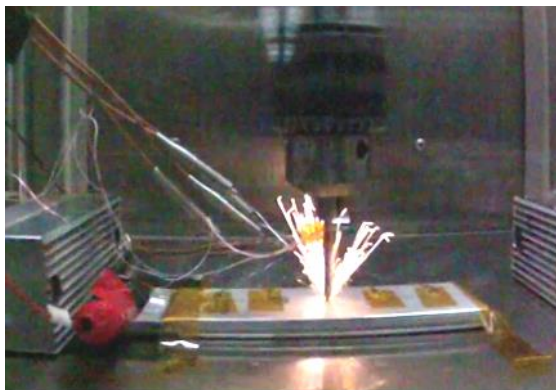
Figure 2-20 Errors of the shorting current estimation for the nail penetration test #1



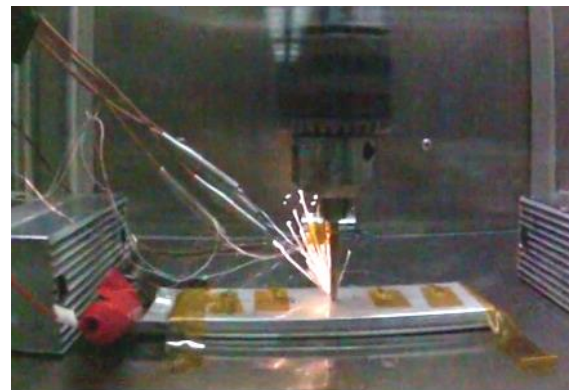
Time = 0.067 s  
First spark



Time = 0.075 s  
Spark continued



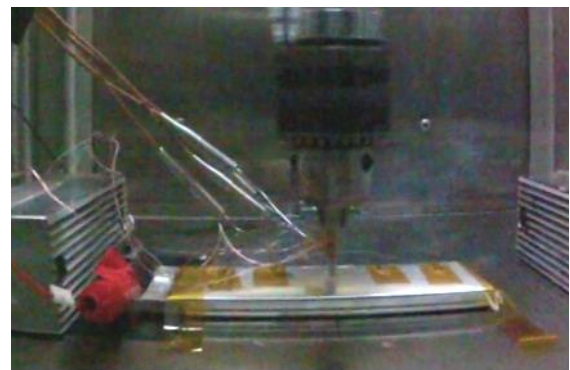
Time = 0.083 s  
Spark continued



Time = 0.092 s  
Spark continued

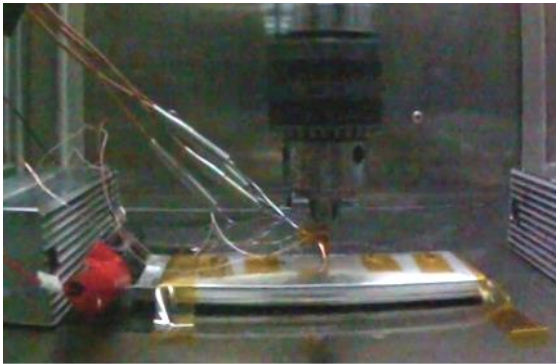


Time = 0.167 s  
Smoke initiated

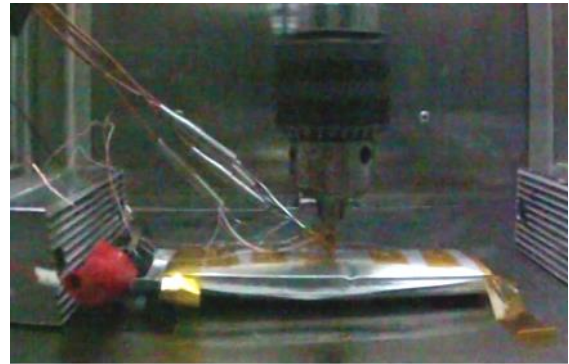


Time = 0.300 s  
Full penetration is completed

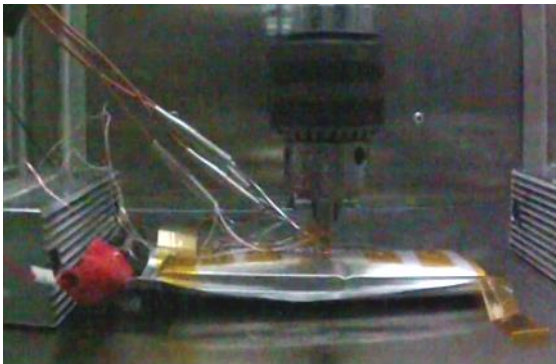
Figure 2-21 Cell characteristics of the nail penetration #1 during 0 s to 0.3 s



Time = 1.067 s  
Spark



Time = 1.200 s  
Swelling



Time = 1.242 s  
Fire Initiated



Time = 2.458 s  
Spark



Time = 4.000 s  
Seal Broken



Time = 4.400 s  
Spark

Figure 2-22 Cell characteristics of the nail penetration #1 during 0.1 s to 4.4 s

### 2.3.2 Nail Penetration Test #2: Repeatability and Reproducibility

A second diagnostic nail, Nail#2, was manufactured to demonstrate experimental reproducibility. Figure 2-23 shows dimensions of components for Nail #1 and Nail #2. Note that Nail #1 was used for the nail penetration test #1. Nail resistance comparison between Nail #1 and Nail #2 is shown in Figure 2-24. The error bars denote the maximum and the minimum values of least square linear fit curves for measurements. The resistance measurements of Nail #2 show small errors because the bonding strength between the inner probes and the sensor holder is improved. Table 2-3 lists the nail resistance at 20 °C and temperature coefficients of resistivity for Nail #2 using least square linear fit curves.

For the nail penetration test#2, a pouch cell with its capacity of 2.94 Ah was used to investigate repeatability of the nail penetration test. Experimental setup for the repeatability test is shown in Figure 2-25. The light was installed in the operation chamber for improving image quality of the video camera. Cell surface temperatures, nail temperatures and ambient temperature are measured and recorded every 0.3 s using Agilent 34970A. The average penetration speed for this test is 51.3 mm/s. The penetration depth of Nail #2 before the penetration completed is illustrated in Figure 2-26. Cell characteristics of the nail penetration #2 during 0 s to 3.6 s are shown in Figure 2-27.

Nail center temperatures and nail surface temperatures of Test#1 and Test#2 during nail penetration tests are compared and shown in Figure 2-28 and Figure 2-29. The actual nail temperatures of Test#2 exceed the range of measurements for the Type J thermocouple used in Nail#2. For temperatures above 700 °C, the nail temperatures are assumed to be constant at 800 °C. At the beginning of the penetration in Test #2, the nail temperature profiles of Test#2 similar to the nail temperature profiles in Test#1. However, the nail temperatures of Test#2 increase with higher heat generation rate. For both tests, the nail center temperatures drop suddenly at 350 °C.

Comparisons of cell surface temperatures between Test#1 and Test#2 are shown in Figure 2-30. All cell surface temperatures for both tests show similar profiles. The cell surface #1 and #4 for both tests demonstrate high repeatability. The slightly differences of the cell surface #2 and #3 is due to non-uniform heat generation at the shorting current.

Comparison of average nail resistance during the penetration of Test #1 and Test #2 is shown in Figure 2-31. With undetermined actual nail center temperatures in Test#2, the nail resistance of Nail #2 is estimated to constant for temperatures above 700 °C.

Cell voltage comparison and average shorting current comparisons between Test #1 and Test #2 are shown in Figure 2-32 and Figure 2-33. The cell voltage drops at the initial stage in Test#2 is lesser than in Test#1 indicating that the shorting resistance in Test#2 is higher than the shorting resistance in Test#1. After the penetration is completed, the recover voltage for both tests is the same value at 1.493 V. The average shorting current is approximately 40 C-rate. Due to high fluctuations of the shorting current in Test#2, the cell is discharged faster than the cell in Test#1. To determine the cumulative discharge capacity for Test #1 and Test #2, the trapezoidal numerical integration is used to integrate Equation (2-5). Figure 2-34 shows the cumulative discharge capacity for Test #1 and Test #2. The normal discharge capacity of the cell used in Test #2 is higher than the cell used in Test #1 by 8%. For nail penetration tests, however, the cell discharge capacity in Test #2 is approximately the same as the discharge capacity in Test #1. Figure 2-35 demonstrates the cumulative discharge capacity for Test #1 and Test #2 as a function of cell voltages.

$$Discharge\ Capacity = \int I(t) dt \quad (2-5)$$

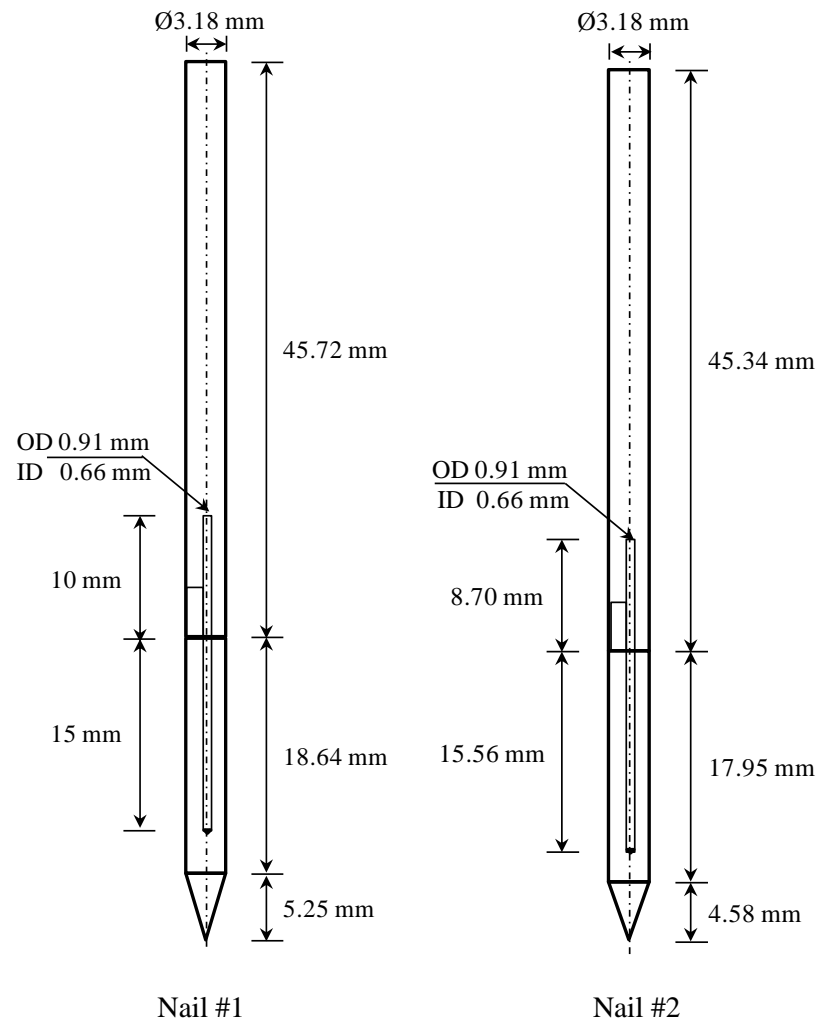


Figure 2-23 Dimension components of Nail #1 and Nail #2

Table 2-3 Nail resistance at 20 °C and temperature coefficients of resistivity for Nail #2 using least square linear fit curves

Test #	$R_0(\mu\Omega)$	$\beta(^{\circ}\text{C}^{-1})$
1	60.15	$0.97 \times 10^{-3}$
2	60.11	$1.02 \times 10^{-3}$
3	60.15	$1.05 \times 10^{-3}$
Average	60.17	$1.00 \times 10^{-3}$

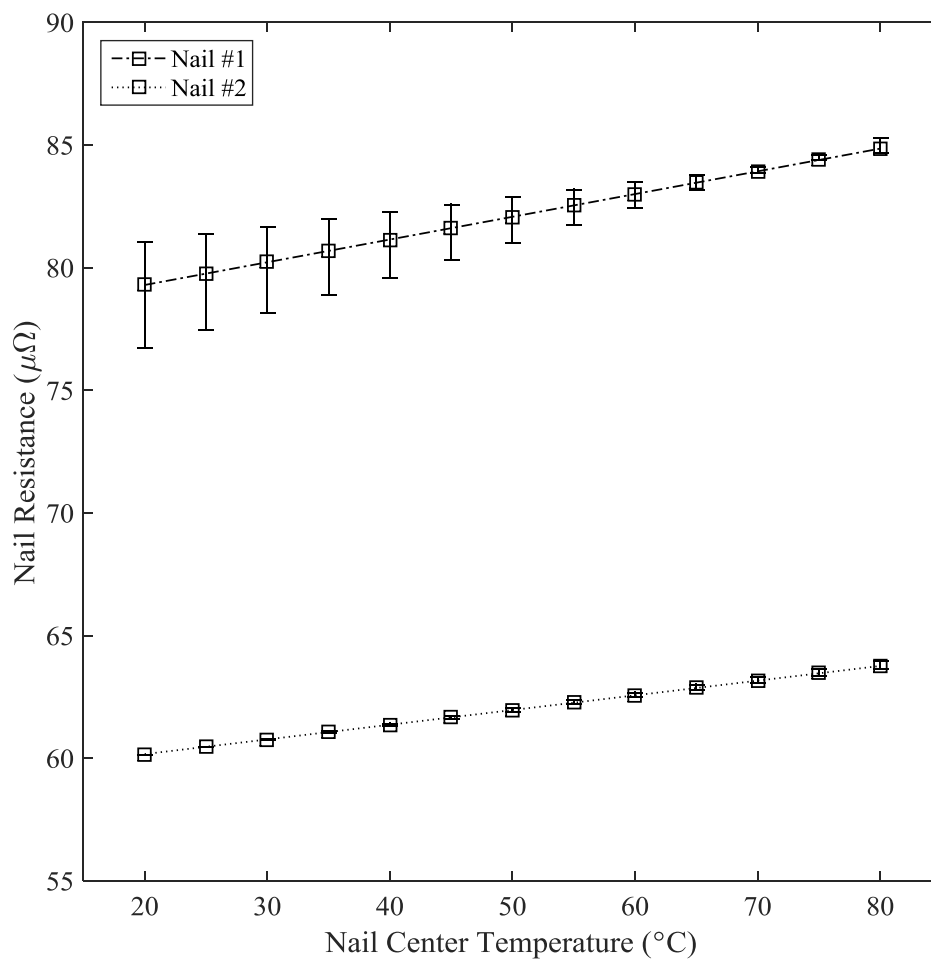


Figure 2-24 Average nail resistance comparison between Nail #1 and Nail #2

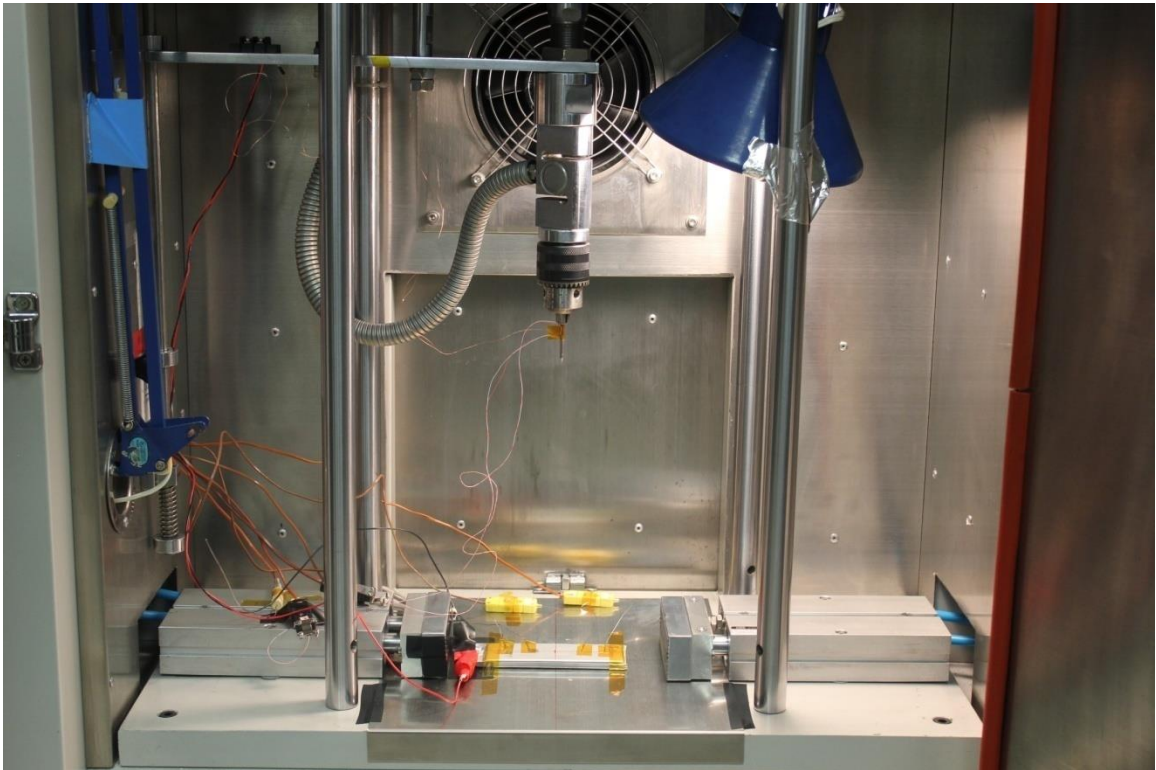


Figure 2-25 Experimental setup for the repeatability test

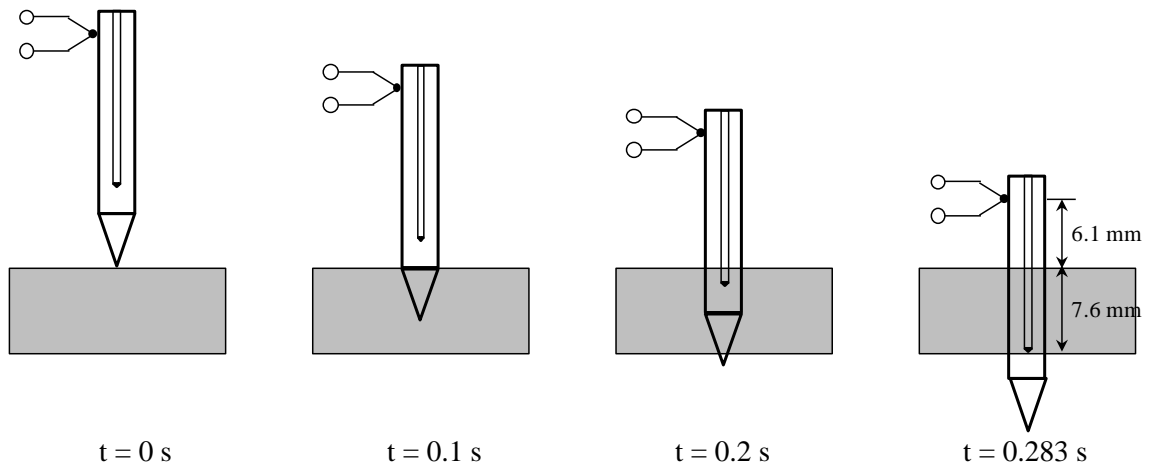
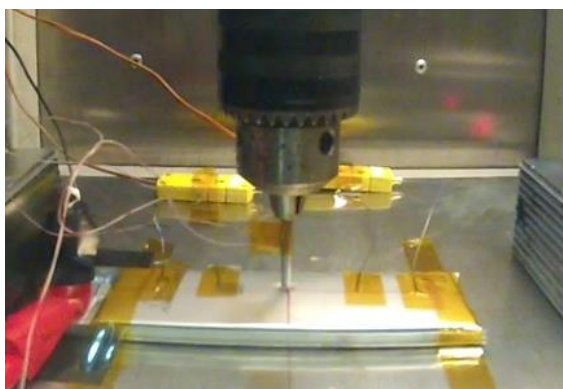
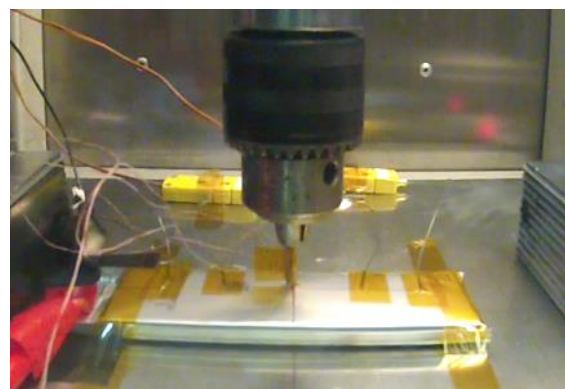


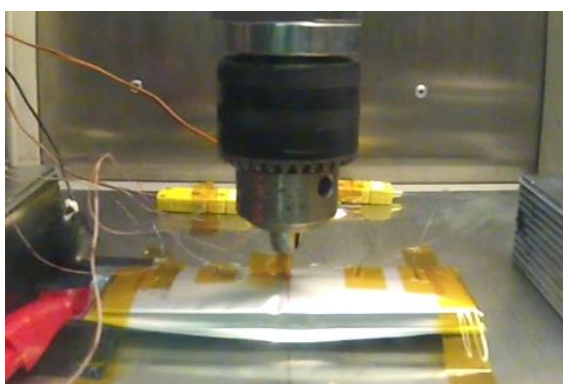
Figure 2-26 Penetration depth of Nail #2 before the penetration completed



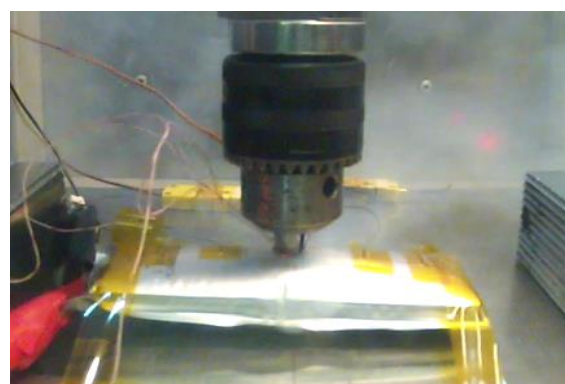
Time = 0.158 s  
Smoke Initiated



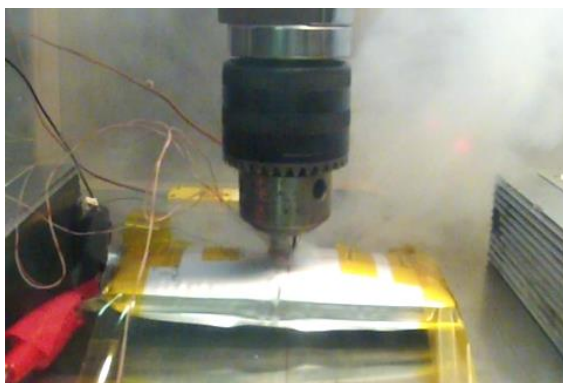
Time = 0.283 s  
Penetration Completed



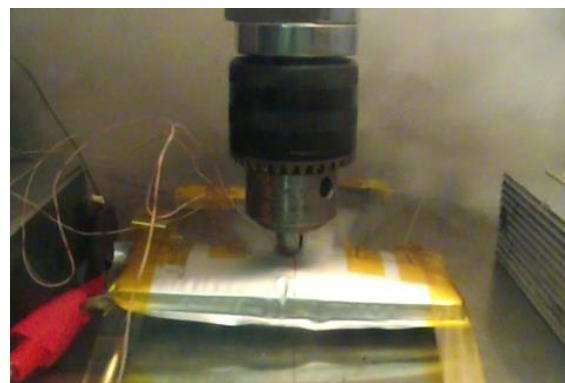
Time = 1.083 s  
Swelling



Time = 1.842 s  
Fire



Time = 2.400 s  
Smoking



Time = 3.600 s  
Smoking

Figure 2-27 Cell characteristics of the nail penetration #2 during 0 s to 3.6 s

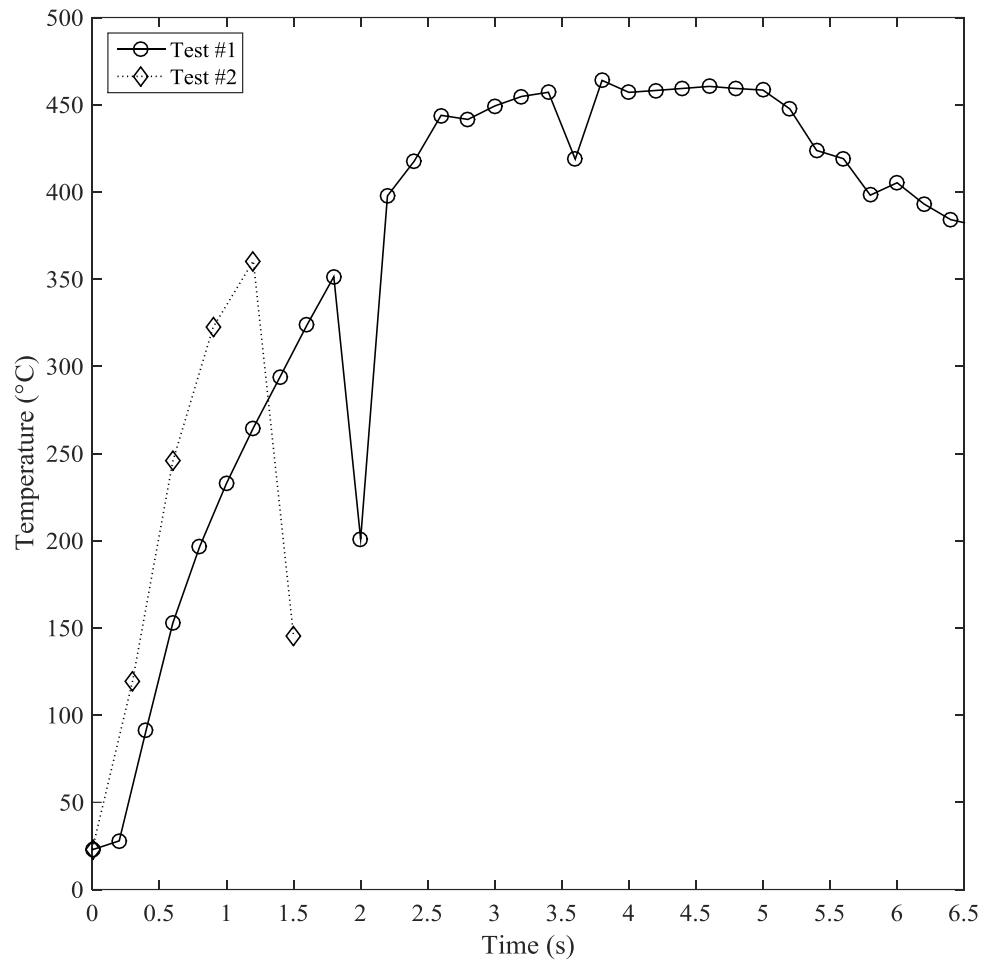


Figure 2-28 Nail center temperatures comparison between Test#1 and Test#2

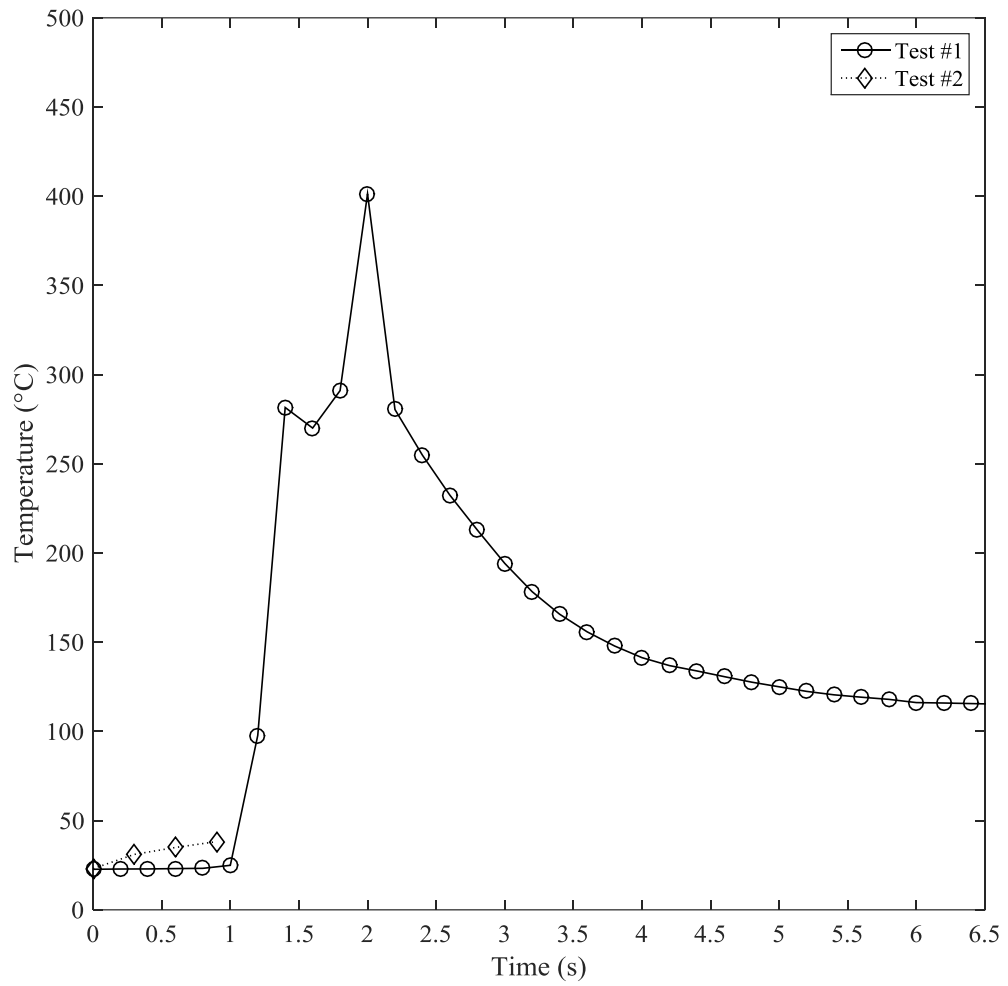


Figure 2-29 Nail surface temperatures comparison between Test#1 and Test#2

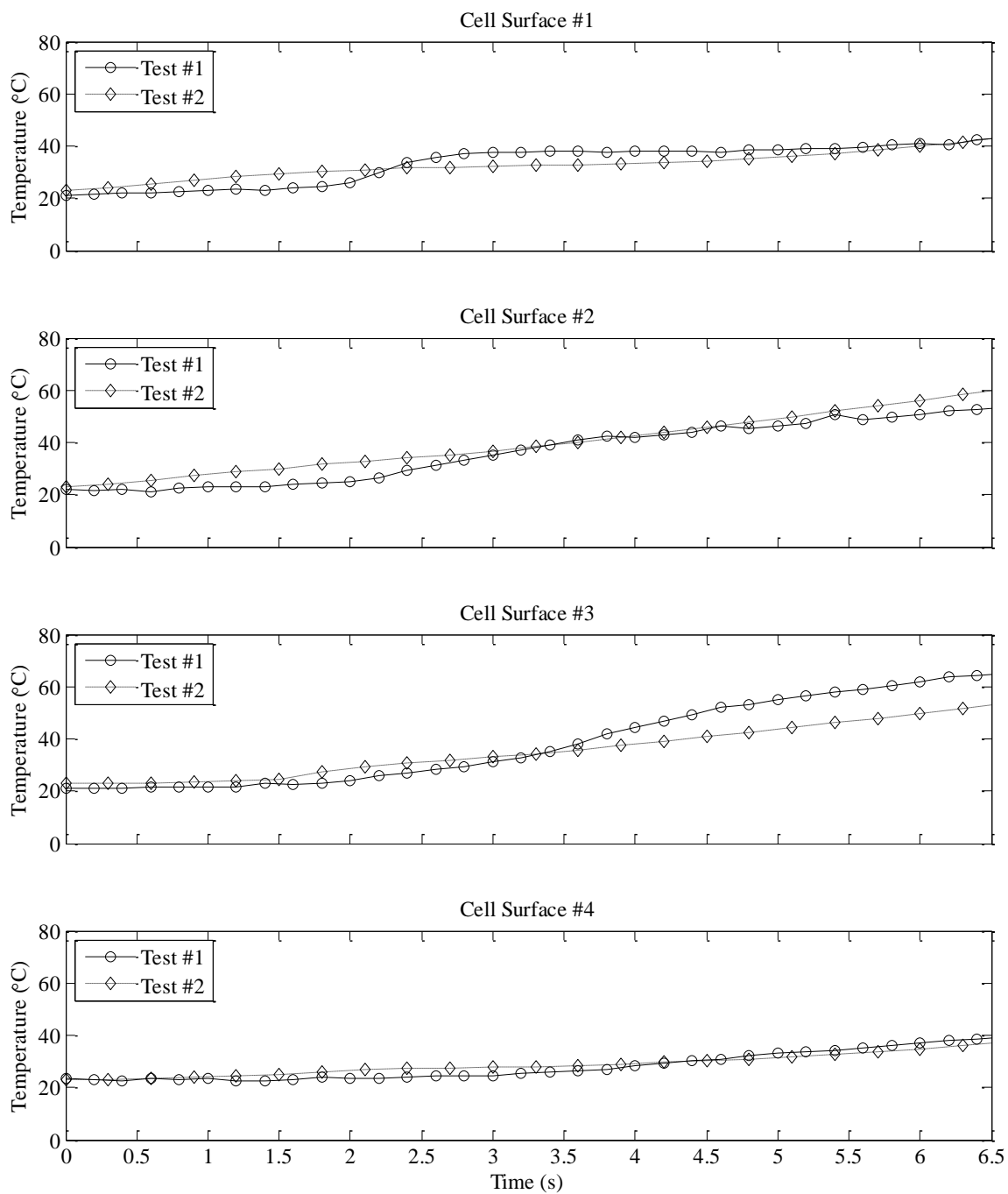


Figure 2-30 Comparisons of cell surface temperatures between Test#1 and Test#2

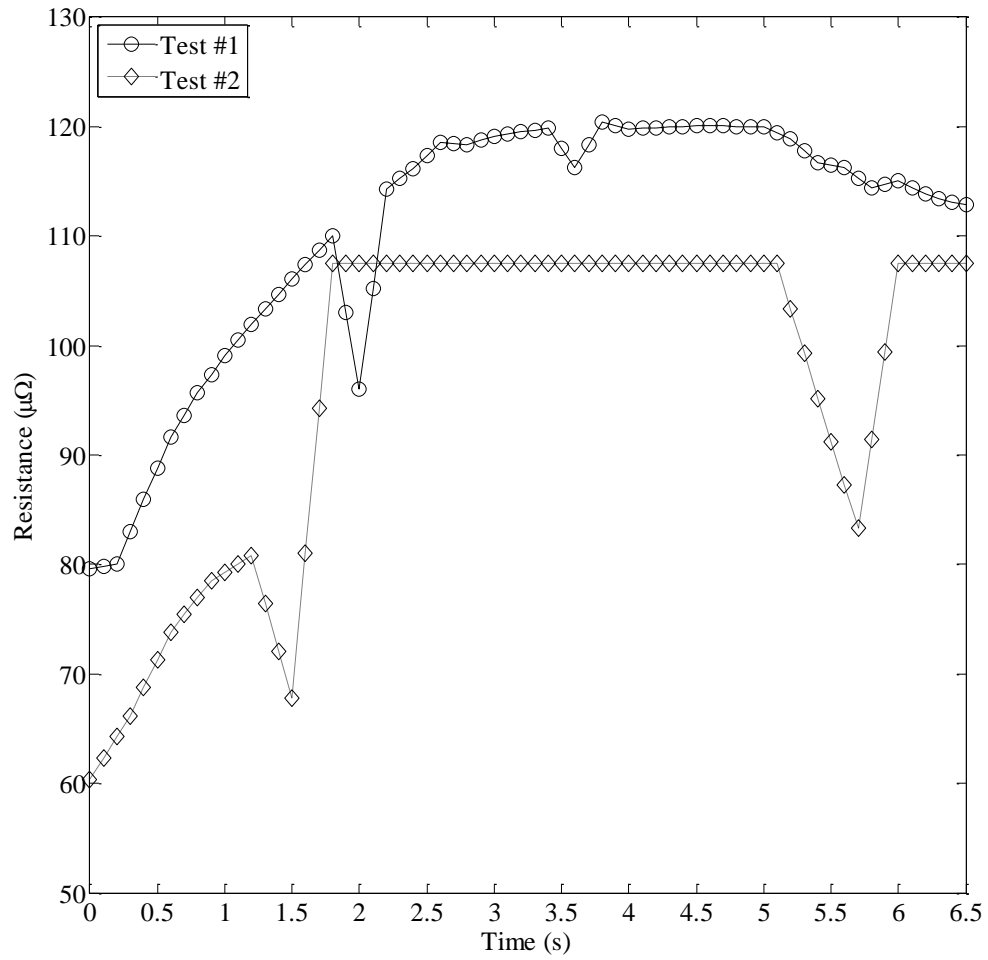


Figure 2-31 Comparisons of average nail resistance during the penetration of Test #1 and Test #2

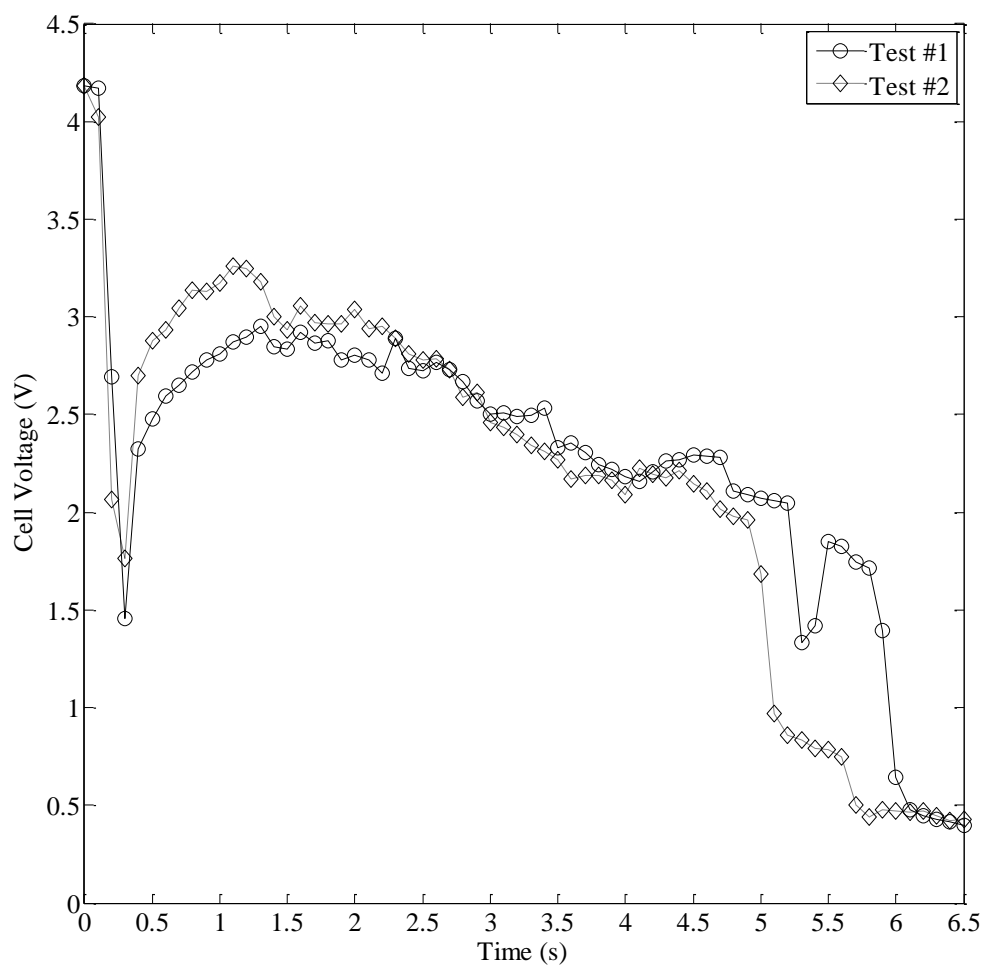


Figure 2-32 Cell voltage comparison between Test #1 and Test #2

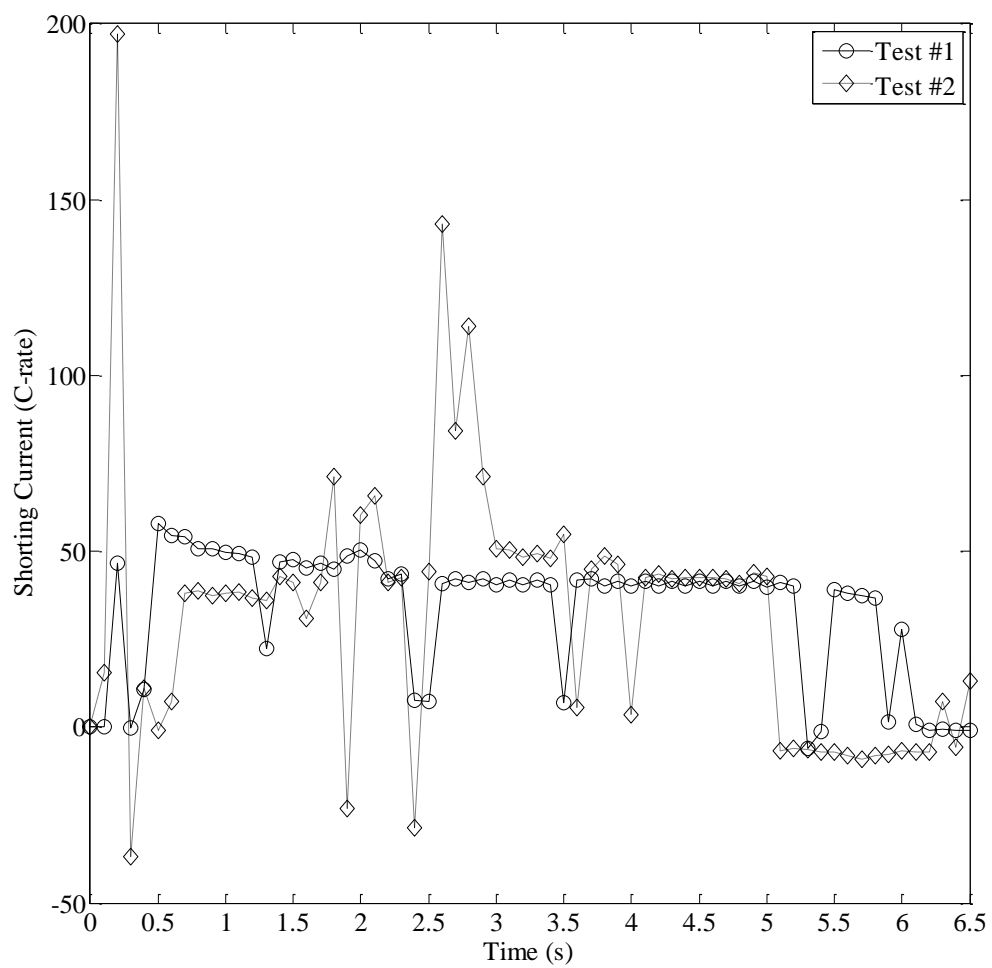


Figure 2-33 Average shorting current comparison between Test #1 and Test #2

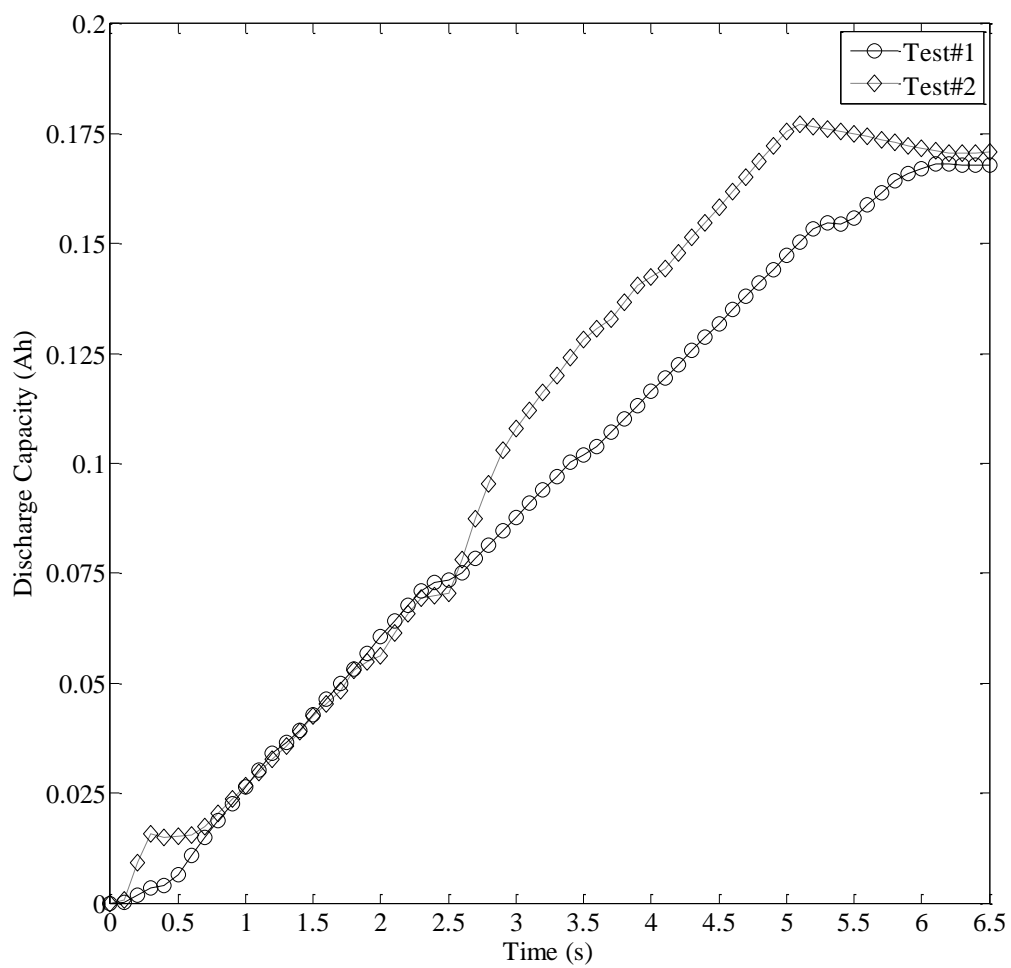


Figure 2-34 Cumulative discharge capacity comparison between Test #1 and Test #2

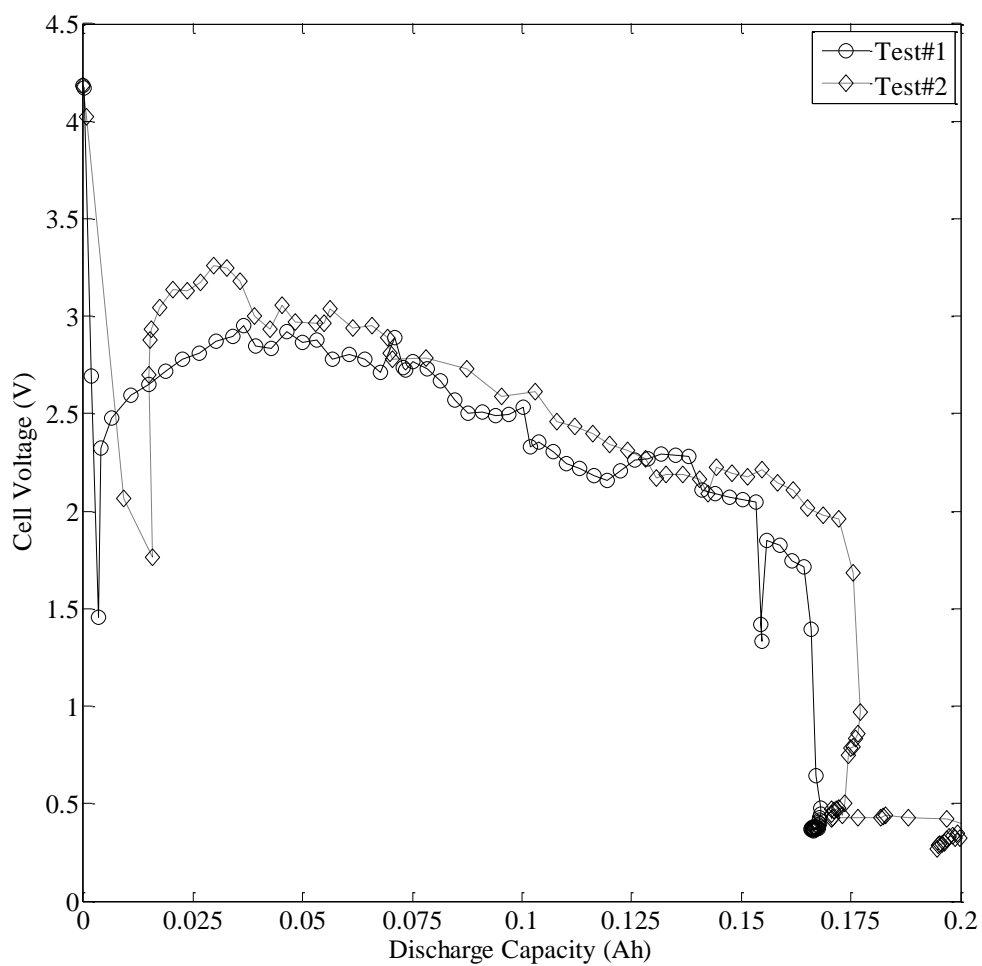


Figure 2-35 Cumulative discharge capacity as a function of cell voltages for Test #1 and Test #2

## 2.4. Summary

A prototype of a diagnostic nail is developed for investigating cell characteristics at a shorting current. The installation of two wires and one thermocouple into the center of the nail enables to obtain nail temperatures at the shorting spot and to estimate the shorting current flow through the nail. The fluctuation of the shorting current is due to random sparks and fire caused loose contacts between the nail and cell the components.

Comparisons of two nail penetration tests using two different diagnostic nails show that the reproducibility of tests is still very challenging. Experimental data reveals that the shorting resistance at the initial stage is a critical parameter to obtain repeatable results. After the penetration completed, the average shorting current for both tests is approximately 40 C-rate. The magnitude of the fluctuation of the shorting current cannot be estimated. In order to generate scientifically meaningful data, both the diagnostic nail and experimental procedures still need improvement.

## Chapter 3

### Effects of Nail Composite Wall on Cell Characteristics during a Nail Penetration Test

A new structure of a diagnostic nail is developed to improve operating temperatures of the sensors and to reduce noise from the measurements. The sensor holder material is changed from 304 stainless steel to a miniature ceramic tube. The Type J thermocouples used in the prototype are replaced with Type K thermocouples to measure nail temperatures above 700 °C. To improve accuracy of nail resistance measurements, the wires are bonded to the ceramic holder using high temperature cement. An electrical strain relief is installed for improving stability of voltage and temperature measurements. New experimental results are compared with the experimental results of Test #1. Moreover, energy balance of the diagnostic nails for the tests are presented.

#### 3.1. A Diagnostic Nail with Ceramic Sensor Holder

A new diagnostic nail, Nail #3, is made of a 304 stainless steel rod with 3.18 mm in diameter. Figure 3-1 shows a diagram of a new design nail and a new diagnostic nail. To fabricate the nail, a ceramic sensor holder is inserted into a hollow nail by press fitting. With implementing the ceramic holder, the wall thickness of the nail is decreased by 37% comparing with the prototype. The material of the ceramic holder is OMEGATITE® 200. An electrical strain relief is installed to provide a secure hold for the wires when they are pulled or in motion. Figure 3-2 demonstrates a cross section diagram at the location of measurements for the new nail design and a ceramic sensor holder. A Type K thermocouple is installed into the ceramic holder to increase the range of

temperature measurements. The outer diameter of the thermocouple is 254  $\mu\text{m}$  and the diameter of copper wires is 127  $\mu\text{m}$ . The wires and the thermocouple are bonded to the ceramic holder using OMEGABOND<sup>®</sup> 600 high temperature cement.

The nail resistance between the inner probes are measured using the methodology described in Chapter 2. Figure 3-3 and Figure 3-4 show the current flow through the nail and voltage drops between the inner probes for three repeated measurements. Nail center temperatures, nail surface temperatures and ambient temperatures during the measurements are shown in Figure 3-5, Figure 3-6 and Figure 3-7 respectively. The nail resistance between the inner probes as a function of nail center temperatures is shown in Figure 3-8. The nail resistance measurements show good agreement with Matthiessen's rule. Table 3-1 lists the nail resistance at 20 °C and temperature coefficients of resistivity for Nail #3 using least square linear fit curves.

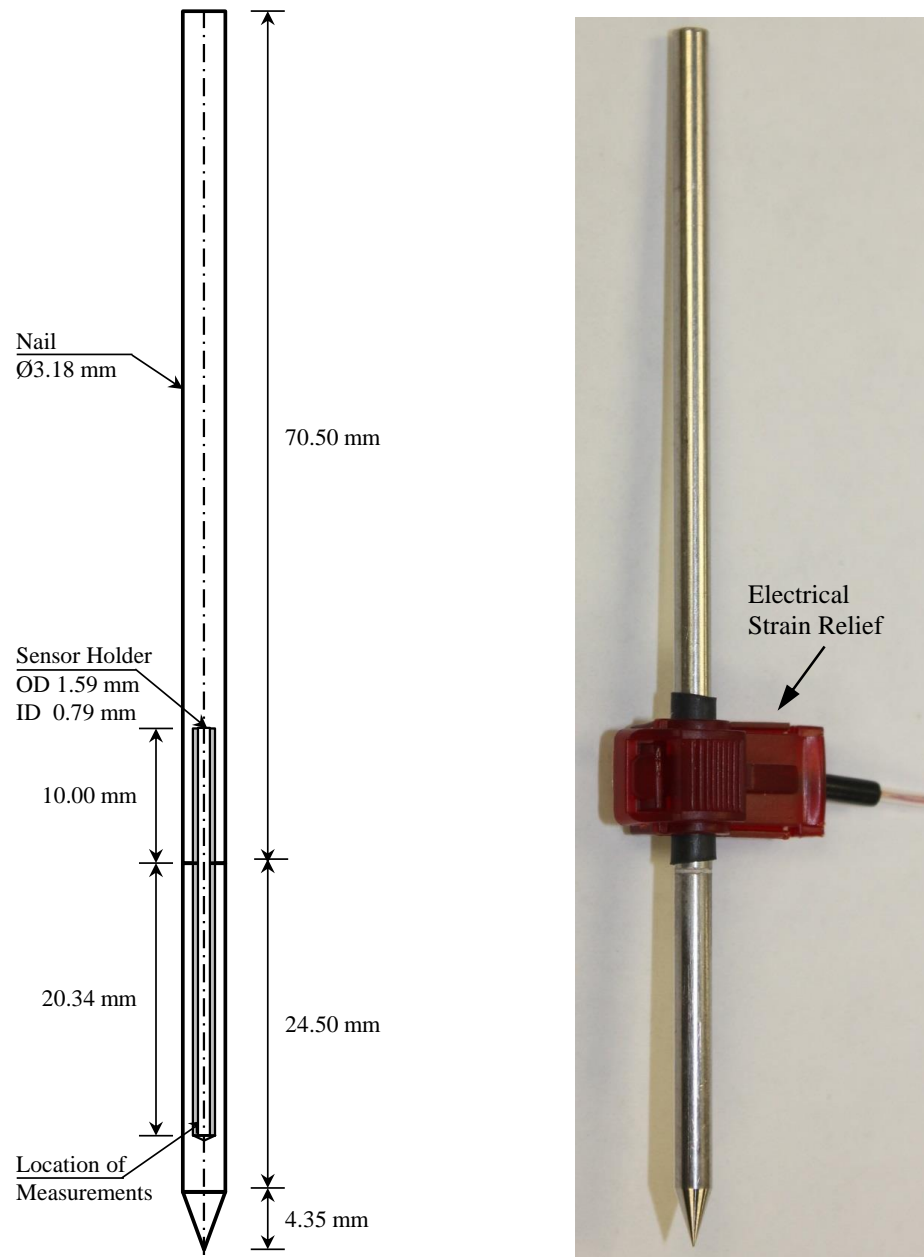


Figure 3-1 A diagram of a new design nail (left) and a new diagnostic nail (right)

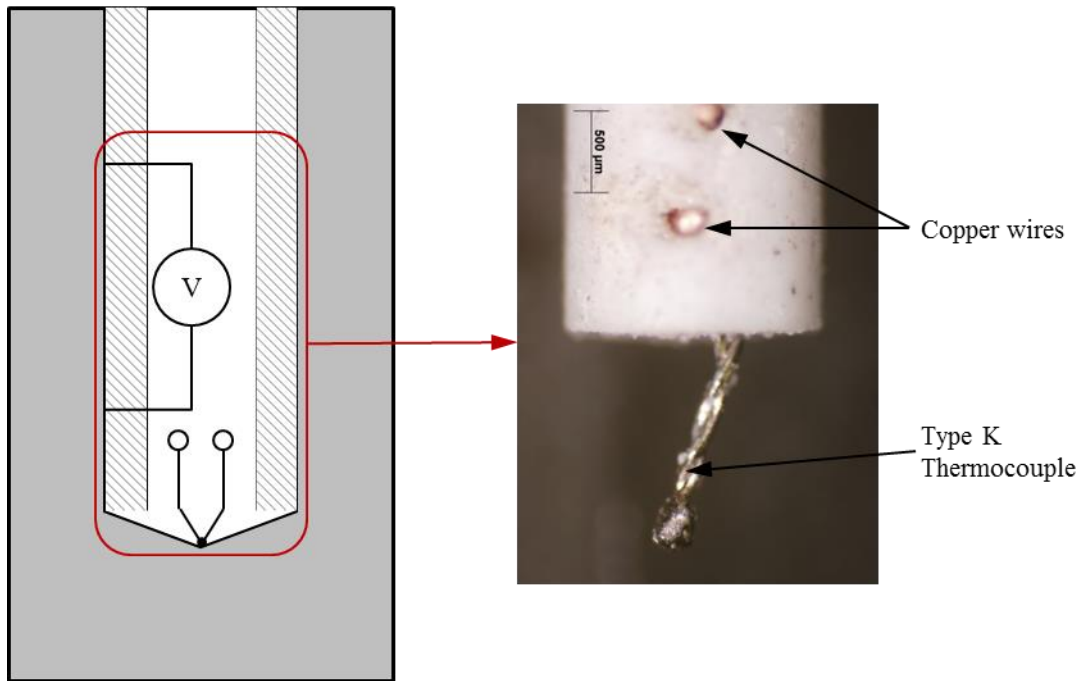


Figure 3-2 A cross section diagram at the location of measurements for a new nail design (left) and a ceramic sensor holder (right)

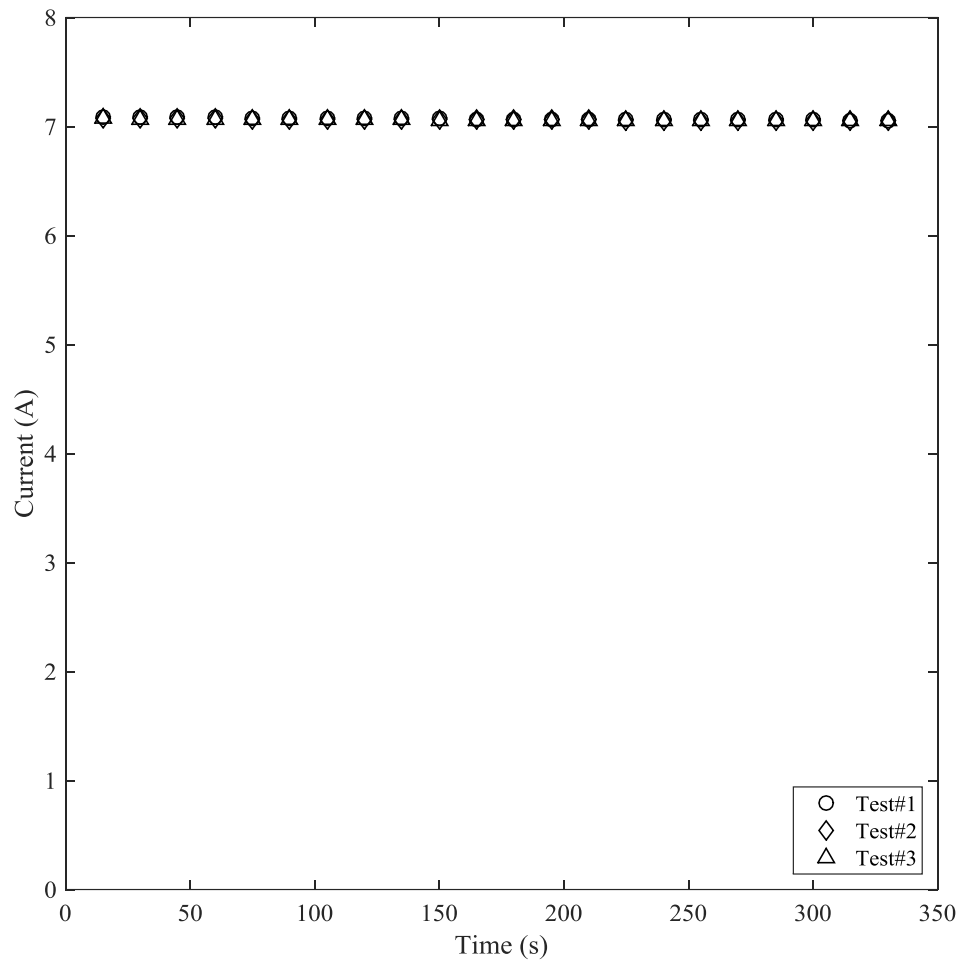


Figure 3-3 Current flow through the nail for the nail resistance measurements

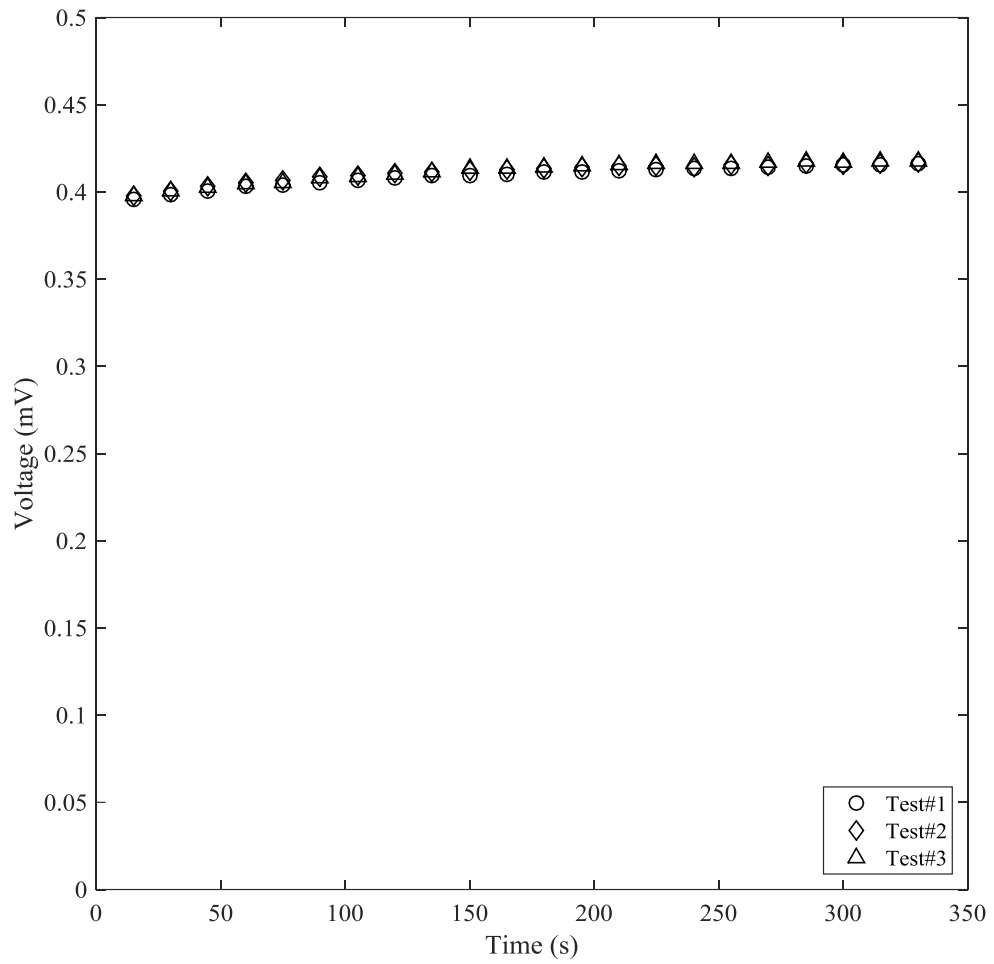


Figure 3-4 Voltage drop between the inner probes for the nail resistance measurements

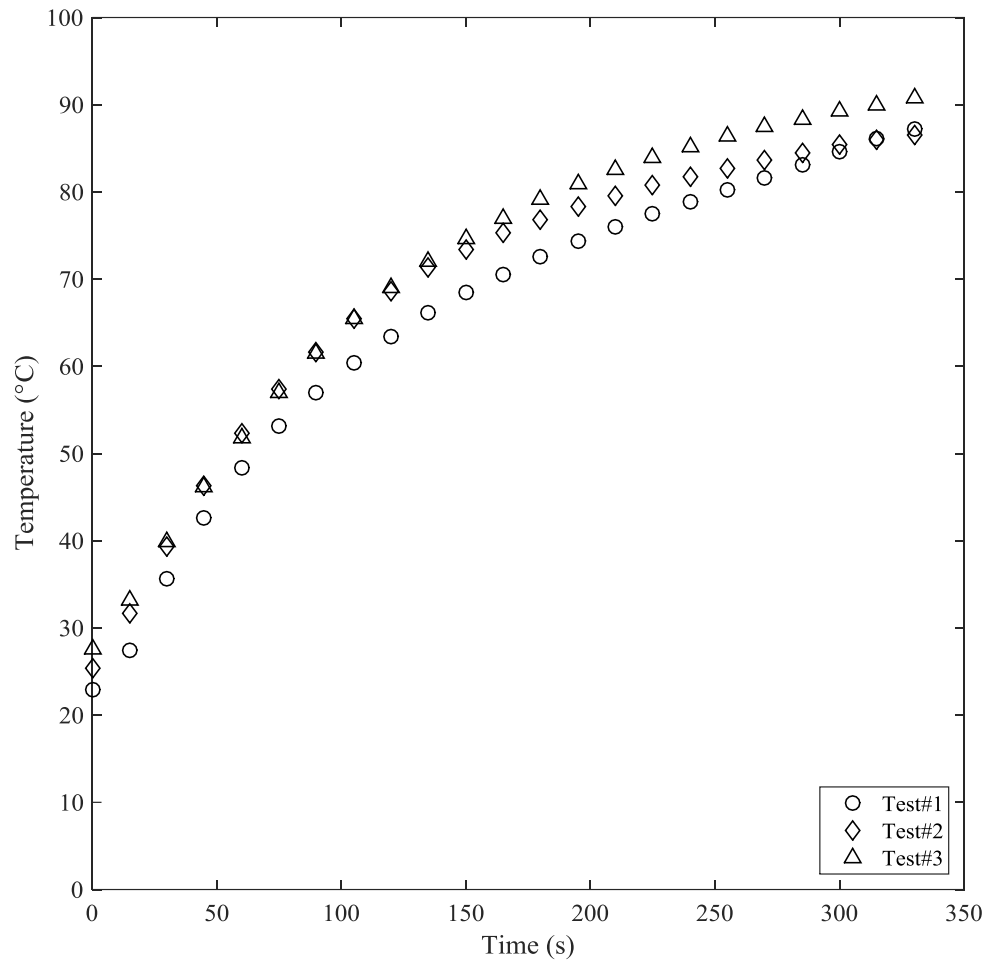


Figure 3-5 Nail center temperatures during the nail resistance measurements

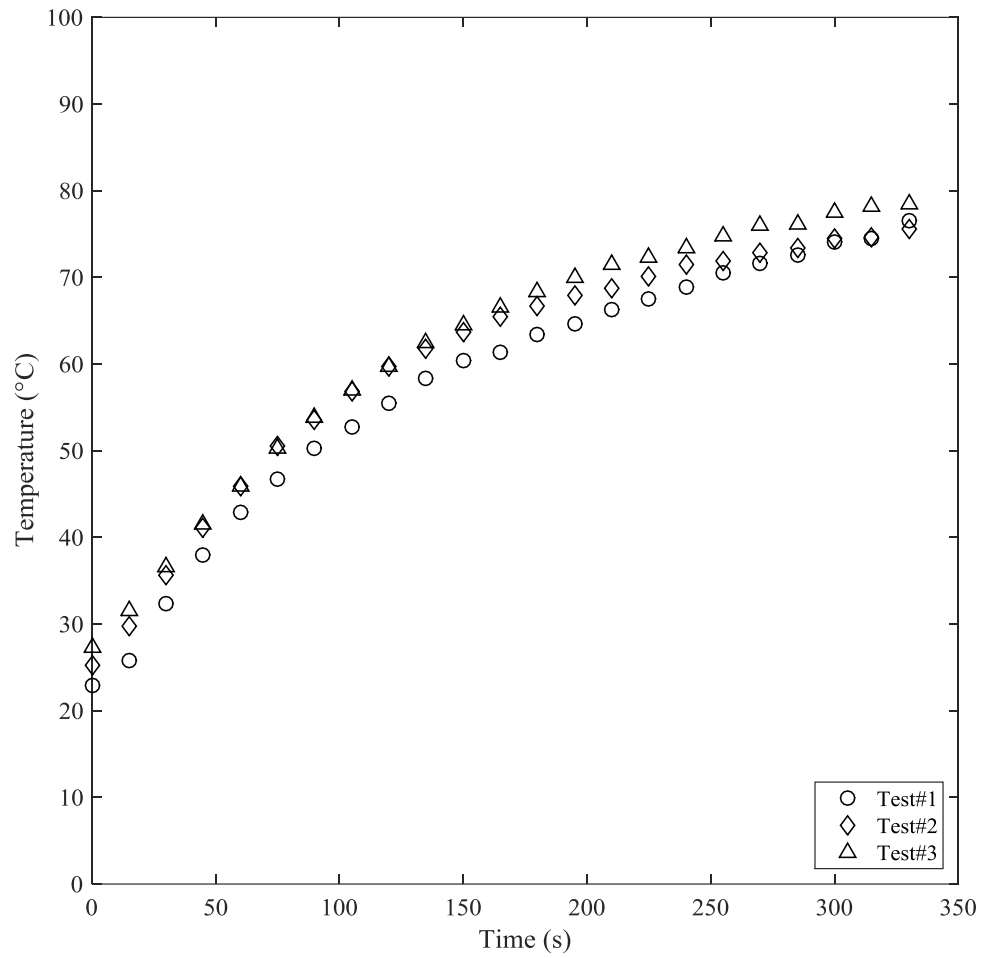


Figure 3-6 Nail surface temperatures during the nail resistance measurements

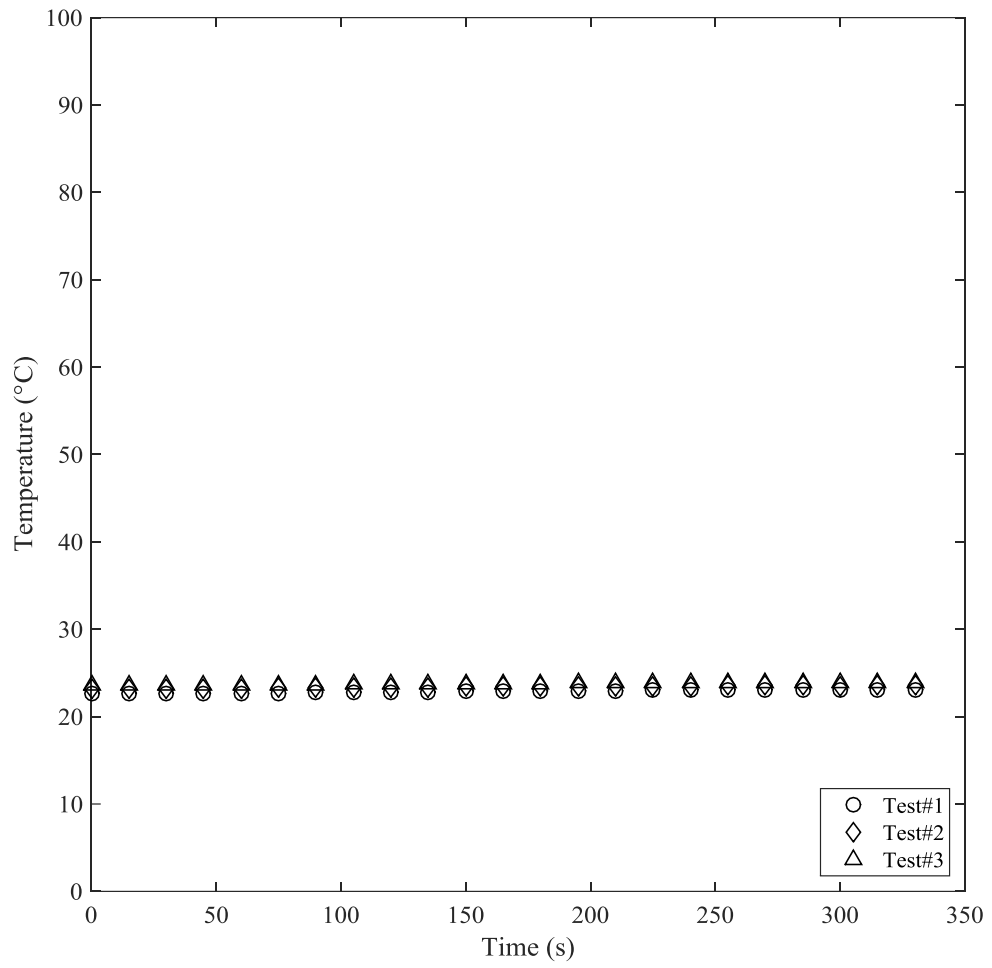


Figure 3-7 Ambient temperatures during the nail resistance measurements

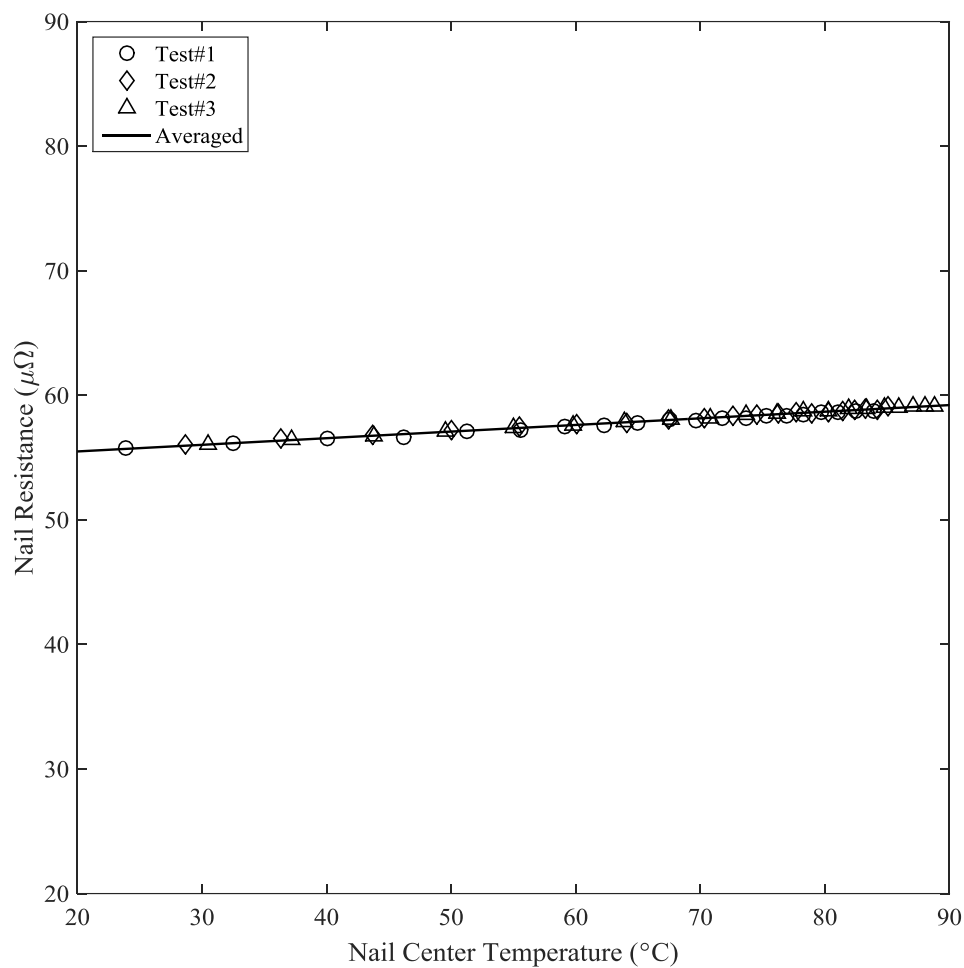


Figure 3-8 Nail resistance between the inner probes as a function of nail center temperatures

Table 3-1 Nail resistance at 20 °C and temperature coefficients of resistivity for Nail #3 using least square linear fit curves

Test #	$R_0(\mu\Omega)$	$\beta(^{\circ}\text{C}^{-1})$
1	55.41	$0.955 \times 10^{-3}$
2	55.64	$0.920 \times 10^{-3}$
3	55.51	$0.966 \times 10^{-3}$
Average	55.49	$0.959 \times 10^{-3}$

### 3.2. Experimental

For the nail penetration test#3, a pouch cell ( $\text{LiNi}_{1/3}\text{Mn}_{1/3}\text{Co}_{1/3}\text{O}_2$ ) with its capacity of 2.94 Ah is used for this experimental investigation. The cell is charged with a CC-CV protocol at room temperature and rested for 2 hour before performing a nail penetration test. For temperature measurements, cell surface temperatures, nail temperatures and ambient temperature are recorded every 0.3 s using Agilent 34970A. For electrical measurements, the cell voltage and the voltage drops between the inner probes are recorded every 0.1 s using Measurement Computing USB-2408 DAQ Module. GoPro Hero3 HD Video Camera is used to capture physical cell behaviors during the penetration. A frame rate of the video camera is 120 frame/s. Figure 3-9 shows an experimental setup in the operation chamber of the nail penetration tester. Aluminum-foil tape is used to hold on the cell tightly to the floor of the operation chamber.

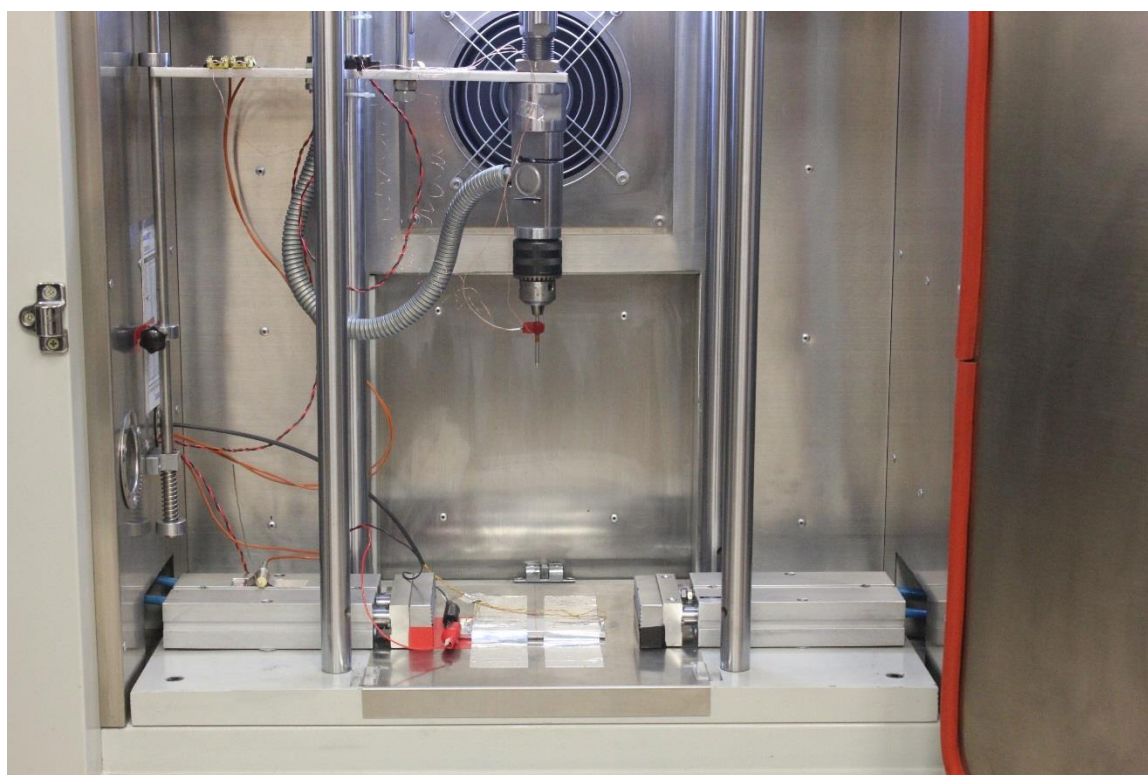


Figure 3-9 Experimental setup for the nail penetration test #3

### **3.3. Results and Discussions**

#### **3.3.1 Cell Characteristics during the Nail Penetration Test #3**

For the nail penetration test #3, the average penetration speed is 51.7 mm/s. The nail penetration depth before the penetration completed is illustrated in Figure 3-10. After the penetration completed, Figure 3-11 demonstrates a diagram of current flow path and measurements at the shorting location for Nail #3. Selected cell characteristics during the nail penetration are shown in Figure 3-12. Due to gas generation inside the cell, the high pressure pushes the cell against the force of the machine. The high pressure can be observed from the tension of the aluminum tape. The control system of the nail penetration tester maintains the position by increasing the force against the pressure. Later, some high pressure gas is released underneath the cell. Therefore, the nail was moved down from the original position by 1.8 mm.

Nail center temperatures comparison between Test #1 and Test #3 is shown in Figure 3-13. The new nail design can improve the measurements of the nail center temperatures significantly. There is no any fluctuation of temperature measurements due to noise. The similar temperature profiles of both tests implies that the wall thickness of the nail does not effect to heat generation at the shorting location. Figure 3-14 shows nail surface temperatures comparisons between Test#1 and Test#3. With the new nail design, a thermocouple can be attached on the nail surface at higher position compared to the prototype in Test #1. When the cell is swelling, the heat dissipation along the nail can be observed obviously. The time lag of temperature rise after the penetration completed is approximately 0.7 s for both tests, even though the wall thickness of Nail#3 is thinner than Nail#1.

Comparisons of cell surface temperatures between Test#1 and Test#3 are shown in Figure 3-15. All cell surface temperatures for both tests show similar profiles. This can be implied that the

experiments are repeatable. The cell surface #1 and #3 for both tests demonstrate high repeatability. For the cell surface #2 and #3, the maximum temperature differences between Test #1 and Test #3 are 11.8 °C and 16.1 °C. The temperature differences between Test #1 and Test #3 is due to non-uniform heat generation inside the cell.

Comparisons of average nail resistance during the penetration of Test #1 and Test #3 are shown in Figure 3-16. The nail resistance is estimated using Equation (2-3) and average nail resistance at 20 °C and average temperature coefficients of resistivity. For the maximum resistance of both tests, the nail resistance in Test #1 is increased by 58.5% whereas the nail resistance in Test #3 is increased by 46.2%. The difference of the resistance between these tests is due to the temperature coefficient of resistivity obtained from nail resistance measurements. The resistivity temperature coefficient of Nail #1 is higher than Nail #3 by 22%.

Cell voltage comparison between Test #1 and Test #2 is shown in Figure 3-17. Before the penetration completed, the cell voltage drops in Test #3 is lesser than in Test #1 by 0.3 V. The lower voltage drop indicates that the shorting resistance in Test #3 is higher than the shorting resistance in Test#1. After the penetration completed, the recover voltage for Test #3 is higher than the recover voltage for Test #1 by 1.68 V. The recover voltage is determined from the minimum voltage at 0.3 s to the maximum voltage after the penetration completed. Due to the higher discharge capacity of the cell used in Test #3, the cell voltage in Test#3 drops to 0.3 V later than in Test #1.

Voltage drops between the inner probes for Test #1 and Test #3 are shown in Figure 3-18. The ceramic holder reveals that the current redistribution into the inner wall is a sinusoidal waveform. The ceramic holder is an electrical insulator so electric cannot flow through the holder. However, it can be polarized by an applied electric field if it is placed between electric field. Average shorting current comparison between Test #1 and Test #2 Figure 3-19. Figure 3-20

demonstrate cumulative discharge capacity of the cell using Equation (2-5). Figure 3-21 shows the cumulative discharge capacity as a function of the cell voltage.

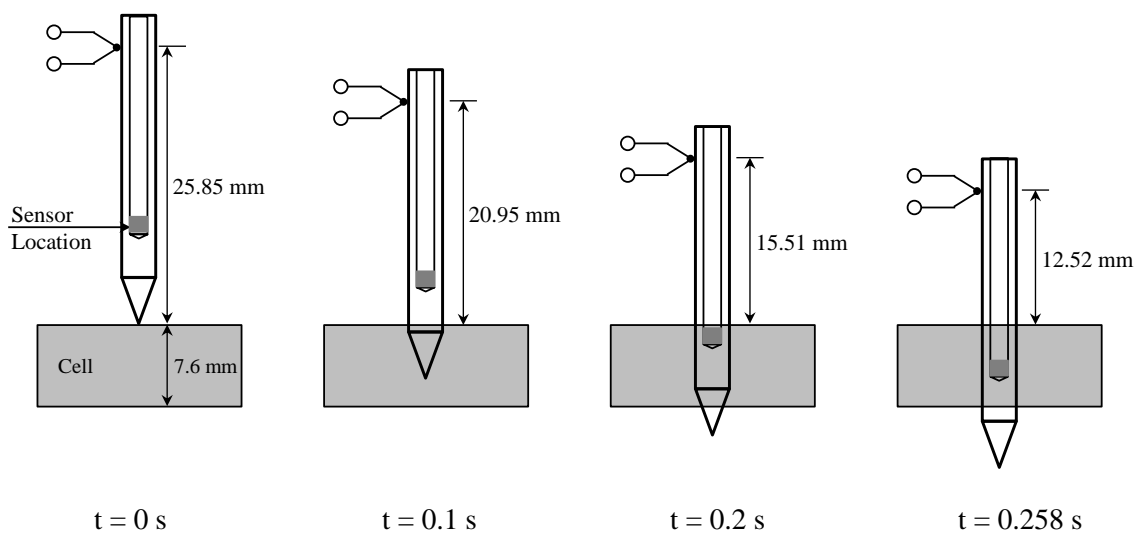


Figure 3-10 Penetration depth of Test #3 before the penetration completed

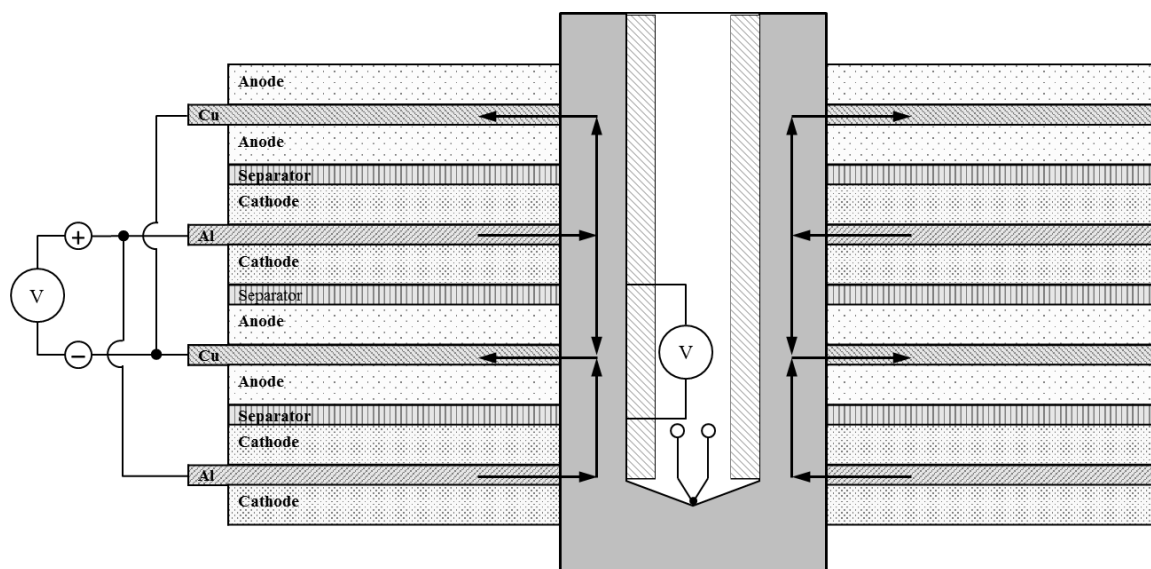
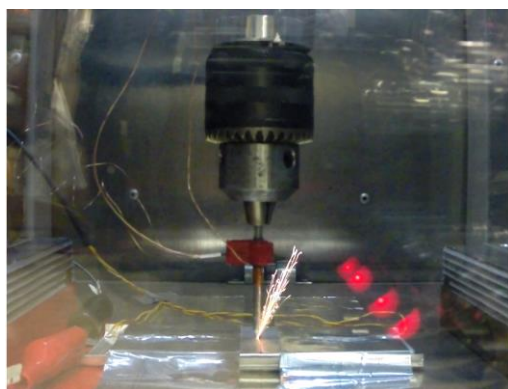
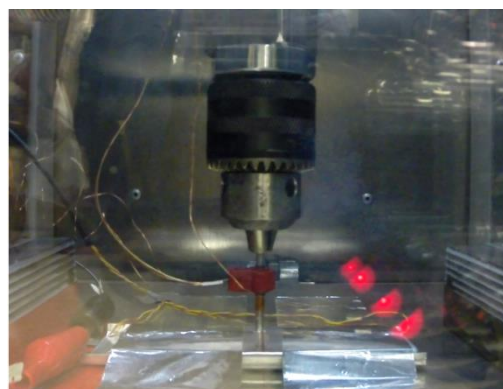


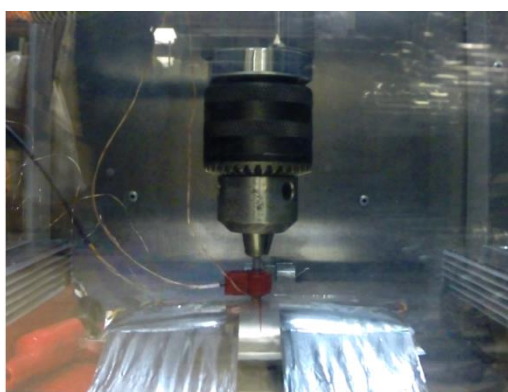
Figure 3-11 Diagram of current flow path and measurements at the shorting location for Nail #3



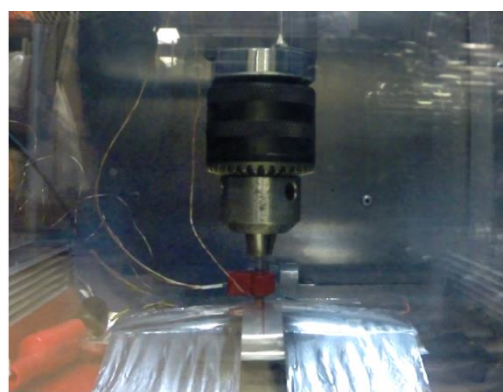
Time = 0.033 s  
Sparks



Time = 0.258 s  
Penetration Completed



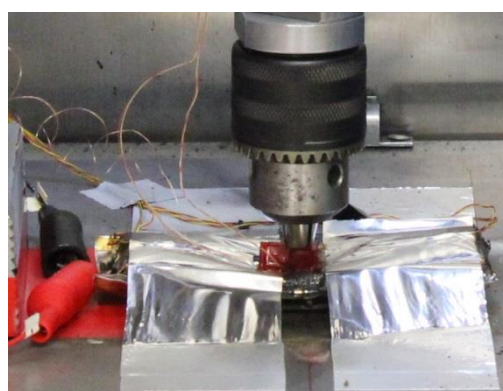
Time = 1.350 s  
Maximum cell volume expansion



Time = 1.375 s – 1.433 s  
The chuck moved down by 1.8 mm



Time = 3.025 s  
Smoking and Fire



The cell after the test was finished

Figure 3-12 Cell characteristics of the nail penetration #3

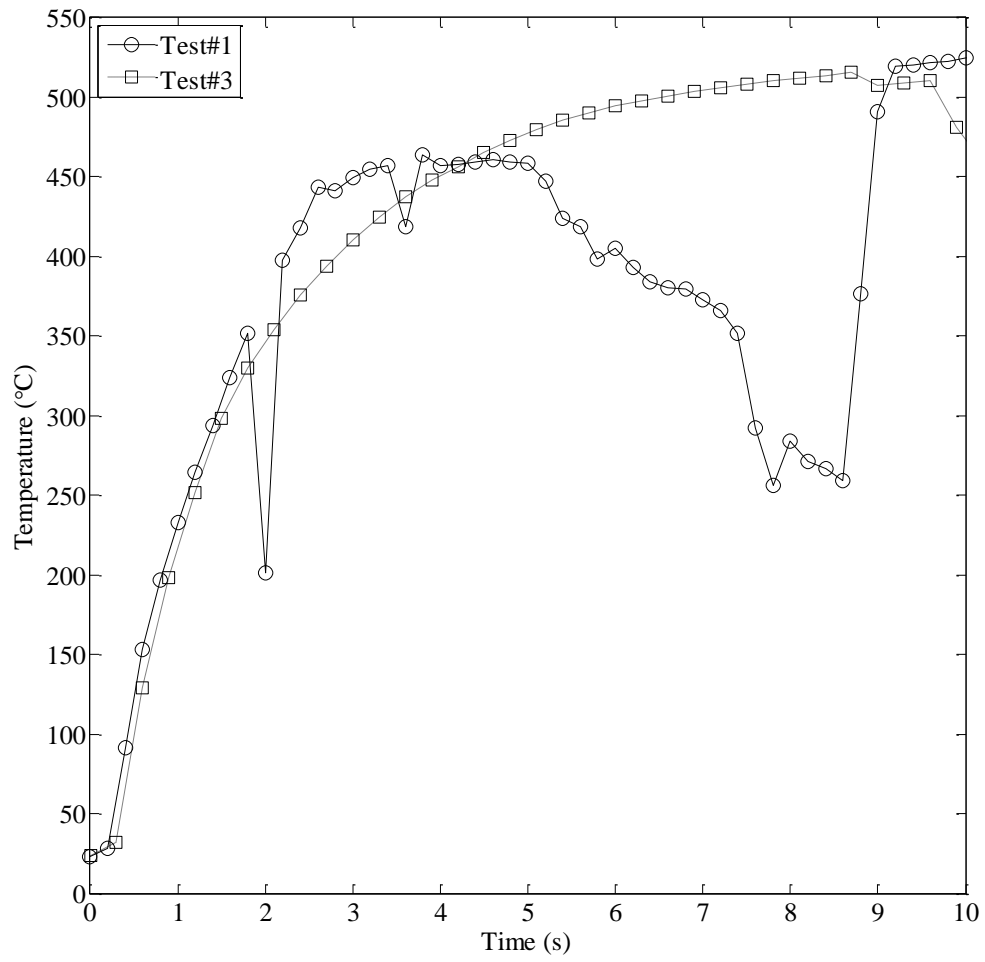


Figure 3-13 Nail center temperatures comparison between Test#1 and Test#3

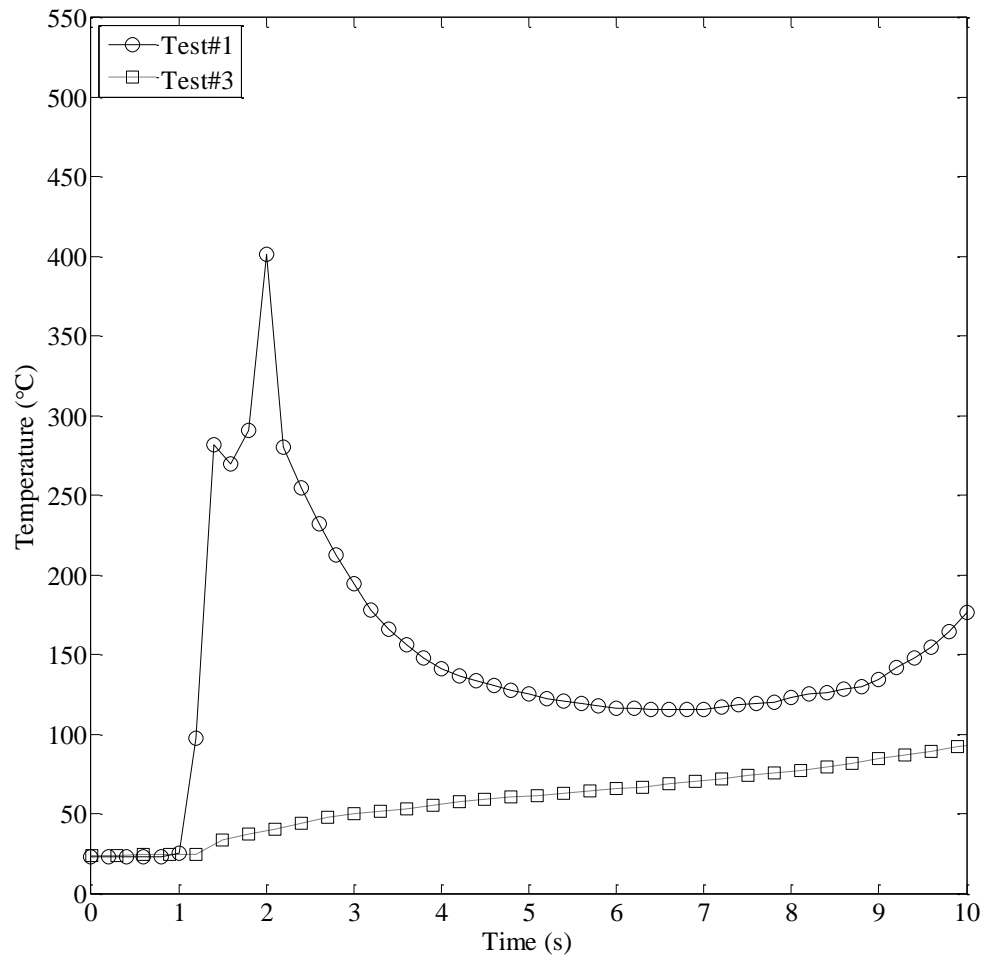


Figure 3-14 Nail surface temperatures comparison between Test#1 and Test#3

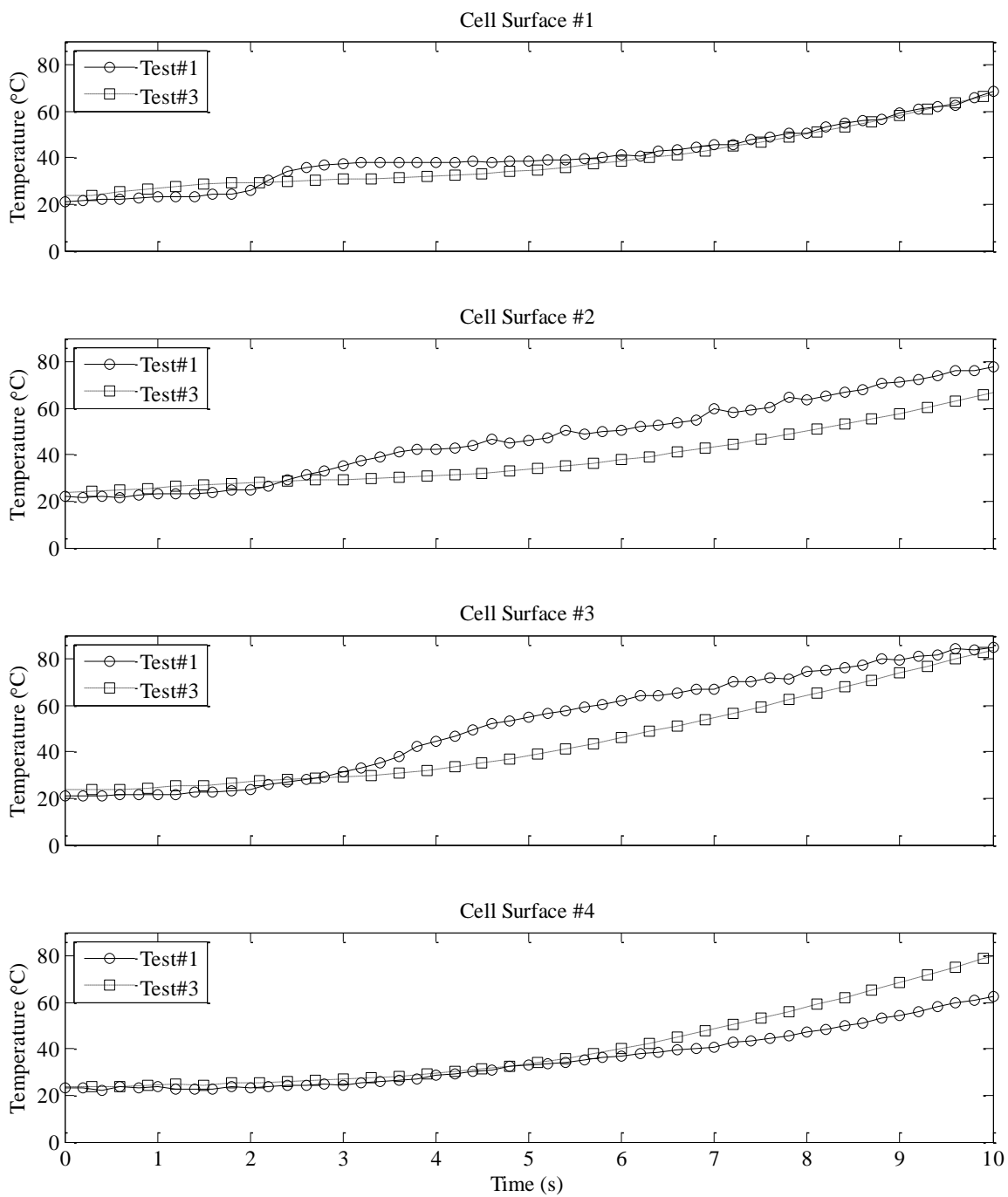


Figure 3-15 Comparisons of cell surface temperatures between Test#1 and Test#3

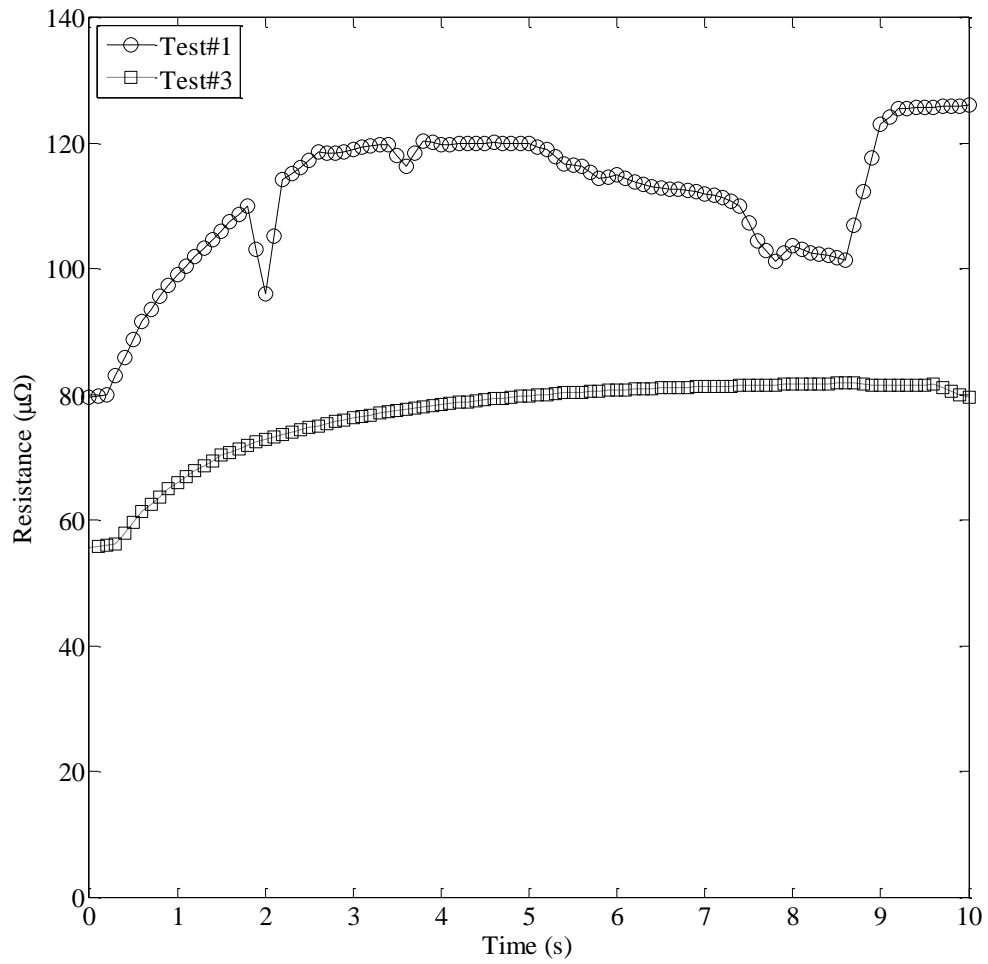


Figure 3-16 Comparisons of average nail resistance during the penetration of Test #1 and Test #3

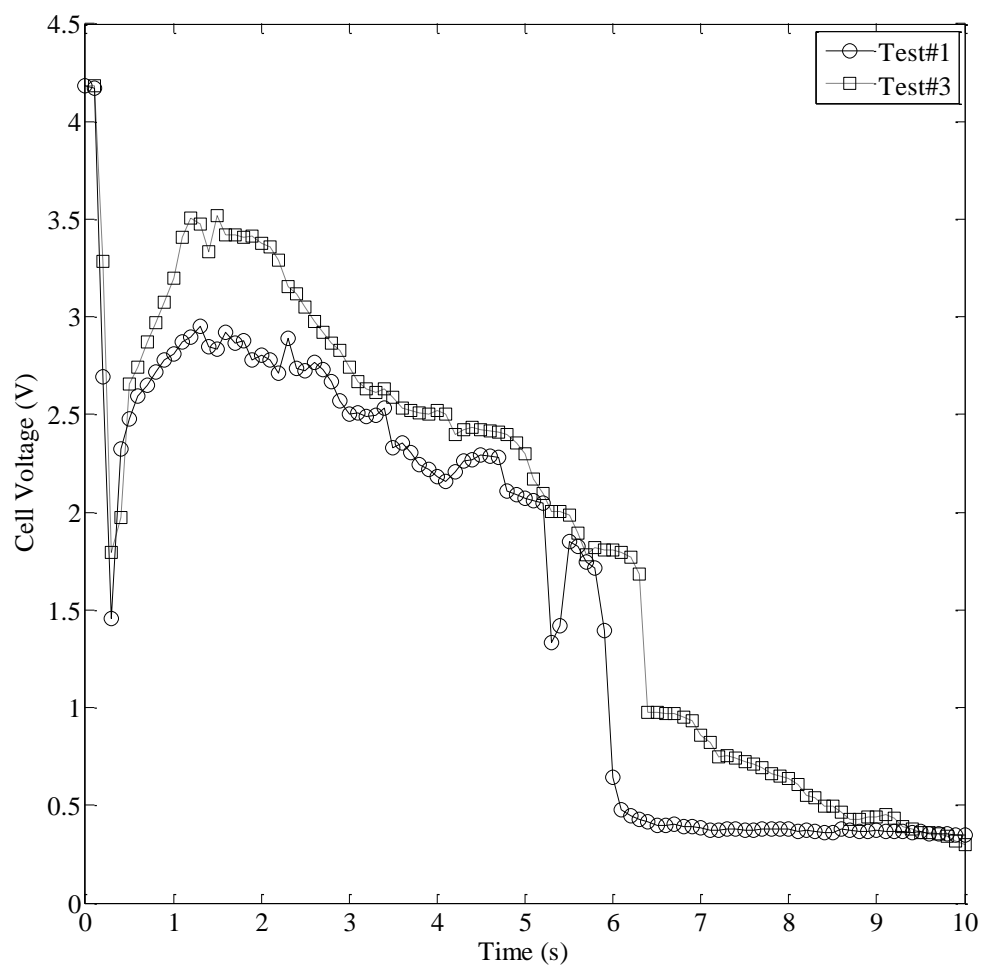


Figure 3-17 Cell voltage comparison between Test #1 and Test #3

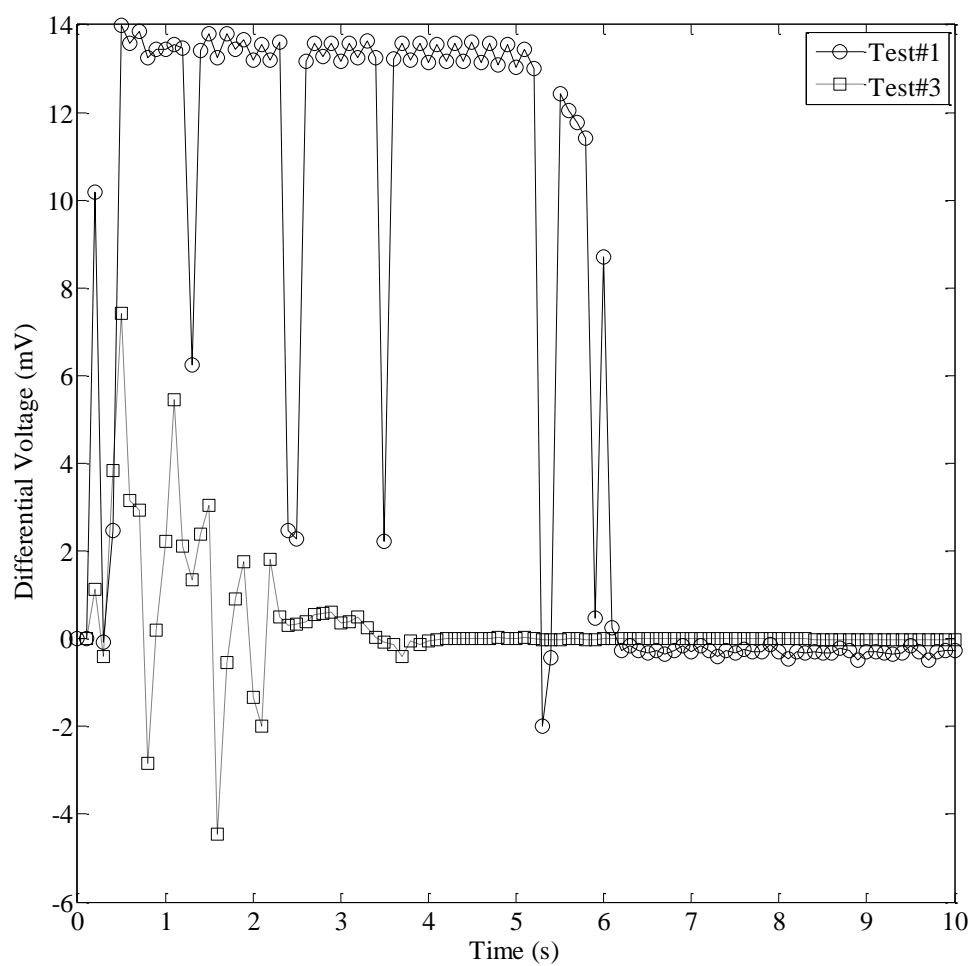


Figure 3-18 Voltage drops between the inner probes for Test #1 and Test #3

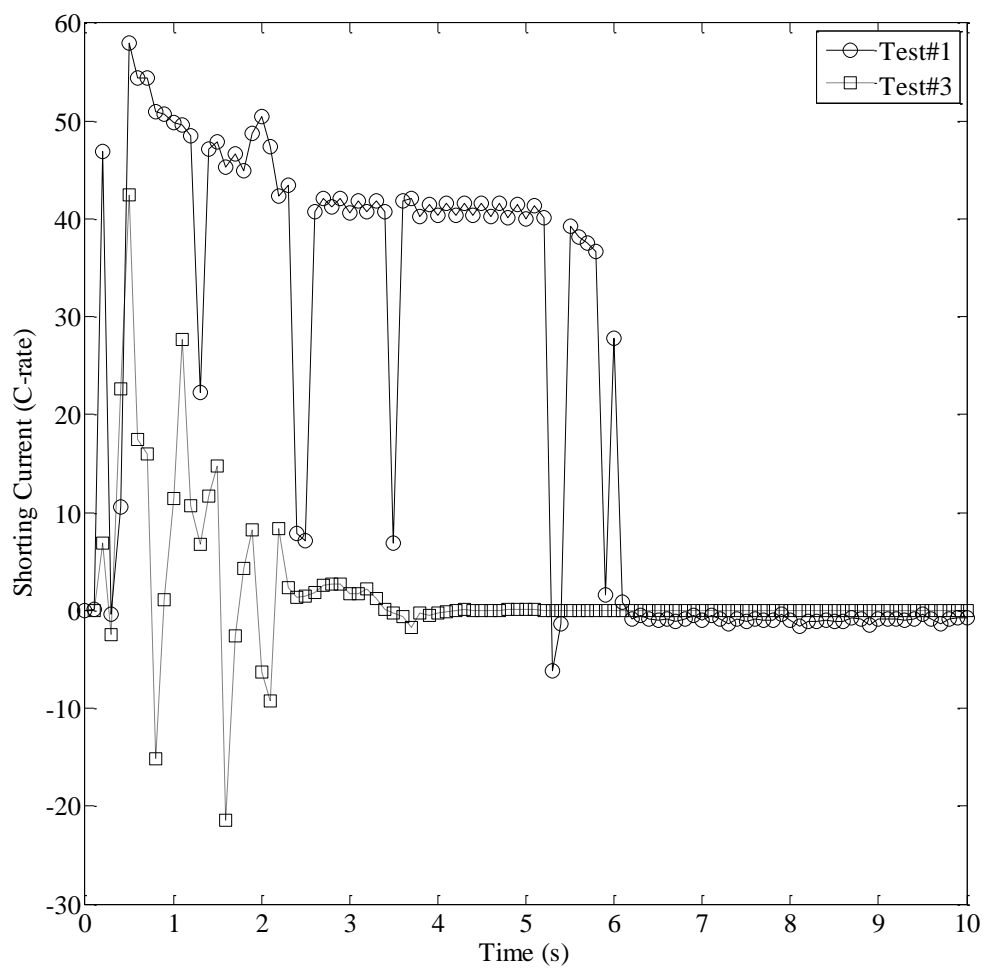


Figure 3-19 Average shorting current comparison between Test #1 and Test #3

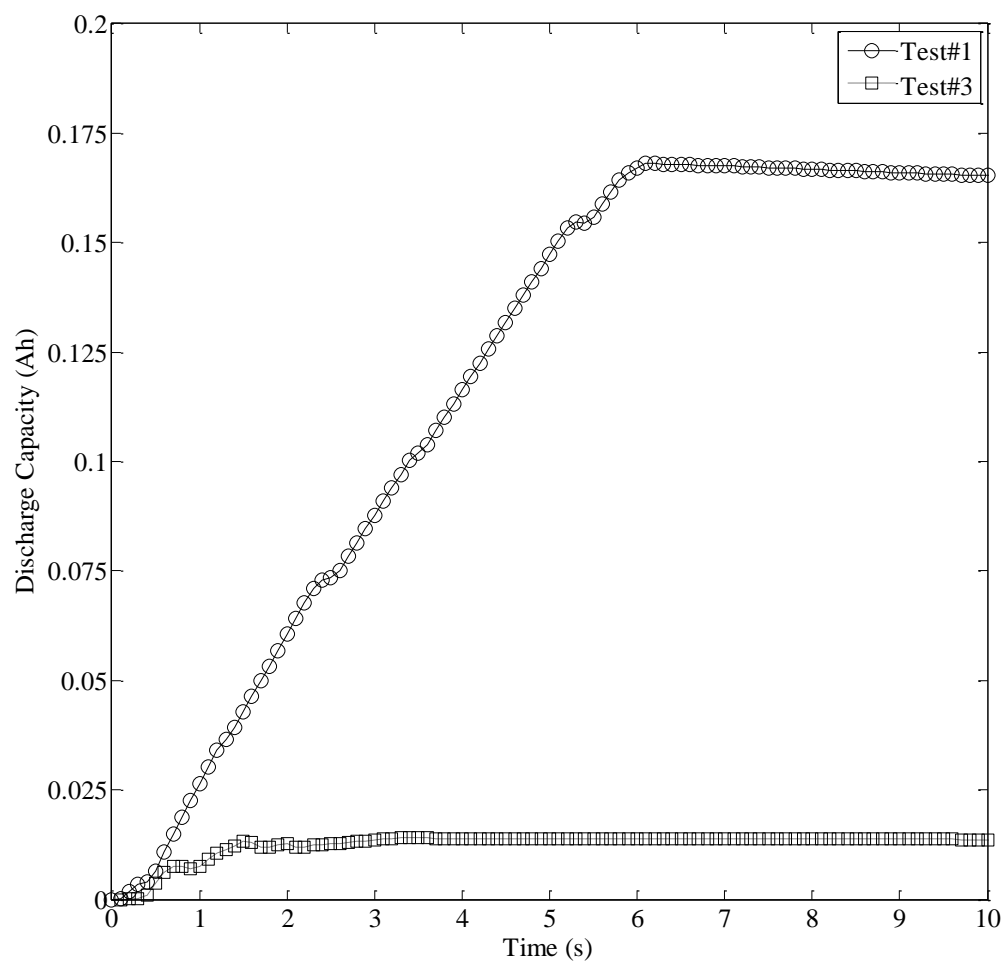


Figure 3-20 Discharge capacity as a function of time for Test #1 and Test #3

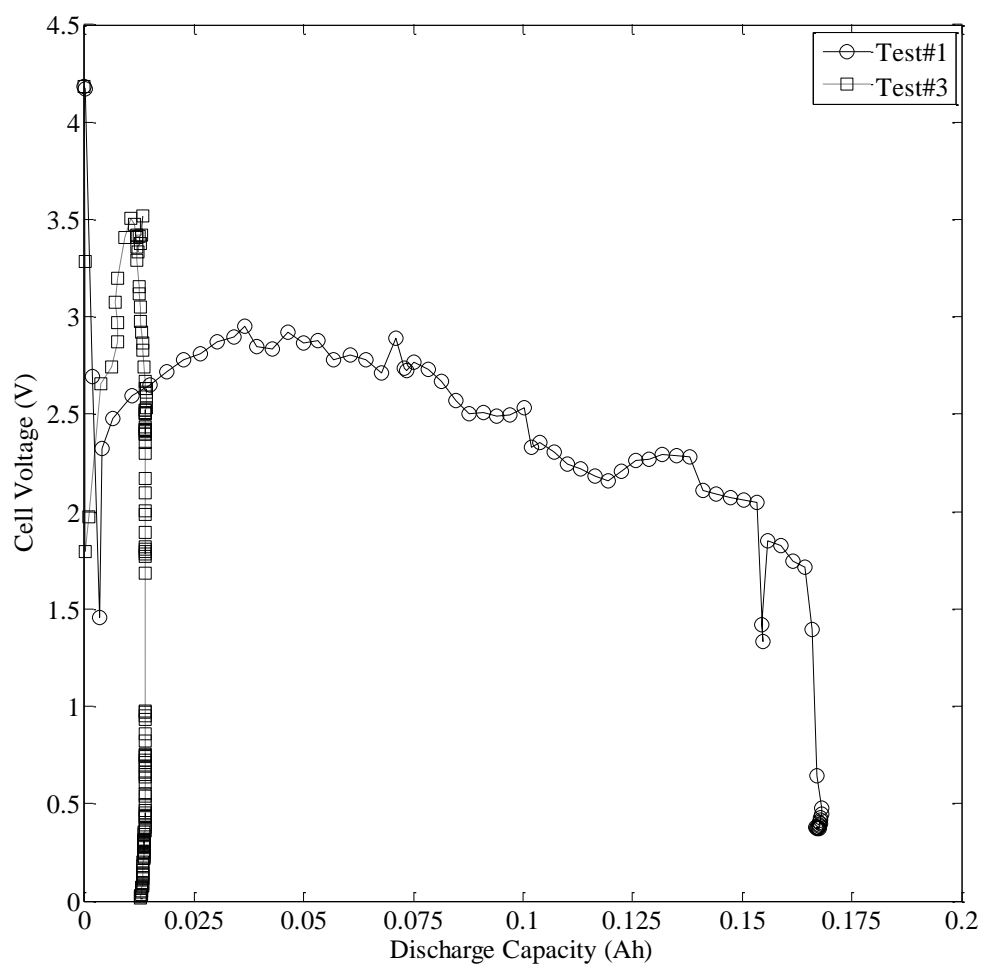


Figure 3-21 Cell voltage as a function of discharge capacity for Test #1 and Test #3

### 3.3.2 Energy Balance of the Diagnostic Nails at the Shorting Area

Control volumes of the diagnostic nails used in Test #1 and Test #3 are illustrated in Figure 3-22. Energy balance of a control volume can be expressed shown in Equation (3-2) where  $\dot{E}_{Acc}$  is a rate of accumulative heat in the control volume,  $\dot{E}_{In}$  is a rate of energy entering the control volume,  $\dot{E}_{Out}$  is a rate of energy leaving the control volume and  $\dot{E}_{Gen}$  is a rate of thermal energy generation due to Ohmic heat.

$$\dot{E}_{Acc} = \dot{E}_{In} - \dot{E}_{Out} + \dot{E}_{Gen} \quad (3-1)$$

$\dot{E}_{Acc}$  can be determined using Equation (3-2) where  $\rho_{ss}$  is the density of 304 stainless steel,  $A_c$  is a cross section area of the metal,  $L$  is the length of the cell thickness,  $c_p$  is a specific heat at constant pressure,  $T$  is nail center temperature and  $t$  is time. Constant properties are applied to the control volumes. Table 3-2 lists material properties of a nail.

$$\dot{E}_{Acc} = \rho_{ss} A_c L c_p \frac{dT}{dt} \quad (3-2)$$

$\dot{E}_{Gen}$  can be estimated using Equation (3-3) where  $I$  is the current flow through the nail and  $R_{Nail}$  is the nail resistance of the control volume.

$$\dot{E}_{Gen} = I^2 R_{Nail,L} \quad (3-3)$$

$R_{Nail,L}$  can be estimated using Equation (3-4) where  $\sigma_0$  is the electrical conductivity of 304 stainless steel at 20 °C,  $\beta$  is the average temperature coefficients of resistivity obtained from nail resistance measurements and  $T_0$  is the reference temperature.

$$R_{Nail,L} = \frac{L}{A_c \sigma_0} [1 + \beta(T - T_0)] \quad (3-4)$$

$\dot{E}_{In}$  and  $\dot{E}_{Out}$  are rate of energy transport across control surfaces of the nail by three basic mechanisms. The first mechanism is heat conduction through the actual contact spots. The second mechanism is heat conduction through the interstitial medium convection such as air and electrolyte. The third mechanism is the radiation across the gaps. During a nail penetration test, complicated phenomena occur inside the cell and especially at the interface between the nail and the electrodes. Moreover, internal temperatures of the cell near the shorting location are very challenging to measure. Therefore, only the accumulative heat and Ohmic heat are estimated for this present work.

Figure 3-23 shows the accumulative heat comparison for Test #1 and Test #3. For both tests, the rate of the accumulative heat is increased rapidly after nail penetration completed due to high inrush current. Later, the rate of the accumulative heat decreases because heat dissipation along the nail causing the nail surface temperature increase. Both profiles show good agreement in the increasing rate and decreasing rate. Notice that the high fluctuation in Test #1 is due to noise from temperature measurements. Figure 3-24 show Ohmic heat comparison for Test #1 and Test #3. Due to the current measurements, considerable difference in heat generation between Test #1 and Test #3 can be expected. The Ohmic heat is less than the accumulative heat for both tests. This can be implied that that heat entering to the nail is much greater than the combination of Ohmic heat and heat losses.

To estimate the accumulative energy and thermal energy generation of the nail, the trapezoidal numerical integration is used to integrate Equation (3-2) and Equation (3-3). Figure 3-25 and Figure 3-26 demonstrate the accumulative energy and thermal energy generation of the nail used in Test #1 and Test #3. Due to the mass of Nail #1 is higher than Nail #3, the accumulative heat in Test #1 is higher than the accumulative heat in Test #3. The accumulative heat is approximately 2 times of Ohmic heat for Test #1, whereas 16 times of Ohmic heat in Test #3.

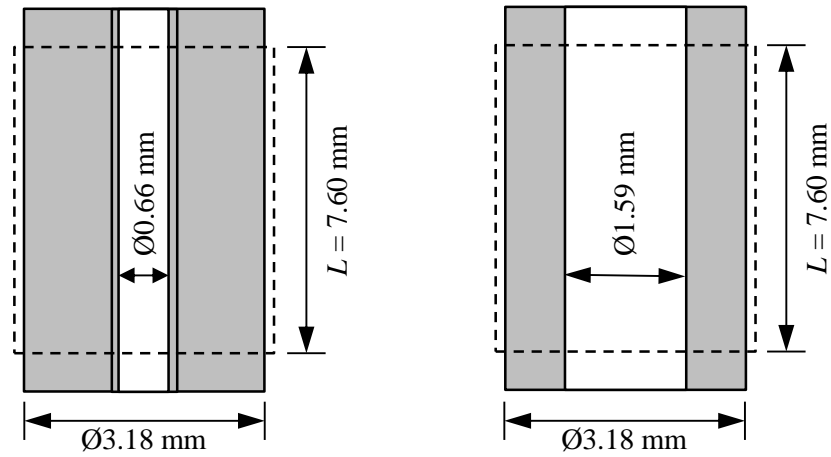


Figure 3-22 Control volumes of the diagnostic nails used in Test #1 (left) and Test #3 (right)

Table 3-2 Material properties of a nail

Properties	Unit	Value
Density	$\text{kg m}^{-3}$	7900
Specific heat	$\text{J kg}^{-1}\cdot\text{K}^{-1}$	477
Electrical conductivity	$\text{S cm}^{-1}$	$1.39 \times 10^6$
Reference temperature	$^{\circ}\text{C}$	20

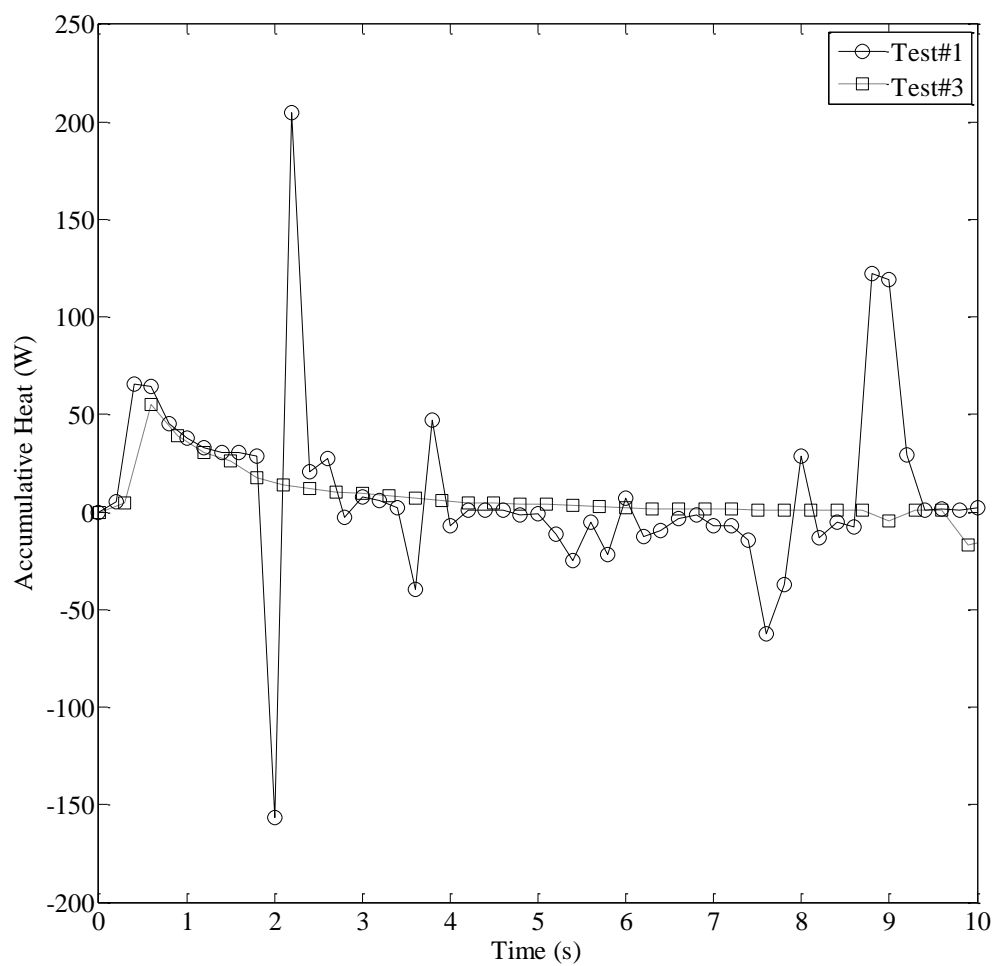


Figure 3-23 Accumulative heat comparison for Test #1 and Test #3

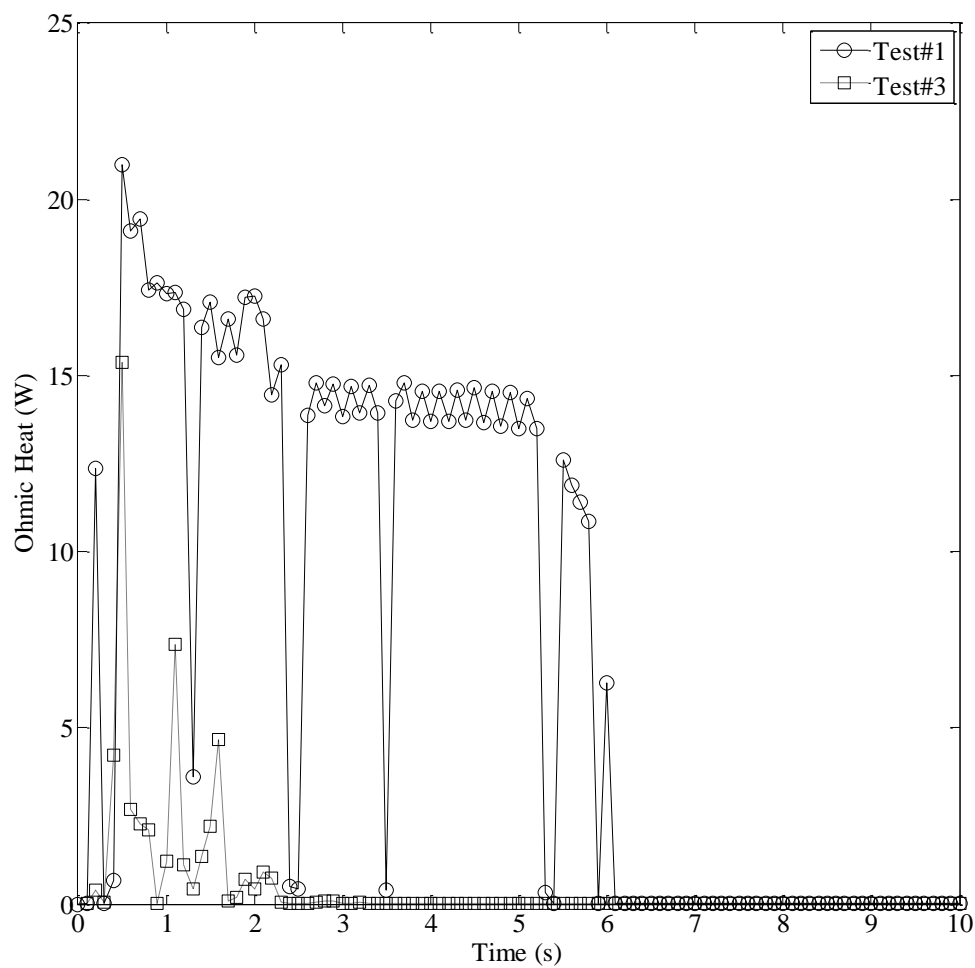


Figure 3-24 Ohmic heat comparison for Test #1 and Test #3

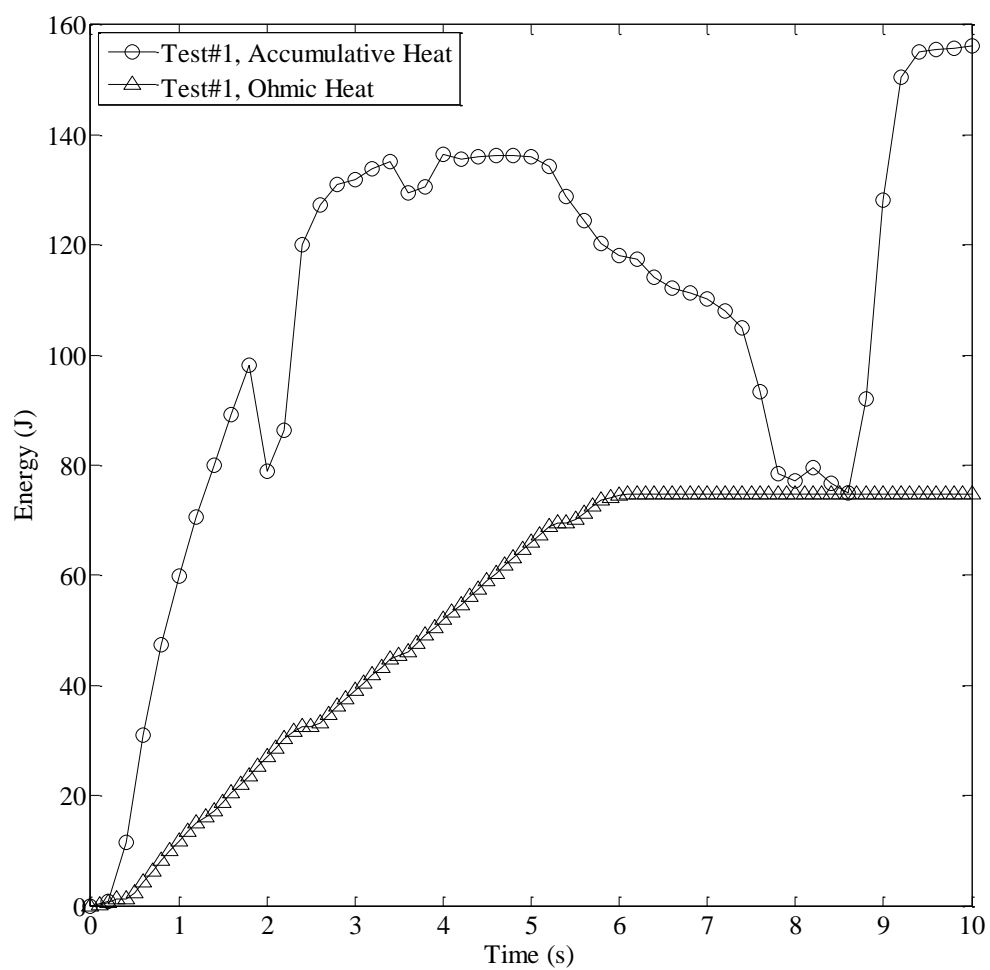


Figure 3-25 Accumulative energy and thermal energy generation of the nail used in Test #1

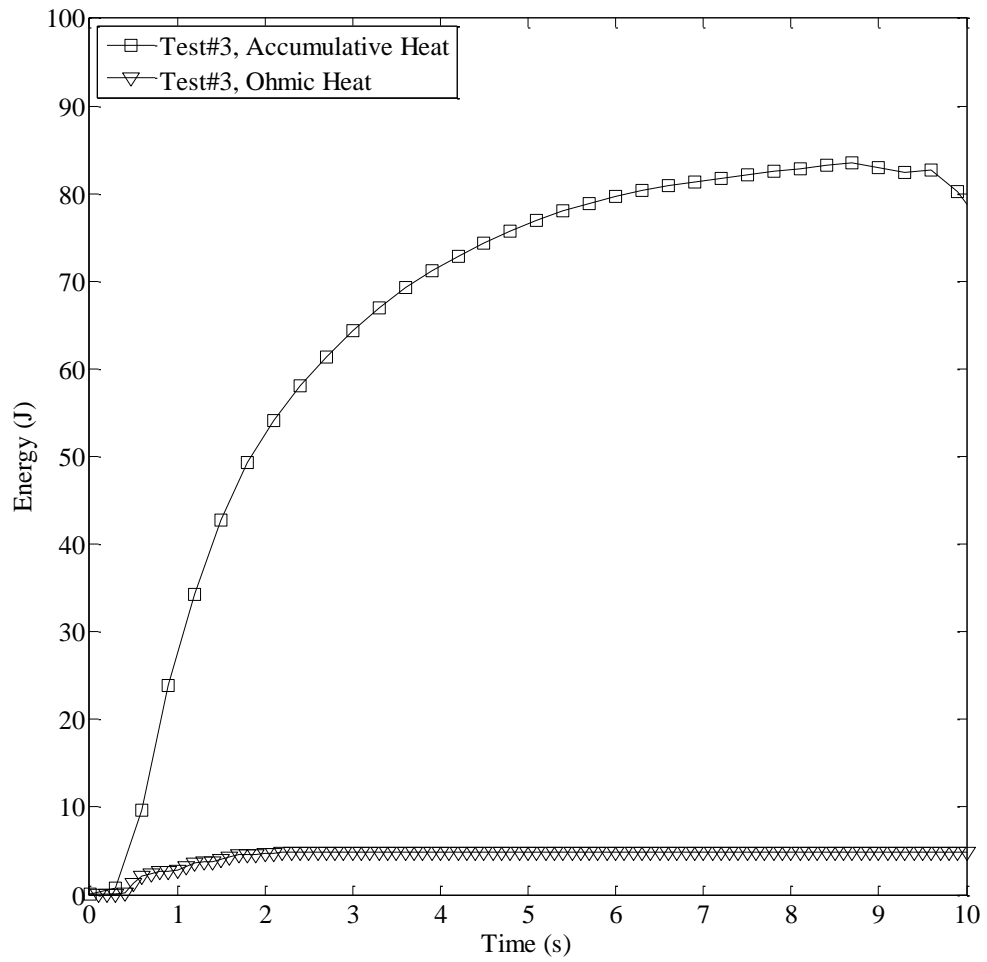


Figure 3-26 Accumulative energy and thermal energy generation of the nail used in Test #3

### **3.4. Summary**

A diagnostic nail with a composite wall is developed for investigating effects of nail composite wall on cell characteristics during a nail penetration test. With improvements in the new design, nail temperature measurements can be improved significantly. Comparisons of experimental results between Test#1 and Test #3 demonstrate that the wall structure does not only effect the cell characteristics but also the rate of heat conduction and heat generation along the nail. The nail made with a composite wall reveals current flows from the nail surface into the inner with a sinusoidal waveform.

## Chapter 4

### Conclusions and Future Work

#### 4.1. Conclusions

Diagnostic nails have been developed to obtain nail temperatures and shorting current flow through the nail during nail penetration tests. With new experimental data, the fundamental electrochemical and thermal behaviors of Lithium-ion batteries during internal short circuits have been elucidated. Chapter 1 presents literature reviews of prior experimental studies on nail penetration tests, as well as modeling and simulation studies for internal short circuits.

Chapter 2 presents in situ measurements of internal short circuits during nail penetration using diagnostic nails. To obtain repeatable results, the shorting resistance at the initial stage is needed to be controllable. The average shorting current for both tests is approximately 40 C-rate. The fluctuation of the shorting current is due to random sparks and fire caused loose contacts between the nail and cell the components. The reproducibility of nail penetration tests is still very challenging.

Chapter 3 presents effects of nail composite wall on cell characteristics during nail penetration tests. A new composite wall structure of a diagnostic nail is introduced. The new diagnostic nail is installed with a ceramic sensor holder to improve operating temperatures of the sensors. A nail penetration test is conducted using the new nail design. Comparisons of experimental results between Test#1 and Test #3 show that the composite wall structure does not affect to the cell characteristics during the nail penetration test but it affects to the current redistribution inside the nail.

## **4.2. Future Work**

Much work is needed to develop comprehension of electrochemical and thermal transport processes, as well as failure mechanisms during internal short circuits by a nail penetration. Further experimental studies can be investigated to elucidate the fundamentals and failure mechanisms as following.

### **4.2.1 Parametric Study of Nail Structure Design**

A diagnostic nail enables investigations on electrochemical and thermal behaviors of Lithium-ion batteries during a nail penetration. Further development on the nail structure is needed to elucidate the fundamentals and mechanisms during a nail penetration test. To study current distribution inside the nail, number of copper wires and distance between the wires are needed to be studied. Furthermore, effects of nail diameter to cell behaviors during nail penetrations are also an important study. The nail diameter effects to the shorting resistance, the shorting area and heat dissipation along the nail.

### **4.2.2 Effects of Nail Thermal Conductivity on Cell Characteristics during a Nail Penetration Test**

Thermal conductivity is an important transport property of materials indicating the rate of thermal energy transfer by the diffusion process. Based on Fourier's law, the conduction heat flux can be increased by increasing thermal conductivity. For modeling nail penetration processes, Zhao et al. [37] shows that the nail thermal conductivity plays a critical role on cell thermal characteristics during the penetration. With higher nail thermal conductivity, the peak temperature of the nail is decreased significantly.

Based on FreedomCAR Electrical Energy Storage System Abuse Test Manual for Electric and Hybrid Electric Vehicle Applications [38], the description of penetration tests in the manual indicates that a mild steel pointed rod is used for a penetration test. For a general definition, mild steel is low-carbon steel containing Carbon from 0% to 0.3%. The low carbon steels are widely in automotive applications used because their formability and weld ability. Comparison of material properties between 304 stainless steel and 1018 mild steel is listed in Table 4-1. The thermal conductivity of 1018 mild steel is higher than the thermal conductivity of 304 stainless steel by 220%. Moreover, the electrical resistivity of 1018 mild steel is lower than the thermal conductivity of 304 stainless steel by 69%. Significant changes in cell characteristics during a nail penetration can be expected.

#### **4.2.3 Experimental Investigation on Electrical and Thermal Contact Resistance in Nail Penetrations**

Electrical Contact Resistance (ECR) is a resistance to a flow of electricity generated by a joint between two elements. For a nail penetration test, poor mechanical connections between electrodes and the nail create internal short circuits, as well as establish the ECR at the interface. As the current flows from a cathode electrode to an anode electrode, heat generation due to the ECR can be higher than heat generation due to the electrochemical reaction. The heat transfer through the gaps can play an important role in heat dissipation during nail penetrations. Therefore, the thermal contact resistance is crucial to study.

Table 4-1 Material properties of 304 stainless steel and 1018 mild steel [39]

Materials Property	Unit	304 Stainless Steel	1018 Mild Steel
Yield strength	MPa	207	414
Electrical resistivity	$\mu\Omega\text{-cm}$	72 (20°C) 116 (650°C)	15.9 (0°C) 21.9 (100°C) 29.3 (200°C)
Thermal conductivity	W/m-K	16.2 (0-100°C)	51.9
Specific heat capacity	J/kg-°C	500 (100°C)	486 ( $\geq 100^\circ\text{C}$ )
Density	kg/m <sup>3</sup>	8000	7870
Thermal diffusivity	m <sup>2</sup> /s	$4.05 \times 10^{-6}$	$13.57 \times 10^{-6}$
Coefficient of thermal expansion	$\mu\text{m/m-}^\circ\text{C}$	17.3 (20°C) 17.8 (315°C) 18.4 (538°C)	n/a

## References

- [1] U.S. Department of Energy, “Alternative Fuels Data Center: Maps and Data.” [Online]. Available: <http://www.afdc.energy.gov/data/>.
- [2] B. Smith, “Chevrolet Volt Battery Incident Summary Report,” Washington, DC, 2012.
- [3] B. Klayman and B. Woodall, “UPDATE 5-Tesla reports third fire involving Model S electric car,” *Reuters*, 2013. [Online]. Available: <http://www.reuters.com/article/2013/11/07/autos-tesla-fire-idUSL2N0IS0TL20131107?type=companyNews>.
- [4] T. Moloughney, “Another Model S fire,” *Tesla Motors Club*, 2013. [Online]. Available: <http://www.teslamotorsclub.com/showthread.php/23581-Ugh-Another-Model-S-fire-2013-11-06>.
- [5] J. Lingeman, “Tesla Model S burns in Seattle,” *Autoweek*, 2013. [Online]. Available: <http://autoweek.com/article/car-news/tesla-model-s-burns-seattle>.
- [6] E. Musk, “Tesla Adds Titanium Underbody Shield and Aluminum Deflector Plates to Model S,” *Tesla Motors Inc.*, 2014. [Online]. Available: <http://www.teslamotors.com/blog/tesla-adds-titanium-underbody-shield-and-aluminum-deflector-plates-model-s>.
- [7] S. Tobishima, Y. Sakurai, and J. Yamaki, “Safety characteristics of rechargeable lithium metal cells,” *J. Power Sources*, vol. 68, no. 2, pp. 455–458, Oct. 1997.
- [8] E. Darcy, “Screening Li-ion batteries for internal shorts,” *J. Power Sources*, vol. 174, no. 2, pp. 575–578, Dec. 2007.
- [9] N. Takami, H. Inagaki, T. Kishi, Y. Harada, Y. Fujita, and K. Hoshina, “Electrochemical Kinetics and Safety of 2-Volt Class Li-Ion Battery System Using Lithium Titanium Oxide Anode,” *J. Electrochem. Soc.*, vol. 156, no. 2, pp. A128–A132, Feb. 2009.
- [10] P. Ramadass, W. Fang, and Z. (John) Zhang, “Study of internal short in a Li-ion cell I. Test method development using infra-red imaging technique,” *J. Power Sources*, vol. 248, pp. 769–776, Feb. 2014.
- [11] W. Cai, H. Wang, H. Maleki, J. Howard, and E. Lara-Curzio, “Experimental simulation of internal short circuit in Li-ion and Li-ion-polymer cells,” *J. Power Sources*, vol. 196, no. 18, pp. 7779–7783, Sep. 2011.
- [12] F. Ren, T. Cox, and H. Wang, “Thermal runaway risk evaluation of Li-ion cells using a pinch-torsion test,” *J. Power Sources*, vol. 249, pp. 156–162, Mar. 2014.

- [13] E. Sahraei, J. Campbell, and T. Wierzbicki, "Modeling and short circuit detection of 18650 Li-ion cells under mechanical abuse conditions," *J. Power Sources*, vol. 220, pp. 360–372, Dec. 2012.
- [14] E. Sahraei, R. Hill, and T. Wierzbicki, "Calibration and finite element simulation of pouch lithium-ion batteries for mechanical integrity," *J. Power Sources*, vol. 201, pp. 307–321, Mar. 2012.
- [15] E. Sahraei, J. Meier, and T. Wierzbicki, "Characterizing and modeling mechanical properties and onset of short circuit for three types of lithium-ion pouch cells," *J. Power Sources*, vol. 247, pp. 503–516, Feb. 2014.
- [16] T. Wierzbicki and E. Sahraei, "Homogenized mechanical properties for the jellyroll of cylindrical Lithium-ion cells," *J. Power Sources*, vol. 241, pp. 467–476, Nov. 2013.
- [17] L. Greve and C. Fehrenbach, "Mechanical testing and macro-mechanical finite element simulation of the deformation, fracture, and short circuit initiation of cylindrical Lithium ion battery cells," *J. Power Sources*, vol. 214, pp. 377–385, Sep. 2012.
- [18] K. Ozawa, "Lithium-ion rechargeable batteries with LiCoO<sub>2</sub> and carbon electrodes: the LiCoO<sub>2</sub>/C system," *Solid State Ionics*, vol. 69, no. 3–4, pp. 212–221, 1994.
- [19] M.-S. Wu, P.-C. J. Chiang, J.-C. Lin, and Y.-S. Jan, "Correlation between electrochemical characteristics and thermal stability of advanced lithium-ion batteries in abuse tests—short-circuit tests," *Electrochim. Acta*, vol. 49, no. 11, pp. 1803–1812, Apr. 2004.
- [20] S. Tobishima and J. Yamaki, "A consideration of lithium cell safety," *J. Power Sources*, vol. 81–82, no. 0, pp. 882–886, 1999.
- [21] K. Kitoh and H. Nemoto, "100 Wh Large size Li-ion batteries and safety tests," *J. Power Sources*, vol. 81–82, no. 0, pp. 887–890, Sep. 1999.
- [22] J. Nguyen and C. Taylor, "Safety performance for phosphate based large format lithium-ion battery," *Telecommunications Energy Conference, 2004. INTELEC 2004. 26th Annual International*. pp. 146–148, 2004.
- [23] J. Lamb and C. J. Orendorff, "Evaluation of mechanical abuse techniques in lithium ion batteries," *J. Power Sources*, vol. 247, pp. 189–196, Feb. 2014.
- [24] T. D. Hatchard, S. Trussler, and J. R. Dahn, "Building a 'smart nail' for penetration tests on Li-ion cells," *J. Power Sources*, vol. 247, pp. 821–823, 2014.
- [25] T. Yamauchi, K. Mizushima, Y. Satoh, and S. Yamada, "Development of a simulator for both property and safety of a lithium secondary battery," *J. Power Sources*, vol. 136, no. 1, pp. 99–107, Sep. 2004.
- [26] H. Maleki and J. N. Howard, "Internal short circuit in Li-ion cells," *J. Power Sources*, vol. 191, pp. 568–574, 2009.

- [27] S. Santhanagopalan, P. Ramadass, and J. Zhang, "Analysis of internal short-circuit in a lithium ion cell," *J. Power Sources*, vol. 194, pp. 550–557, 2009.
- [28] T. G. Zavalis, M. Behm, and G. Lindbergh, "Investigation of Short-Circuit Scenarios in a Lithium-Ion Battery Cell," *J. Electrochem. Soc.*, vol. 159, no. 6, pp. A848–A859, Jan. 2012.
- [29] W. Fang, P. Ramadass, and Z. (John) Zhang, "Study of internal short in a Li-ion cell-II. Numerical investigation using a 3D electrochemical-thermal model," *J. Power Sources*, vol. 248, pp. 1090–1098, Feb. 2014.
- [30] W. Zhao, "Modeling of Large-Format Li-Ion Cell Performance and Safety," The Pennsylvania State University, 2014.
- [31] P. Dan, E. Mengeritski, Y. Geronov, D. Aurbach, and I. Weisman, "Performances and safety behaviour of rechargeable AA-size Li/LixMnO<sub>2</sub> cell," *J. Power Sources*, vol. 54, no. 1, pp. 143–145, Mar. 1995.
- [32] S. Tobishima, K. Takei, Y. Sakurai, and J. Yamaki, "Lithium ion cell safety," *J. Power Sources*, vol. 90, no. 2, pp. 188–195, 2000.
- [33] D. H. Doughty and A. A. Pesaran, "Vehicle Battery Safety Roadmap Guidance," *Natl. Renew. Energy Lab.*, 2012.
- [34] D. Howell, "U.S. DOE Perspective on Lithium-ion Battery Safety," in *Safety Considerations for EVs powered by Li-ion Batteries*, 2012.
- [35] D. H. Doughty, "SAE J2464 "EV & HEV Rechargeable Energy Storage System (RESS) Safety and Abuse Testing Procedure," *SAE Tech. Pap.*, vol. 2010-01-10, 2010.
- [36] R. A. Matula, "Electrical resistivity of copper, gold, palladium and silver," *J. Phys. Chem.*, vol. 8, p. 1147, 1979.
- [37] W. Zhao, G. Luo, and C.-Y. Wang, "Modeling Nail Penetration Process in Large-Format Li-Ion Cells," *J. Electrochem. Soc.*, vol. 162, no. 1, pp. A207–A217, Jan. 2015.
- [38] D. H. Doughty and C. C. Crafts, "FreedomCAR Electrical Energy Storage System Abuse Test Manual for Electric and Hybrid Electric Vehicle Applications," Sandia National Laboratories, 2006.
- [39] Matweb LLC, "Online Materials Information Resource," <http://www.matweb.com>, 2014. [Online]. Available: <http://www.matweb.com/index.aspx>.

## VITA

### Poowanart Poramapojana

#### Education

---

Ph.D., Mechanical Engineering, Pennsylvania State University	2015
Graduate Certificate, Energy Storage Systems, Pennsylvania State University	2014
M.Sc., Mechanical Engineering, Michigan Technological University,	2012
Graduate Certificate, Hybrid Electric Drive Vehicle Engineering, Michigan Tech	2011
B.Eng., Metallurgical and Materials Engineering, Chulalongkorn University,	2005

#### Research and Professional Experience

---

Graduate Research Assistant	2012 – 2015
Electrochemical Engine Center, Pennsylvania State University	
Teaching Assistant, MEEM4700 Dynamic Systems and Controls	2011 – 2012
Department of Mechanical Engineering, Michigan Technological University	
Graduate Research Assistant	2010 – 2012
Intelligent Mechatronics and Embedded Systems Laboratory, Michigan Tech.	
Assistant Researcher, Research and Development Department	2007 – 2009
Iron and Steel Institute of Thailand (ISIT), Bangkok, Thailand	
Engineer, Engineering and Product Development Division	2006 – 2007
TATA Steel (Thailand) Public Company Limited, Bangkok, Thailand	
Head of Metallurgical Laboratory, Heat Treatment Department	2005 – 2006
KPN Automotive Public Company Limited, Chonburi, Thailand	
Intern, BBL Student Internship Program #43, Bangkok Bank PCL, Thailand	Summer 2005
Supplier Quality Engineer, Supply Chain Department	Summer 2004
Fabrinet Company Limited, Patumthanee, Thailand	

#### Honor and Awards

---

Student Program, ARPA-E Energy Innovation Summit	2014
Best Student Paper Award, IEEE/ASME international conference on	2012
Mechatronic and Embedded Systems and Applications	
Graduate Student Government Travel Award, Michigan Technological University.	2012
Royal Thai Government Scholarship	2010 – 2015